

Vehicle Propulsion Using Continuous Track Linear Induction Motors on Steel Plates

Mark Simpson

A thesis submitted to Auckland University of Technology in partial
fulfilment of the requirements for the degree of Master of Engineering

February 2016

School of Engineering, Computer and Mathematical Sciences

Primary Supervisor: Dr. Adam Taylor

Abstract

Linear induction motors (LIMs) are zero-carbon emission, non-contacting electrical motors that operate on the same principle as rotary squirrel cage induction motors found prominently in industry today. LIMs are capable of operating over wide speed ranges and are effective for generating linear thrust without requiring gears, pulleys or other components for converting angular motion to linear motion.

This thesis explores the concept of a novel robotic vehicle for operation on steel, iron or other surfaces with high magnetic permeability. Two custom designed 4-pole, 3-phase LIM stators, vehicle body, reaction plate tracks, dual variable frequency drive controller board and interface were designed, built and tested. A control strategy utilizing the coupled nature of the attractive normal and linear thrust forces is proposed, focusing on how to achieve peak thrust for given structural and operational parameters, including a phase balancing implementation used to compensate for minor differences in impedances between phases. Simulations and experimental evidence are presented to show the changing ratio of thrust to normal force produced over the slip-frequency operating region of 10-20Hz. With a thrust to normal force ratio selected to suit the operating conditions, the controller outputs a voltage to achieve the requisite flux linkage and Volts-per-Hertz control is used to keep flux linkage constant as the slip-frequency changes during operation.

The developed vehicle has a total mass of 28kg and has been experimentally tested to develop a peak thrust force from standstill of 90N for an input power of 1.7kW. Operation of the vehicle on flat surfaces and climbing inclines up to 21° was validated experimentally.

Table of Contents

Abstract	ii
Table of Contents.....	iii
List of Figures	vi
List of Tables.....	ix
Glossary of Terms.....	x
Attestation of Authorship	xv
Acknowledgements	xvi
Chapter 1 Introduction	1
<i>1.1 Comparison of Adhesion and Thrust Mechanisms.....</i>	<i>1</i>
<i>1.2 Achieving Linear Motion.....</i>	<i>2</i>
1.2.1 Linear Induction Motors	4
<i>1.3 Scope of Thesis</i>	<i>5</i>
Chapter 2 Background Information.....	6
2.1 DC-AC Inverters	6
2.1.1 Inverter Topologies.....	7
2.1.2 Common Issues.....	10
2.2 LIM Operation.....	15
2.2.1 LIM Construction	15
2.2.2 Contrasting RIMs and LIMs.....	17

2.2.3 LIM Equivalent Circuit.....	18
2.3 Climbing Walls.....	22
2.4 Turning.....	27
Chapter 3 LIM Stator Design.....	30
3.1 Design Requirements.....	30
3.2 Stator Structure	31
3.3 Construction of Windings.....	35
3.4 Preliminary Experimental Results	39
Chapter 4 Inverter Design and Development	44
4.1 Overall Design	44
4.2 Direct Digital Synthesis (Sine PWM).....	47
4.3 Software Amplitude and Phase Control.....	52
4.3.1 Current Waveform Distortion.....	53
4.3.2 Imbalanced Phase Compensation	55
Chapter 5 Reaction Plate Design.....	59
5.1 Reaction Plate Structure	59
5.2 Experimental Results.....	64
Chapter 6 LIM Vehicle Performance	71
6.1 Normal Force	71
6.2 Thrust Force.....	77

6.3 <i>Simulated Performance</i>	80
Chapter 7 Future Work	91
7.1 <i>Chassis/Track Design</i>	91
7.2 <i>Control Algorithm</i>	93
7.3 <i>Other Recommendations for Further Development</i>	98
Chapter 8 Conclusion	100
Appendix A Inverter Schematic/PCB	102
A.1 <i>Schematic Diagram</i>	102
A.2 <i>PCB Layout</i>	103
Appendix B Inverter Program Code	104
Appendix C Raw Experimental Data	115
List of References	119

List of Figures

Figure 1.1 Translating Rotational Motion into Linear Motion.....	3
Figure 2.1 Half-Bridge Inverter Topology	7
Figure 2.2 Full-Bridge Inverter Topology.....	8
Figure 2.3 Three-Phase H-Bridge Topology	10
Figure 2.4 IGBT Switching Characteristics (adapted from [12]).....	12
Figure 2.5 IGBT and MOSFET Regions of Dominance [14]	13
Figure 2.6 Typical Rectifier-Inverter Schematic.....	15
Figure 2.7 Cutting a RIM to form a LIM [17].....	16
Figure 2.8 Per Phase Equivalent Circuit of a Single-Sided LIM	18
Figure 2.9 Effect of Changing Slip Frequency with Constant Flux Linkage [20]	24
Figure 2.10 Forces Requiring Balancing in order to Prevent Slippage	26
Figure 2.11 Normalized Friction vs Gravity	27
Figure 2.12 Skid-Steer Turning Torque vs Scrub Torque	28
Figure 3.1 Single Slot/Tooth Pair Constructed with E-I Transformer Laminations	32
Figure 3.2 LIM Tooth and Slot Tessellation Pattern and Dimensions	34
Figure 3.3 Increased Flux Density at Sharp Corners.....	35
Figure 3.4 Total MMF Waveform for Different Coil Throw	37
Figure 3.5 Experimental Setup for Testing Stator and Reaction Plate Parameters	40
Figure 3.6 Per Phase Equivalent Circuit without Reaction Plate	41
Figure 3.7 Phase Current vs Applied Voltage for Different Airgaps	42
Figure 3.8 Attractive Force vs Phase Current for Different Airgaps (w/o reaction plate)	43
Figure 4.1 Controller Block Diagram.....	44

Figure 4.2 Screenshot of the LIM Controller App Interface	45
Figure 4.3 Physical View of Controller Board	47
Figure 4.4 Direct Digital Synthesis using Hardware [32]	48
Figure 4.5 Effect of Number of Samples on Filtered Output Waveform	50
Figure 4.6 3-Phase 50Hz Current Waveform with Inductive Load.....	52
Figure 4.7 Current Waveform Distortion for 100% Amplitude Coefficient	53
Figure 4.8 Bootstrap Capacitor Charging Path.....	54
Figure 4.9 3-Phase Current Waveforms after Balancing in Software	58
Figure 5.1 Early Reaction Plate Prototypes.....	60
Figure 5.2 Thrust vs Reaction Plate Thickness (Simulated)	61
Figure 5.3 Thrust vs Phase Current for Various Reaction Plate Thicknesses	62
Figure 5.4 Thrust vs Reaction Plate Length	63
Figure 5.5 Reaction Plates Form a Closed Loop around the LIM Vehicle	64
Figure 5.6 LIM Locked Thrust vs Phase Current.....	65
Figure 5.7 Thrust vs Frequency for Fixed Phase Current	66
Figure 5.8 Voltage and Current Waveforms Applied to Stators	67
Figure 5.9 Power Factor vs Input Power at Slip=1	68
Figure 6.1 Calculated Forces for 3A Phase Current and Full Slip	72
Figure 6.2 LIM Vehicle and Rig for Achieving a Constant Airgap.....	73
Figure 6.3 Side-on View of Experimental Setup for Measuring Normal Force	74
Figure 6.4 Measured Normal Force Versus Frequency at 3A	74
Figure 6.5 Per Stator Attractive Force vs Current for a 5mm Airgap	76
Figure 6.6 Measuring Vehicle Thrust on Steel Backing Plate with Fixed Track.....	77

Figure 6.7 12.5Hz Thrust vs Phase Current with 5mm Airgap	78
Figure 6.8 Maximally Erect Steel Backing Plate (86°)	79
Figure 6.9 Thrust and Normal Force vs Phase Current	81
Figure 6.10 Force Developed by One Stator versus Reaction Plate Velocity	82
Figure 6.11 Force versus Frequency for a Constant Applied Voltage	83
Figure 6.12 Force vs Frequency for Constant V/Hz Ratio	84
Figure 6.13 Simulated Current vs Frequency using Constant V or V/Hz Techniques...	85
Figure 6.14 Z-Component of Magnetic Field along Stator Length	86
Figure 6.15 2D Snapshot of Magnetic Field Strength in Stator	86
Figure 6.16 Magnitude of Eddy Currents Flowing in the Reaction Plate	87
Figure 6.17 Measuring Joule Heating of Reaction Plate	88
Figure 7.1 Close-up of Chassis Design using Castors.....	92
Figure 7.2 Proposed Future Chassis and Track Design.....	92
Figure 7.3 Microcontroller, Sensors and Expansion Port Interface	94
Figure 7.4 LIM Vehicle Control Sequence	96

List of Tables

Table 1.1 Linear Motion Mechanism Parameter Comparison	4
Table 2.1 Possible H-Bridge Load Conditions	9
Table 3.1 Summary of Desired Vehicle Performance Objectives.....	30
Table 3.2 LIM Stator Physical Parameters.....	39
Table 4.1 Controller LED Functions	46
Table 5.1 Reaction Plate Segment Dimensions.....	64
Table 6.1 Redesigned Vehicle Dimensions.....	73
Table 6.2 Values Used to Calculate Reaction Plate Joule Heating	89

Glossary of Terms

Abbreviations

AC	Alternating Current
ADC	Analog-Digital Converter
DC	Direct Current
EMF	Electromotive Force
FEM	Finite Element Method
IGBT	Insulated-Gate Bipolar Transistor
LC	Inductor-Capacitor
LED	Light Emitting Diode
LIM	Linear Induction Motor
MMF	Magneto-Motive Force
MOSFET	Metal-Oxide-Semiconductor Field Effect Transistor
PID	Proportional-Integral-Derivative (Controller)
PWM	Pulse Width Modulation
RC	Resistor-Capacitor
RIM	Rotary Induction Motor
RMS	Root Mean Square
SVPWM	Space Vector Pulse Width Modulation

Nomenclature

a	Width of stator from center (half total width)
a_e	Effective stator width accounting for transverse edge effects [$2a_e = 2a + 0.6g$]
A	Amplitude coefficient for controller output waveform
$\cos\phi_1$	Power factor
d	Reaction plate (secondary) thickness
d_i	'i'th data entry of lookup table
$d_{t\%}$	Percentage of dead time per cycle
f_c	Carrier frequency
f_{out}	Fundamental output frequency from controller (primary frequency)
f_s	Supply frequency
F_f	Friction force between vehicle wheels and reaction plate
F_n	Net normal force on stator
F_{na}	Attractive force normal to stator
F_{nr}	Repulsive force normal to stator
F_{nw}	Component of the vehicle weight normal to stator
$F_{segment}$	Thrust produced by single reaction plate segment
F_x	Linear thrust
$F(x,t)$	Time and spatially varying MMF waveform in airgap
g	Airgap length
g_e	Equivalent airgap length accounting for longitudinal end effects (see [17])
G_e	Goodness Factor
h_s	Slot height

h_t	Tooth height
i_x	Time varying current waveform in phase x
I_1	Primary current
I'_2	Secondary current
J_m	Primary current sheet fundamental
K_w	Winding factor
l_{ec}	Coil end connection length
l_{hinge}	Length of hinge section connecting reaction plate segments
$l_{segment}$	Reaction plate segment length
l_{stator}	Stator length
L	Phase inductance
mg	Weight of complete vehicle (mass x acceleration due to gravity)
n	Length of the sine lookup table (number of samples per cycle)
N	Number of turns per phase
p_1	Number of poles
P_m	Mechanical power
q	Slots per pole per phase
r_c	Winding conductor radius
r_{di}	Registry address for 'i' data entry
R_1	Primary resistance
R'_2	Secondary resistance
S	Slip
v_r	Reaction plate velocity

v_s	Synchronous velocity
v_x	Time vary voltage waveform applied to phase x
V_{DCBUS}	Voltage on DC bus of controller
$V_{f,rect}$	Forward voltage drops of diodes of controller rectifier
V_1	Primary voltage
w_s	Slot width
w_t	Tooth width
y	Coil throw
Z_L	Inductive impedance
α_x	Desired phase shift for phase x
α^*_x	Compensated phase shift for phase x
β'	Coil span $[\frac{y}{\tau}]$
η_1	Stator efficiency
θ	Phase angle
θ_b	Angle of backing plate relative to horizontal plane
λ_d	Differential geometrical permeance $[\frac{5\frac{g}{b_s}}{5+4\frac{g}{b_s}}]$
λ_f	End connection geometrical permeance $[0.3q(3\beta - 1)]$
λ_s	Slot geometrical permeance $[\frac{1}{12}\frac{h_s}{b_s}(1 + 3\beta')]$
μ	Relative magnetic permeability
μ_s	Coefficient of static friction
μ_0	Magnetic permeability of free space
ρ_{Cu}	Resistivity of copper

σ	Conductivity (of aluminum)
σ_e	Equivalent conductivity including end effects and airgap (see [17])
τ	Pole pitch
χ_m	Magnetizing reactance
χ_C	Capacitive reactance
χ_L	Inductive reactance
$\chi_{l\sigma}$	Primary reactance
ω_1	Supply angular frequency

Attestation of Authorship

I hereby declare that this submission is my own work and that, to the best of my knowledge and belief, it contains no material previously published or written by another person (except where explicitly defined in the acknowledgements), nor material which to a substantial extent has been submitted for the award of any other degree or diploma of a university or other institution of higher learning.



Mark Simpson

Acknowledgements

I would like to take the opportunity to recognize the people who have helped me along the way in my research.

Thank you to all of the faculty and staff at Auckland University of Technology for allowing me the freedom and flexibility to pursue my research with few limitations or bureaucratic barriers. In particular, I would like to thank my research supervisor, Dr. Adam Taylor, for the insight provided into LIM theory and helping me with the various experimental hurdles encountered.

Finally, thank you to my wife, Emily, for her love, support and understanding of the time commitment I have made to complete this research.

Chapter 1 Introduction

The need for robotic exploration of unknown environments, cleaning of the exterior of high-rise buildings and inspection or maintenance at large scale industrial sites has resulted in growing interest in robotic vehicles capable of adhering to non-horizontal surfaces. Robots can be used to assist workers with time-consuming or dangerous tasks in order to improve operational efficiency and safety. In such robots, the mechanism for developing adhesion and the mechanism for generating thrust are usually distinct and separate from the robot itself, leading to increased robot weight, development and construction expenses. A robotic vehicle with inherent adhesion and thrust abilities is therefore desirable and advantageous.

1.1 Comparison of Adhesion and Thrust Mechanisms

Various adhesion technologies are available today for utilization in wall-climbing vehicles. These technologies encompass magnetic, pneumatic, mechanical, electrostatic and chemical, and each have their own set of advantages and disadvantages in terms of load capacity, reliability, expense, weight and required components for infrastructure when applied to wall climbing robots [1].

In some cases, permanent magnets may be employed to produce an attractive force between the robot and climbing surface that is capable of withstanding large loads, but operation is limited to applications with ferromagnetic surfaces [2]. Pneumatic suction systems operate by placing suction cups onto surfaces and use a negative fluid pressure of air to create a partial vacuum. These systems have a large load capacity, but require a relatively clean and flat non-porous surface to ensure reliable operation [3].

Climbing robots may alternatively use mechanical limbs to grip to a surface for climbing [4]. Such robots require complicated control strategies due to the numerous motors and gears needed to move limbs freely and are limited to operation on surfaces with protrusions to grasp onto. Other adhesion techniques include the use of electro-adhesive pads which produce an attractive force due to an electric field or the use of novel materials that chemically bond to the surface [5].

The mechanisms used to produce thrust for wall-climbing robots also vary depending on the targeted operating surface. Some robots use arrangements of legs to propel themselves in a fashion that mimics the way animals move about. Robots also often use wheels or tracks to convert rotational motion from a motor and gearbox into linear motion. Other types of robots may use slides or guide wires for translation across predetermined pathways [1].

All of the robot types discussed above produce thrust or an adhesive force by coming into physical contact with the operating surface and all movement is a result of a friction force between the robots and operating surfaces at the point of contact. Non-contacting interfaces also exist for scenarios in which the robot is levitating above the operating surface and rely on non-physical forms of propulsion, such as propulsion resulting from interactions with electric or magnetic fields [6].

1.2 Achieving Linear Motion

Linear thrust may be readily achieved through the conversion of rotational motion using gears, pulleys, belts or other devices. Directly coupling a rotating motor to a wheel

or gearbox is one such technique for achieving linear motion, but other popular techniques include the use of belt conveyors, ball/lead screw systems or rack and pinion gears [7].

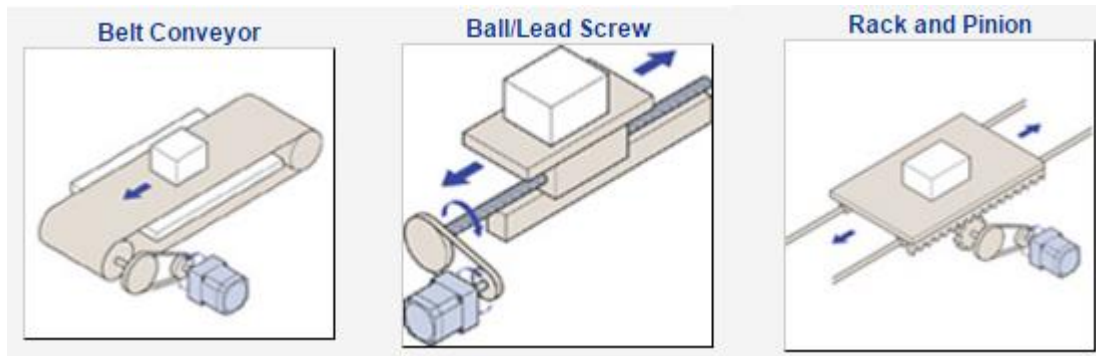


Figure 1.1 Translating Rotational Motion into Linear Motion [7]

Belt conveyors convert the rotational motion of the drive motor to linear motion of the belt via pulleys. The payload is placed on the belt and can hence be moved from one place to another in a linear fashion. The friction produced between the belt and internal support medium due to the weight of the payload limits achievable thrust and may result in slipping between the belt and end rollers. The travel range is also restricted by the length of the belt.

Ball/lead screw systems use a motor to turn a long rod with special threads and have a platform which moves along the rod as it turns. Ball screw systems have a platform with a recirculating tube that contains ball bearings that roll along the helical raceway of the rod to produce linear motion with very little friction. Lead screw systems have a female threaded platform that moves along the length of the threaded rod like a nut. These systems can achieve large thrust over a short travel range and have relatively low achievable linear velocities.

The rack gear of a rack and pinion gear set is similar to a regular gear that has been cut through to the center and rolled out flat. When this gear is attached to a platform

for movement and matched to a pinion gear connected to a motor, the teeth of the rotating pinion gear mate with those of the rack, pushing the rack and platform in a linear direction. Rack and pinion gears are affordable and have a travel range limited by the arbitrary length of the rack gear.

1.2.1 Linear Induction Motors

Linear Induction Motors (LIMs), however, are capable of generating linear motion directly, through a non-contact mechanism that does not require any moving parts other than the motion target object. For a LIM, the motion target object is a non-magnetic, conductive plate that moves via interaction between magnetic fields produced by induced eddy currents in the plate and the rotating magnetic field established in the stator.

A summary of the key advantages and disadvantages of the linear motion mechanisms discussed herein is found in Table 1.1.

	Belt Conveyor	Ball/Lead Screw	Rack and Pinion	LIM
Thrust	Fair	Good	Good	Excellent
Friction	Good	Fair	Good	Excellent
Speed Range	Good	Fair	Fair	Excellent
Travel Range	Fair	Limited	Good	Excellent
Maintenance	Good	Good	Good	Excellent
Price	Good	Good	Excellent	Fair

Table 1.1 Linear Motion Mechanism Parameter Comparison

Table 1.1 shows the LIMs outperform belt conveyor, ball/lead screw and rack and pinon systems in terms of thrust, friction, speed, travel and maintenance, but the limiting factor of LIMs is their price. LIMs also tend to be physically large, heavy and require a

variable frequency drive for speed control and efficient operation. The price may be offset for a wall climbing robot due to the reduced cost of mechanisms responsible for adhesion and thrust. LIMs can be used to achieve an attractive force sufficient for climbing when operated on ferromagnetic surfaces, while simultaneously producing thrust via interaction with a non-ferromagnetic, highly conductive secondary reaction plate, eliminating the need for two separate force producing mechanisms. A caterpillar track made from aluminum can be used as this secondary reaction plate, but also required wheels and bearings to be employed to maintain a constant airgap between the stator and reaction plate track during movement.

1.3 Scope of Thesis

This research aims to verify the capability of LIMs to be used as adhesion/propulsion mechanism for a robotic wall climbing vehicle for operation on steel plates. Chapter 2 provides a background to the technical concepts explored in the research and introduces the key components. Chapters 3 covers the design and assembly of the stators. Chapter 4 discusses the design, implementation and performance of the inverter. Chapter 5 analyzes reaction plate track prototypes and experimentally validates their performance. Chapter 6 ties the critical elements of the vehicle together to present experimental results and comments on the overall applicability as a wall climbing vehicle. Recommendations for future work are presented in Chapter 7, followed by presentation of thesis conclusions in Chapter 8.

Chapter 2 Background Information

The following sections familiarize the reader with the technical concepts introduced in this thesis. Section 2.1 introduces basic inverter operation and topologies. Section 2.2 summarizes LIM operation and areas of research. Section 2.3 offers a summary of the operating principle and forces required for wall-climbing vehicles to climb inclines. The chapter is concluded in Section 2.4 with a description of the how steering a tracked LIM vehicle can be achieved.

2.1 DC-AC Inverters

An inverter is used to convert a DC power supply into an AC output, which can then be stepped-up to mains voltage using a transformer for the purpose of powering appliances that require AC input from batteries in household applications. For industrial applications, inverters are used to generate AC waveforms of controllable frequency for the purpose of controlling the rotational speed of induction motors and synchronous machines. The source of the DC power supply for industrial purposes can be from a rectified single-phase or 3-phase AC input, but may also be from common DC storage devices such as batteries.

Several different techniques of converting DC into AC exist today, ranging from analogue circuits that generate very low harmonic distortion, such as the Bubba Oscillator [8], through to complicated digital switching techniques that use electronic switches in a bridge topology to reverse current directions [9], simulating AC. Analogue sine wave generators, however, rely on the accuracy of temperature-sensitive resistors and capacitors to generate a fixed frequency; requiring a wide range of values, across multiple

orders of magnitude, in order to generate a reasonable number of frequencies. More recently, digital switching techniques have circumvented these problems by using microcontrollers to accurately time the switching of the electronic switches to generate waveforms of arbitrary frequency and of controllable amplitude, but may instead suffer from greater harmonic distortion. The harmonic distortion can be minimized through the use of low pass filters at the inverter output.

2.1.1 Inverter Topologies

Variable frequency inverters use a number of electronic switches in a variety of possible topologies to convert voltage from a DC input voltage bus into an AC waveform. The simplest such inverter is a half-bridge topology as shown in Figure 2.1.

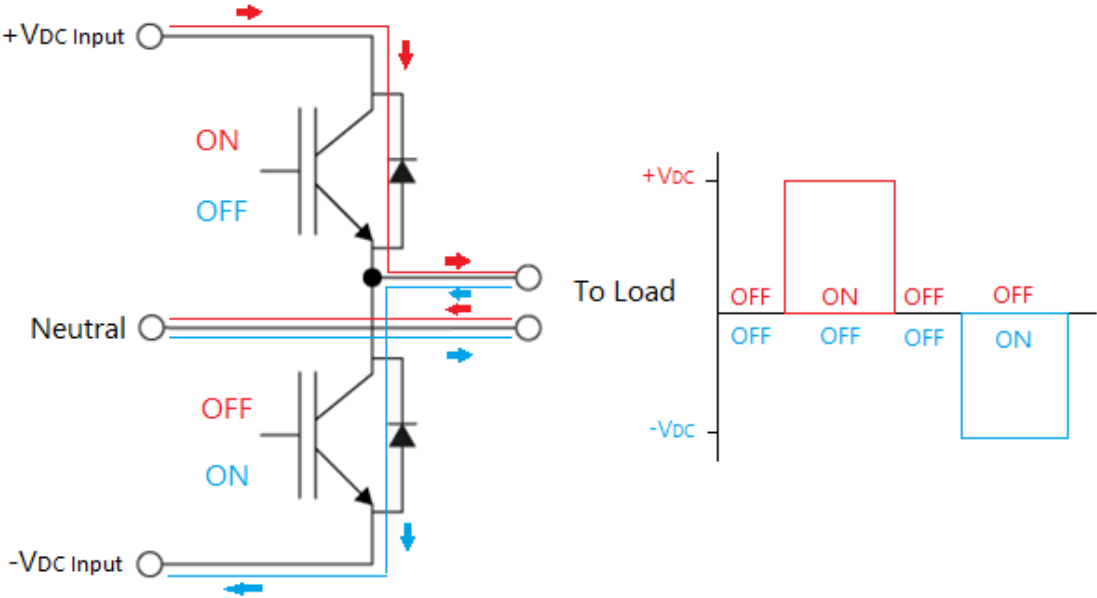


Figure 2.1 Half-Bridge Inverter Topology

The half-bridge inverter consists of a high-side switch and a low-side switch which together form one circuit “leg”. The particular inverter topology of Figure 2.1

requires a positive DC input rail and a negative DC input rail. One lead of the single-phase AC load is connect to the neutral point of the DC supply with the other connected to the central point of the switches. When the high side switch is turned on, current flows from the positive DC voltage rail, through the load, to neutral. The high side switch is then turned off at a time equal to one half of the output waveform period later and the low side switch turned on. The current then flows from the neutral, which is at a higher electric potential than the negative rail, through the load in the reverse direction and to the negative DC voltage rail. The alternating direction of current flow through the load is how the inverter synthesizes an AC waveform. It should be noted that the two switches ought not to be switched on at the same time or short-circuiting will occur between the positive and negative voltage rails.

The half-bridge topology can be extended through the addition of another pair of switches to create a topology known as a single-phase full-bridge inverter, as shown in Figure 2.2.

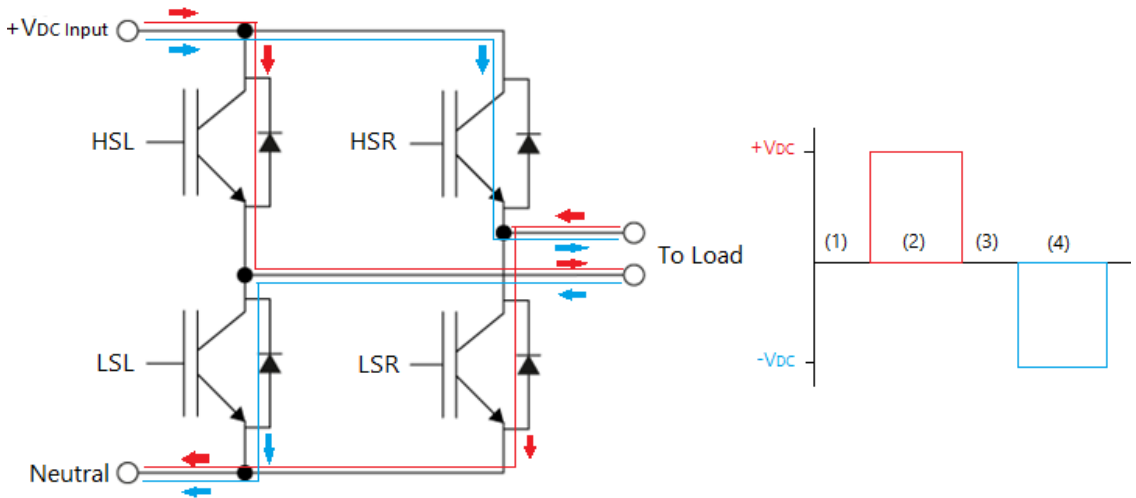


Figure 2.2 Full-Bridge Inverter Topology

The full-bridge inverter consists of 4 switching elements which can be turned off and on individually using control signals. The primary advantage of the full-bridge topology over the half-bridge topology is that alternating current can be achieved using only a positive DC voltage rail.

The four switching elements of the full-bridge can be denoted as high-side left (HSL), high-side right (HSR), low-side left (LSL) and low-side right (LSR). A positive voltage across the load can then be applied by turning HSL and LSR switches on simultaneously, leaving the others off. Similarly, a negative voltage can be applied by turning the HSR and LSL switches on while the others are off. Table 2.1 summarizes the four types of possible scenarios for the topology and gives an example of the switch states that could cause them.

Voltage Across Load	HSL	HSR	LSL	LSR
Zero Potential (1)/(3)	ON	ON	OFF	OFF
Positive (2)	ON	OFF	OFF	ON
Negative (4)	OFF	ON	ON	OFF
Short-Circuited	ON	OFF	ON	OFF

Table 2.1 Possible H-Bridge Load Conditions

The full-bridge topology can be further extended to support 3-phase loads with the addition of another two switching elements, as shown in Figure 2.3. In such a topology, 1 high-side and 2 low-side switches can be on while others are off, forming conduction pathways that allow current to flow through the load. The current enters from the lead connected to the high-side switch in the on state and exits through the leads connected to the low-side switches in the on state. Alternatively, 2 high-side and 1 low-side switches can be on with others off. In this case, two leads source current while the third sinks

current. It should be again noted that no two switches within the same leg may normally be on at the same time or short-circuiting will occur.

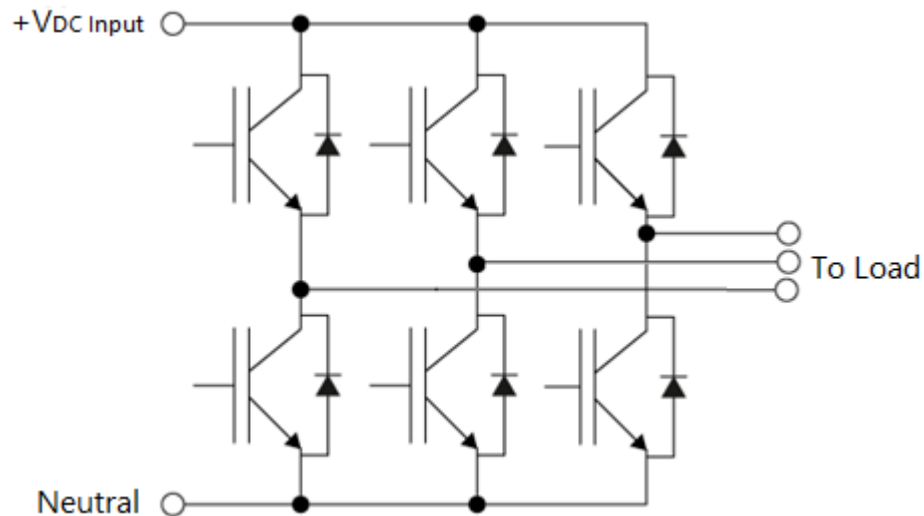


Figure 2.3 Three-Phase H-Bridge Topology

Several other topologies exist that extend upon this, including those using multiple switching elements in place of each of the single switching elements of Figure 2.3. Such topologies utilize space vector PWM (SVPWM) to create 3, 5 or 7 level inverters with increasing fidelity and very low total harmonic distortion in the voltage and current waveforms [9].

2.1.2 Common Issues

This subsection describes three issues that need to be handled when designing a polyphaser inverter. The issues discussed are those relating to dead-time insertion to prevent short-circuiting, selection of switching elements and regenerative braking problems for inductive loads.

2.1.2.1 Dead-Time Insertion

Particular care must be taken when switching the switches to ensure the short-circuited condition of Table 2.1, when both the high-side and low-side switches in a single leg are on, is not caused at any point in time unless the topology has been specified to allow ‘shoot-through’ or short-circuiting states [10]. If short-circuiting occurs, a low impedance pathway can link the DC voltage bus to ground and cause a significant current to flow, likely damaging the components of the inverter. Shoot-through is a highly undesirable condition for the voltage-source-inverter topologies described in this chapter, however, some topologies exist that use this condition to their advantage, such as for shoot-through burst control of Z-source inverters [11]. To prevent shoot-through from accidentally occurring, a ‘dead-time’ period is allowed to elapse between the switching off of one switch and switching on of the other, for two switches in the same leg of the circuit.

Dead-time can be defined as the difference between the switch-on delay time $t_{d,sw-on}$ of the non-conducting switching element and the switch-off time $t_{off}(i_s)$ of the conduction one [12], given by Equation 2.1.

$$t_d(i_s) = t_{d,sw-on} - t_{off}(i_s) \quad (2.1)$$

Taking into account the current rise and fall times, t_r and t_f , and the base drive turn-on and turn-off delays, $t_{d,on}$ and $t_{d,off}$, Equation 2.1 becomes,

$$t_d(i_s) = t_{d,sw-on} + t_{d,on} - t_{d,off}(i_s) - t_f(i_s) \quad (2.2)$$

Figure 2.4 illustrates the current switching process from the moment a high-side IGBT in the on-state is sent a control signal dictating the switch should turn off, through to the complete turning on of a low-side switch initially in the off state.

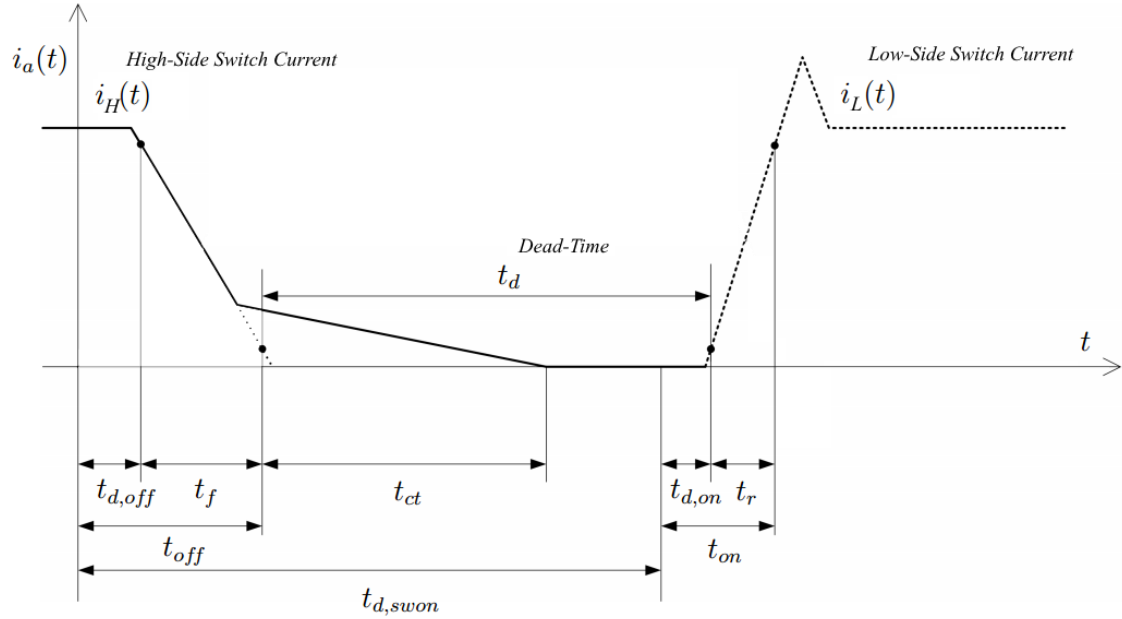


Figure 2.4 IGBT Switching Characteristics (adapted from [12])

Figure 2.4 visually illustrates that the dead-time is the time allowed to elapse from when the current through the high-side switching element has been almost completely halted, until the current begins to flow through the low-side switching element. Dead-time should be selected conservatively such that it exceeds the current tail time, t_{ct} . The current tail time is the time taken for current due to recombination of minor carriers within MOSFETs or IGBTs to settle to zero and is responsible for additional switching losses, especially when the voltage across the switching element approaches its rated voltage [13]. The current tail time for each model of switching element may differ so should be considered when selecting the switching elements to be used.

2.1.2.2 Switching Element Selection

In addition to the required dead-time, Figure 2.4 also shows the various delays that take place every time a switching element is switched. The delays include the finite

delay time between the control signal command to switch off and the time at which the current begins to fall, $t_{d,off}$. The fall time, t_f , is also non-instantaneous and the current rise time, t_r , also takes a finite amount of time to rise and may have some overshoot. Typical, minimum and maximum values for each of the switching element delays can normally be found in the product datasheet.

The switching elements used for inverters are usually either MOSFETs or IGBTs. IGBTs dominate in terms of breakdown voltages yet MOSFETs reign in terms of switching frequency due to the decreased current tail time [13]. Consequently, either MOSFETs or IGBTs can be used depending on the target inverter performance objectives. Figure 2.5 provides a reference for the switching element selection process based on the intended region of application.

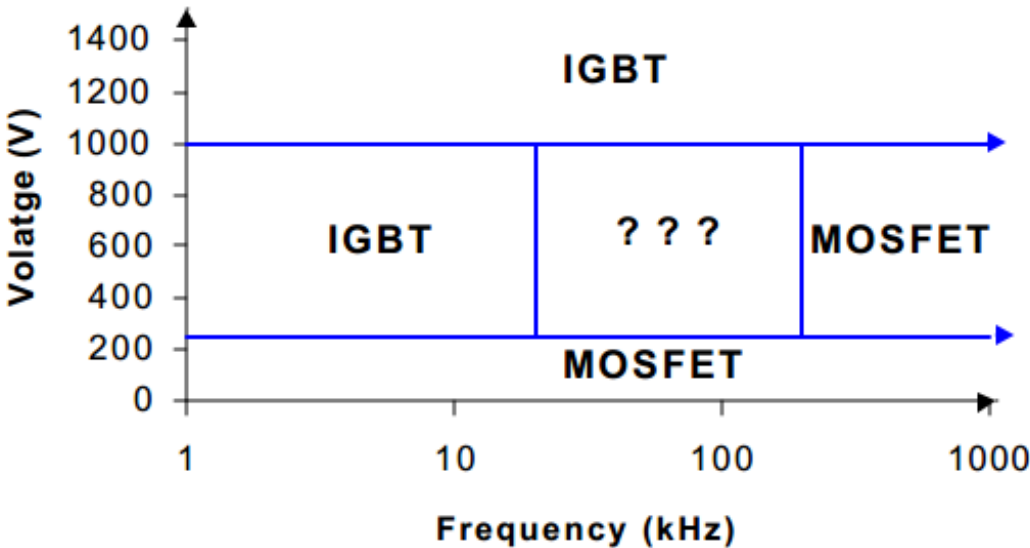


Figure 2.5 IGBT and MOSFET Regions of Dominance [14]

Figure 2.5 shows that IGBTs are preferred for low frequency or high voltage applications, while MOSFETs are preferred for low voltage or high frequency

applications. The mid-voltage- mid-frequency range marked with question marks indicates that MOSFETs and IGBTs should be contrasted and judges on their individual merits to suit each application. While Figure 2.5 is useful when selecting from readily available and affordable MOSFET and IGBT components, high-voltage power MOSFETs made from silicon carbide rated to 5,000V are also available if the designer wants the characteristics of a MOSFET for a high voltage inverter [15].

The minimum required dead-time, t_d (i_s), for a typical IGBT is approximately $0.5\mu s$ [13]. The fraction of dead-time per cycle, $d_{t\%}$, is given by,

$$d_{t\%} = 2f_c t_d * 100\% \quad (2.3)$$

Switching an IGBT using PWM with a carrier frequency of 10kHz can thus be calculated to have a dead-time equal to 1% of the total period. The dead-time causes errors in the output voltage and distortion of the output waveform for sine-PWM [16]. In addition, voltage drops of the power transistors and freewheeling diodes also reduce the magnitude of the produced waveform.

2.1.2.3 Regenerative Braking

The inverter topologies discussed in subsection 2.1.1 all used a high voltage DC rail as the power supply. However, in practical applications it is commonplace to have an industrial three-phase supply as the input, which is then rectified through a 3-phase bridge rectifier and ripple smoothed out with a DC link capacitor. With the addition of the DC link capacitor, excessive charge may accumulate in the capacitor when an inductive load is ‘braking’ or ‘generating’ or if the magnetic field suddenly collapses. Braking or generating states occur, for example, when an induction motor is rotating at a speed

greater than its synchronous speed. This excessive charge threatens the service lifetime of the capacitor, gate drivers and switching elements, so a ‘chopper’ and dump resistor (R) is added to dissipate the excess energy. Figure 2.6 shows the overall schematic for a typical rectifier-inverter.

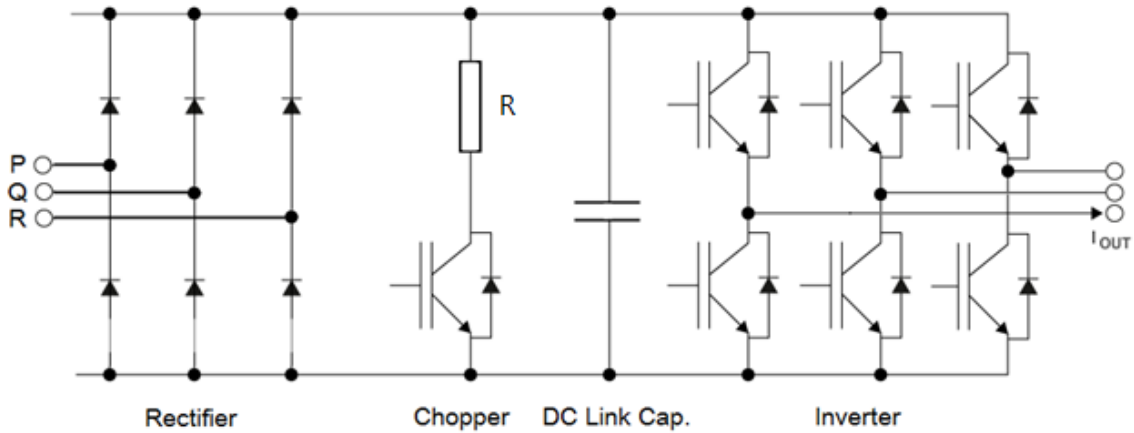


Figure 2.6 Typical Rectifier-Inverter Schematic

2.2 LIM Operation

2.2.1 LIM Construction

A LIM consists of a slotted stator (or primary) and reaction plate (or secondary). The stator is a stack of steel laminations and has slots that are filled with polyphase windings in such a manner that a rectilinear sinusoidally distributed magnetic field is produced along the length of the stator [17]. A LIM can be thought of as a rotary induction motor (RIM) that has been cut along the core at some point, been rolled flat and had any windings severed by the cut removed.

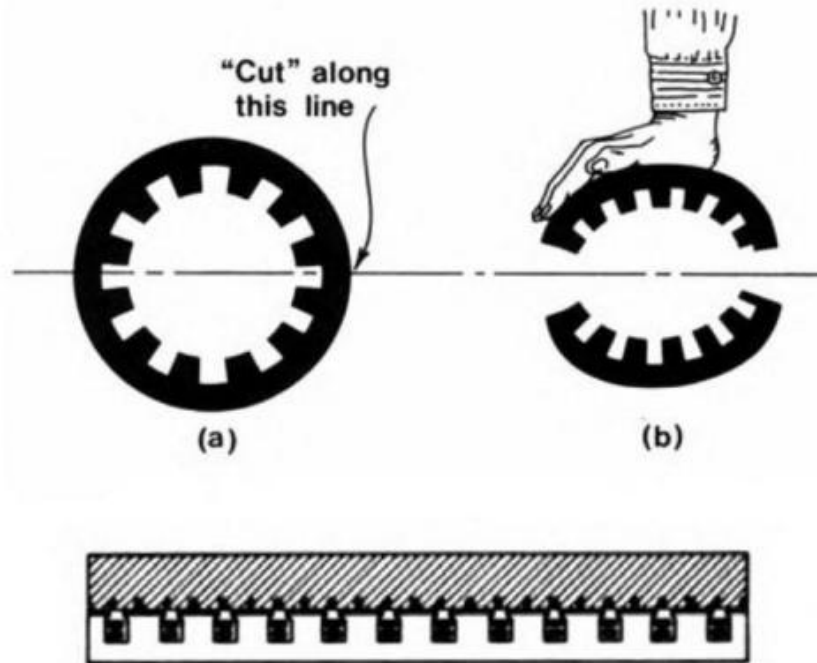


Figure 2.7 Cutting a RIM to form a LIM [17]

The reaction plate of a LIM usually takes the form of a conductive sheet, commonly aluminium or copper, and may also have an iron or steel backing plate [18].

The operating principle is also analogous to that of a RIM whereby relative motion between the travelling magnetic field and the conductive sheet of the reaction plate induces currents in the reaction plate in accordance with the Lorentz force law. The magnetic field of the induced currents interact with the travelling magnetic field, producing a thrust force which seeks to minimize the difference in linear velocity between the two [19]. Additionally, if the reaction plate has an iron or steel backing plate, an attractive normal force will also be produced between the backing plate and stator due to ferromagnetic attraction [20].

The travelling field pattern has a linear velocity, also known as synchronous speed, given by,

$$v_s = 2\tau f_s \quad (2.4)$$

where τ is the pole pitch and f_s is the supply frequency. As electric currents are only induced when there is a mismatch between the secondary and the travelling magnetic field, when the secondary is travelling at the synchronous speed the developed thrust is zero. This implies that the secondary will never be able to fully accelerate to the synchronous speed and will always slip by some amount S . The slip can be calculated by,

$$S = 1 - \frac{v_r}{v_s} \quad (2.5)$$

where v_r is the velocity of the reaction plate (secondary).

2.2.2 Contrasting RIMs and LIMs

A fundamental difference between a RIM and a LIM is that for a RIM, the stator closes onto itself allowing the magnetomotive force (MMF) waveform produced to continuously propagate around the loop while power is applied. Instead, the stator of a LIM may have only a few pole pitches and is quite short so has definite leading and trailing edges to the stator. These edges adversely affect LIM performance due to distortion of the magnetic fields in vicinity of the edge [21] and is known as the ‘longitudinal end effect’.

Other notable differences between a RIM and a LIM include the comparatively larger airgap required for LIMs to ensure there is no mechanical interaction or physical contact between the primary and secondary. The increased airgap leads to an increase in relative reluctance of the airgap and elevated leakage flux [22]. Furthermore, flux leakage flux in a LIM is more noticeable when the pole pitch is small with respect to the airgap, as the ratio of relative reluctance in the longitudinal and transverse decreases,

encouraging further leakage flux. This ratio can be increased through the use of a backing plate, providing a low reluctance path within which flux can flow [17].

2.2.3 LIM Equivalent Circuit

Equivalent circuits for single-sided LIMs [23] [24] [25] are similar to those of transformer and RIMs, but have various adaptations to cater for the effects unique to LIMs such as the transverse and longitudinal end effects. The LIMs proposed for the vehicle constructed within this research are single-sided, short primary, long conductive sheet types intended to be operated at low speeds, allowing general analysis to be conducted using the relatively simple per phase equivalent circuit of Figure 2.8 [17].

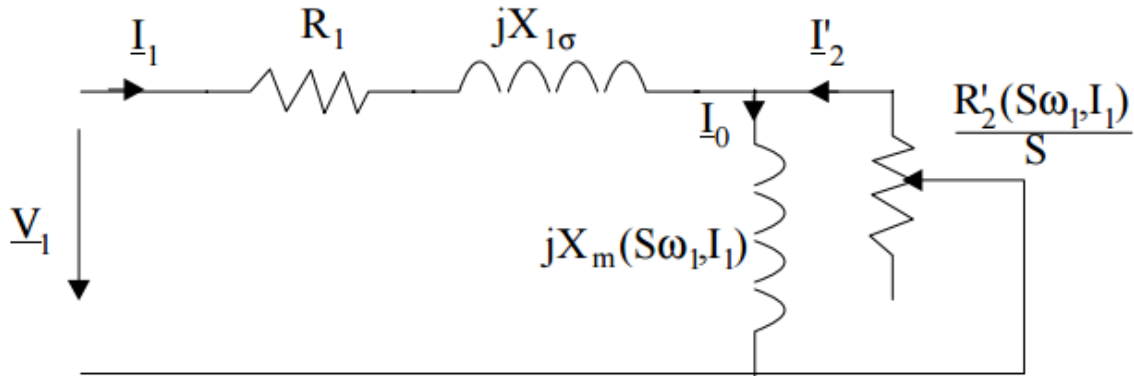


Figure 2.8 Per Phase Equivalent Circuit of a Single-Sided LIM

The parameters of Figure 2.8 are the primary phase drive voltage V_1 , primary current I_1 , primary resistance R_1 , primary reactance $X_{1\sigma}$, secondary current I'_2 , secondary resistance R'_2 and magnetizing reactance X_m . R'_2 and X_m are variable quantities dependent on slip-frequency $S\omega_1$ and primary current I_1 . X_m and R'_2 are proportional to the slip-frequency and current is the result of encapsulating the unique effects of LIMs, such as

airgap leakage, aluminium reaction plate skin effects and transverse edge effects into an equivalent airgap g_e and equivalent aluminium sheet conductivity σ_e .

Equations for the parameters in the per-phase equivalent circuit in Figure 2.8 can be derived from those for the analogous RIM equivalent circuit, resulting in Equations 2.6 – 2.9 [17]. The resistance of each phase, R_l , of stator windings is given by,

$$R_l = \frac{N\rho_{Cu}(4a+2l_{ec})}{\pi r_c^2} \quad (2.6)$$

where N is the number of turns per phase, ρ_{Cu} is the resistivity of copper, a is half the stator width, l_{ec} is the length of winding end connections per turn and r_c is the radius of the conductor windings. The reactance of the stator due to the each phase, $X_{l\sigma}$, is given by,

$$X_{l\sigma} = \frac{2\mu_0\omega_1}{p_1q} [(\lambda_s + \lambda_d)2a + \lambda_f l_{ec}] N^2 \quad (2.7)$$

where μ_0 is the magnetic permeability of free space, ω_1 is the fundamental angular frequency of the voltage waveform, p_1 is the number of poles, q is the number of slots per pole per phase and λ_d , λ_f and λ_s are the differential, end and slot geometrical permeances or coefficients due to the particular physical layout of the windings and stator slots [17]. The magnetizing reactance, X_m , can be calculating using,

$$X_m = \frac{\mu_0\omega_1(NK_w)^2\tau(2a_e)}{\pi^2 p_1 g_e (S\omega_1 I_1)} \quad (2.8)$$

where K_w is the winding factor of the stator coils, τ is the pole pitch, a_e is the effective stator width accounting for transverse edge effects and σ_e is effective conductivity of the reaction plate - a slip-frequency and phase current magnitude dependent quantity accounting for end effects and airgap length [17]. The resistance of

the reaction plate, R'_2 , is the quotient of the magnetizing reactance and the Goodness Factor, G_e , calculable by,

$$R'_2 = \frac{X_m}{G_e} = \frac{12(NK_w)^2 a_e}{p_1 \tau d \sigma_e (S \omega_1, I_1)} \quad (2.9)$$

where d is the thickness of the reaction plate and the Goodness Factor is defined by,

$$G_e = \frac{\mu_0 \omega_1 \tau^2 \sigma_e d}{\pi^2 g_e (S \omega_1, I_1)} \quad (2.10)$$

Excluding copper resistivity, the quantities present in Equations 2.6 to 2.10 are all selectable design parameters based on the physical geometry of the system.

The stator winding resistance, stator reactance and magnetizing reactance terms in the equivalent circuit of Figure 2.8 represent the copper losses due to the stator windings, induced self-EMF due to leakage flux and the magnetizing current required to overcome the non-zero reluctance of the stator, respectively. As R'_2/S represents the load, the remaining power, P_m , available to produce mechanical work is equal to the square of the induced currents in the reaction plates multiplied by R'_2/S . The per-phase power can be summed across the number of phases to which power is applied, resulting in an equation for power available to the system given by,

$$P_m = \frac{3I_2'^2 R'_2}{S} \quad (2.11)$$

However, the mechanical power in a linear system can also be expressed by,

$$P_m = \frac{dW}{dt} = F_x \frac{dx}{dt} = F_x v_s \quad (2.12)$$

Equation 2.12 can hence be rearranged for F_x , the linear thrust force developed, and combined with Equations 2.4 and 2.11 to get,

$$F_x = \frac{P_m}{v_s} = \frac{3I_2'^2 R_2'}{s \cdot 2\tau f_s} \quad (2.13)$$

Kirchoff's laws can then be applied to Equation 2.13 to yield a formula for thrust in terms of the input current through the stator by solving for I_2' , giving,

$$I_2'^2 = \frac{I_1^2}{\left(\frac{R_2'}{sX_m}\right)^2 + 1} = \frac{I_1^2}{\left(\frac{1}{sG_e}\right)^2 + 1} \quad (2.14)$$

Equations 2.13 and 2.14 can then be combined to give,

$$F_x = \frac{3I_1^2 R_2'}{s \cdot 2\tau f_s \left[\left(\frac{1}{sG_e}\right)^2 + 1\right]} \quad (2.15)$$

The efficiency η_l is a quotient of the power made available for doing mechanical work and the power supplied to the system, equal to the power used for work minus power lost due to resistive heating of the primary windings. Using Figure 2.8 and ignoring core and other losses, the efficiency can be approximated by,

$$\eta_1 = \frac{2\tau f_s (1-s) F_x}{2\tau f_s F_x + 3I_1^2 R_1} \quad (2.16)$$

The power factor is calculable via Equation 2.17.

$$\cos \varphi_1 = \frac{2\tau f_s F_x + 3I_1^2 R_1}{3V_1 f_1 I_1} \quad (2.17)$$

In addition to linear thrust, the normal force developed is of interest for the intended application as a ferromagnetic metal plate climbing vehicle. The normal force developed consists of two components – one repulsive, one attractive. If the vehicle is capable of generating a normal attractive force greater than the weight of the vehicle then upside down operation along surfaces in which the entire mass of the vehicle is self-supported also becomes possible. The caveat of an attractive force too great, however, is

the increased frictional losses due to effective weight of the vehicle on the bearings. The net normal force is given by Equation 2.18 [17],

$$F_n = F_{na} + F_{nr} = 2a_e p_1 \tau \frac{\mu_0 J_m^2 \tau^2}{\pi^2 g_e^2 (1+S^2 G_e^2)} \left[1 - \left(\frac{g_e \pi}{\tau} \right)^2 S^2 G_e^2 \right] \quad (2.18)$$

where J_m is the primary current sheet fundamental given by,

$$J_m = \frac{3\sqrt{2}NK_w I_1}{p_1 \tau} \quad (2.19)$$

Equation 2.18 implies that the net normal force is attractive when Equation 2.20 is satisfied.

$$SG_e < \frac{\tau}{g_e \pi} \quad (2.20)$$

This can also be expressed by substituting the definition of the Goodness Factor to yield;

$$\frac{S\mu_0 \omega_1 \tau \sigma_e d}{\pi} < 1 \quad (2.21)$$

The quantities of Equation 2.21 can be separated into those that characterize the motor structure (pole-pitch, reaction plate conductivity and reaction plate thickness) and control parameters (slip and angular frequency), subject to a scaling factor of μ_0/π . This implies that the implementation of an appropriate control strategy and choice of structural parameters can ensure that the robotic vehicle always operates such that the net normal force is attractive.

2.3 Climbing Walls

The mechanisms for producing an attractive force to enable a robotic vehicle to adhere to walls and those for generating thrust in order to move about were discussed in

Chapter 1. Regardless of how the attractive force is produced, the attractive force producing component tends to always be separate from the thrust component as the direction of the attractive force vector is perpendicular to any intended movement directions.

LIMs, however, produce linear thrust while simultaneously producing a normal force component. For low-speed LIMs with an iron backing plate, this normal force is always attractive, even for standstill conditions (slip = 1) [17]. The research outlined within this thesis proposed utilizing the attractive force produced by LIMs to create a type of wall climbing vehicle for climbing on steel plates. Such a vehicle could find application in many industrial areas, including those of cleaning, inspecting or painting enormous facilities and equipment such as large storage tanks, the hulls of ships or the bodies of airplanes.

Although the normal and thrust force are produced by the same active component for LIMs, the forces can be manipulated independently through careful choice of operating slip-frequency product. Figure 2.9 shows the effects of changing slip frequency while keeping flux linkage constant [20].

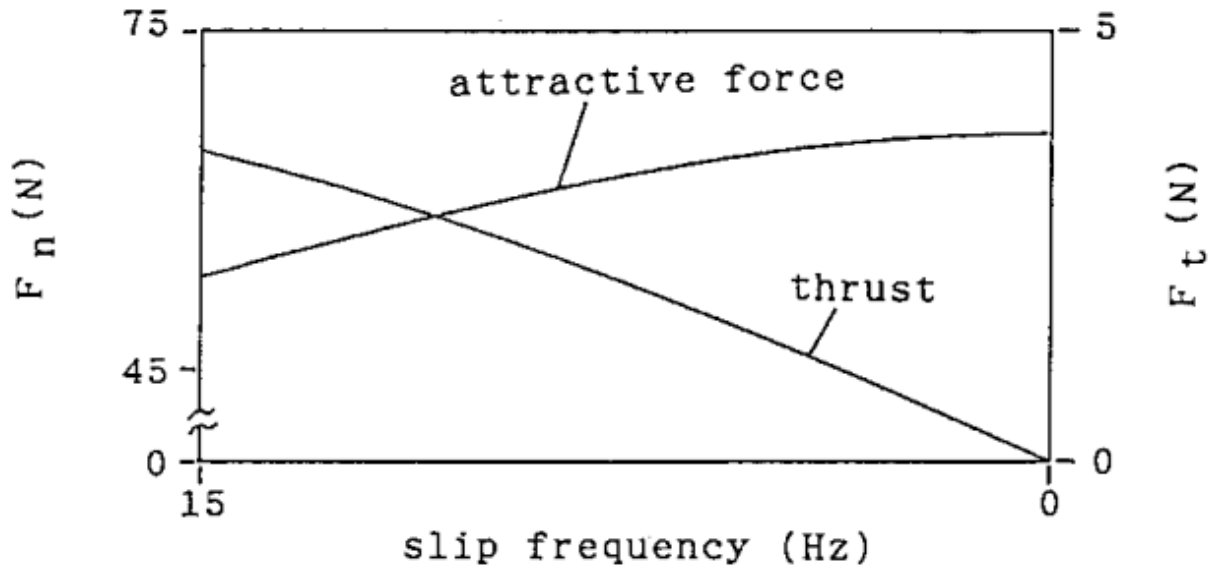


Figure 2.9 Effect of Changing Slip Frequency with Constant Flux Linkage [20]

Figure 2.9 uses a space vector control inverter to demonstrate the effects of different slip-frequency products on realized attractive and thrust forces. The thrust developed is shown to increase with slip-frequency whilst the attractive force is shown to decrease over the low slip-frequency region of 0 to 15Hz.

For this research, a steel backing plate was chosen to be used as the wall along which the vehicle climbs. Although steel has a magnetic permeability much less than that of iron, the LIM still exhibits an electromagnetic attraction to the steel reaction plate due to the magnetic permeability being greater than that of air.

For the vehicle to operate, the net force on the vehicle must be such that any acceleration tends to keep the vehicle in contact with the reaction and backing plates. In addition to the electromagnetic normal forces developed, the weight of the vehicle is an important factor of the system, producing a normal force component dependent on the angle of the surface operated on given by,

$$F_{nw} = -mg \cos \theta_b \quad (2.22)$$

where m is the vehicle mass, g is the acceleration due to gravity, θ_b is the angle of the backing plate relative to the horizontal plane and the minus sign indicates the force is in the natural direction of gravity (downwards for θ_b equal to zero). The net normal force towards the plate then becomes,

$$F_n = F_{na} - F_{nr} - F_{nw} \quad (2.23)$$

To climb an inclined surface, the net normal force must be sufficiently attractive to ensure there is enough friction to prevent the vehicle from sliding down the backing plate. Two locations where slippage may occur are the rubber tyre to aluminium reaction plate interfaces and the aluminium reaction plate to steel backing plate interfaces. The coefficient of static friction, μ_s , for aluminum on steel is approximately 0.61 [26], while that for aluminium to rubber is significantly larger and can be neglected. To prevent sliding, the friction force, F_f , must satisfy,

$$F_f = \mu_s F_n \geq mg \sin \theta_b \quad (2.24)$$

These forces can be easily understood graphically using Figure 2.10.

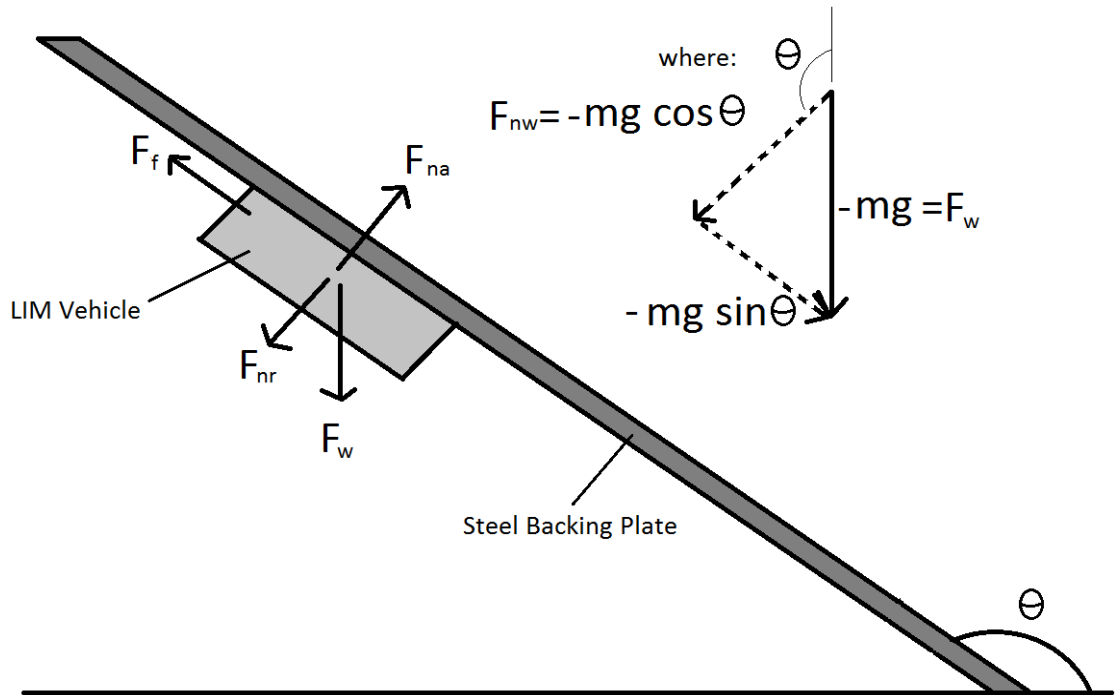


Figure 2.10 Forces Requiring Balancing in order to Prevent Slippage

Taking the derivative of Equation 2.24 with respect to θ_b dictates that the angle at which sliding most readily occurs is when,

$$-\mu_s mg \sin \theta_b = -mg \cos \theta_b \quad (2.25)$$

Equation 2.25 can be simplified and rearranged to give,

$$\theta_{b(peak)} = \tan^{-1} \frac{1}{\mu_s} \quad (2.26)$$

For $\mu_s=0.61$, this has solutions for any integer n at $2.12 \pm n\pi/2$ radians, or $121^\circ \pm n180^\circ$. This extremum denotes the point where the difference between the gravitational force acting to slide the vehicle along the plate and the frictional force resisting the motion is smallest, shown graphically in Figure 2.11.

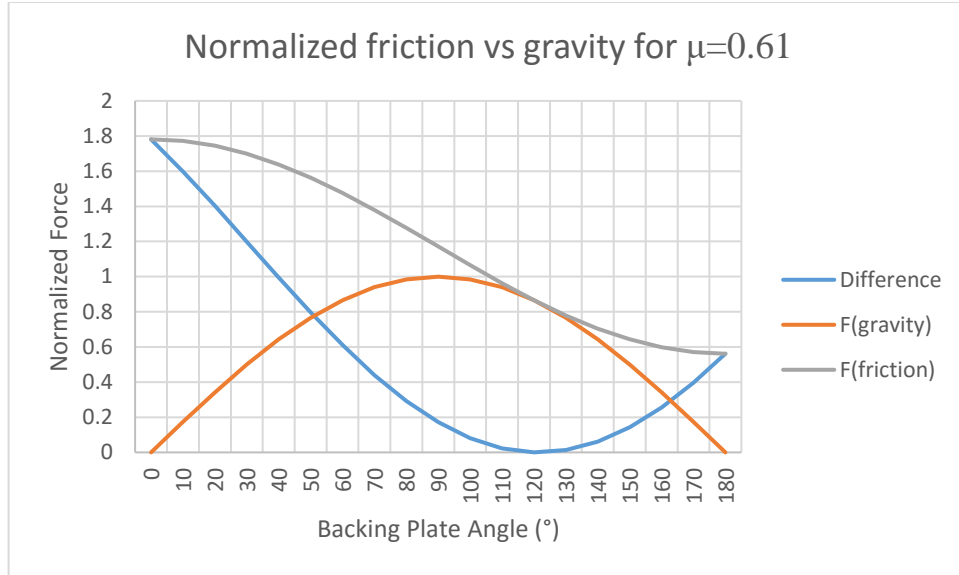


Figure 2.11 Normalized Friction vs Gravity

The net electromagnetic normal force required to prevent sliding at all angles can hence be found by solving Equation 2.27 for $F_{na} - F_{nr}$.

$$\mu_s(mg \cos \theta_{b(peak)} + F_{na} - F_{nr}) = mg \sin \theta_{b(peak)} \quad (2.27)$$

This gives the required net electromagnetic attractive/repulsive normal force as,

$$F_{na} - F_{nr} = 1.92mg \quad (2.28)$$

As the coefficient of 1.92 in Equation 2.28 is greater than 1, the net normal force to prevent sliding at all angles is also sufficient to ensure the vehicle remains attracted to the backing plate for all angles, making upside-down operation on ceilings or other such surfaces possible.

2.4 Turning

Vehicles require not only a method for propulsion but also a mechanism for steering the vehicle towards a desired direction. Although LIMs are only capable of

producing controlled motion in a linear direction, two stators situated a distance apart and with different drive parameters could produce different levels of thrust and hence also produce a differential torque which can be used for turning. Two independent drivetrains enable such a vehicle to drive forwards, reverse and steer.

In addition to producing turning torque, these drivetrains also produce turning scrub or friction from the skidding action that resists the turning torque. Turning torque and turning scrub can be easily visualized with the aid of Figure 2.12, which shows the lateral components of the force vectors for the most extreme turning case – on-the-spot 360° rotations.

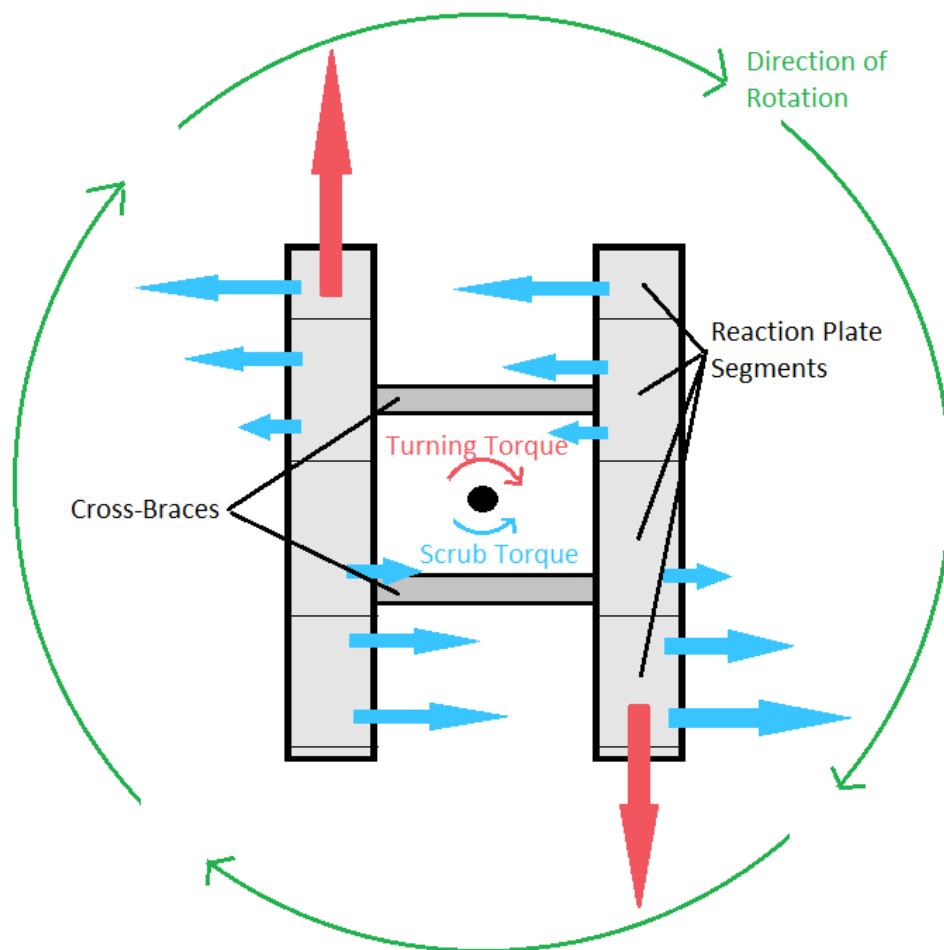


Figure 2.12 Skid-Steer Turning Torque vs Scrub Torque

The two frames holding the stators of the vehicle are completely independent of each other but held firmly together by cross-braces. The separation of the two stator frames determines the magnitudes of turning and scrub torques developed. Inefficient turning results if the tracks are located close to the turning point due to the large scrub torque produced.

Using very long cross-braces to create a very wide car is an effective technique for reducing the scrub torque; however, this results in a bulky vehicle requiring a wide backing plate to operate. An appropriate balance between maneuverability and vehicle size is best met by setting the cross-braces such that the vehicle width equals the vehicle length (determined by stator length plus wheel diameters). Such a scenario also gives increased space for the vehicle to carry a payload. Moreover, turning scrub acts to pull the reaction plate track off of the vehicle so the vehicle needs a mechanism to help hold the track in place.

Chapter 3 LIM Stator Design

The following sections summarize the steps undertaken when designing the physical, mechanical and electrical characteristics of the LIM stators and windings. The stators were designed with predetermined performance targets and were made as light as possible. The chapter concludes with results from preliminary thrust experiments, demonstrating the effect airgap has on thrust.

3.1 Design Requirements

Chapter 1 introduced the concept of the proposed vehicle propulsion mechanism and how the attractive force developed between the stator and steel backing could assist operation on inclined surfaces. As potential applications for the proposed vehicle include those in which the vehicle may be required to operate on vertical or even inverted surfaces, the three key design parameters are the maximum normal force, maximum thrust and vehicle mass, with emphasis placed on generating maximum thrust per unit mass.

The design targets proposed are summarized in Table 3.1.

Criterion	Target
Drive Voltage	<400V
Vehicle Length	<1m
Vehicle Mass	<30kg
Thrust	>300N
Normal Force	>300N

Table 3.1 Summary of Desired Vehicle Performance Objectives

The drive voltage parameter of Table 3.1 was chosen to be limited to 400V due to the availability of semiconductor devices that operate up to 400V and the ubiquity of 400V power supplies. The maximum values for vehicle mass and length were chosen such that the vehicle can be easily transported and be capable of being lifted by a single individual. The thrust and normal force developed must exceed the vehicle's weight, therefore the vehicle should, in principle, be constructed to be as light as possible.

3.2 Stator Structure

Design of the stator structure includes the number of pole-pairs, tooth width, tooth height, slot width, coil throw, number of phases, number of slots, winding layout and stator width.

Whilst increasing the number of phases can reduce the spatial harmonics of the MMF wave in the airgap [22], a longer stator length becomes necessary in order to accommodate the extra slots for the windings. A consumer 3-phase system was adopted and the number of pole pairs was allocated as two, allowing two wavelengths of the spatial MMF to propagate along the airgap while keeping the total length of the stator well within the target range. Increasing the number of pole pair decreases longitudinal end effects compared to a system with just one pole-pair as the spatial MMF takes on a more repetitious form.

The tooth width and slot width are important design parameters as they not only determine the pole pitch and overall stator length, but the tooth width must be selected such that the magnetic field does not become saturated, while the slot width must be sufficiently large to accommodate the numerous turns of the windings. If the stator teeth

become saturated, then the magnetic field will not increase appreciably with increased current in the windings, limiting the amount of power available to produce thrust. Meanwhile, if the number of turns of the windings is small, a greater current is required to produce the same flux linkage, resulting in greater resistive losses.

Stators of induction machines are usually constructed using several layers of non-grain oriented silicon steel, punched from a steel sheet to preserve their magnetic properties [27]. Custom punching and blanking dies can be used cut out the desired stator teeth shapes precisely, however, an assembly of transformer laminations were instead decided upon to construct the stators to allow for flexibility of design, post-design variations and optimization. Additionally, the holes in transformer laminations were use advantageously to aid in stator assembly and mounting to the vehicle chassis.

Figure 3.1 shows two E-shaped transformer laminations side-by-side to illustrate how the slot height (h_s), tooth height (h_t), slot width (w_s) and tooth width (w_t) are measured.

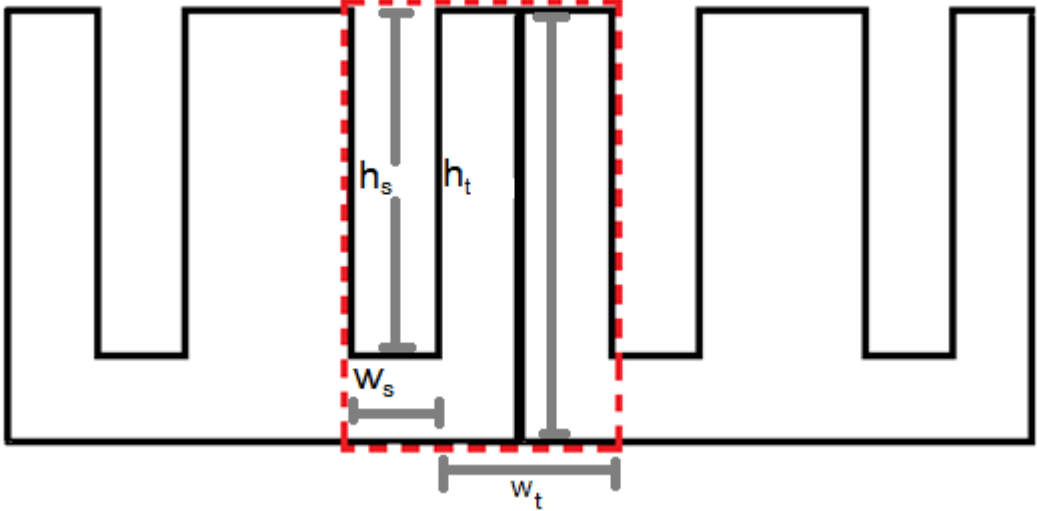


Figure 3.1 Single Slot/Tooth Pair Constructed with E-I Transformer Laminations

Transformer laminations come in a range of sizes, but industrial standards dictate that they maintain the same steel area to slot area given by,

$$\frac{steel}{slot} = \frac{(w_t + w_s)h_t - w_s h_s}{w_s h_s} = 3 \quad (3.1)$$

To reduce stator weight, the stator tooth width can be reduced to equal the stator slot width, as seen in 3-phase transformer laminations. This allows the steel to slot ratio for standard size transformer laminations to be reduced to 5/3, as per Equation 3.2.

$$\frac{steel}{slot} = \frac{(0.5w_t + w_s)h_t - w_s h_s}{w_s h_s} = \frac{5}{3} \quad (3.2)$$

The steel to slot ratio can be even further reduced by utilizing I-shaped laminations and trimming E-shaped laminations into I-shaped sections. Standard EI-76.2 laminations were decided upon for the stator structure as the tooth width, slot height and slot width results in a stator height and length that fit well with the target objectives. The dimensions of each I-shaped section are indicated in Figure 3.2. The I-shaped segments were stacked using a tessellating pattern, offset by one tooth segment for each layer to add rigidity to the finished stator. This pattern using 3 different I-shaped segments of equal width allows for a steel to slot ratio of 1.5 (by inspection, ignoring holes). Including the holes and accounting for the presence of the protruding 12.7mm x 12.7mm mounting tab that occurs once per tessellation, the effective steel to vacant space ratio is 1.49.

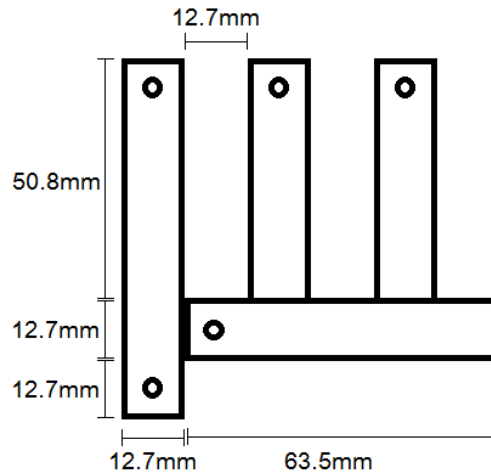


Figure 3.2 LIM Tooth and Slot Tessellation Pattern and Dimensions

A stator using the pattern of Figure 3.2 is capable of holding the same number of winding turns as the arrangement shown in Figure 3.1, made purely of E-laminations with the same slot size, but has half the weight due to the halved steel/slot ratio. Further weight losses are also realized as the decreased tooth width required as shorter length of wire per turn, decreasing the weight contribution of the windings. However, the simple rectangular slot shape causes the flux density to increase at each of the sharp corners as the flux lines complete their magnetic circuit, causing non-uniform flux distribution within the stator and additional losses. To illustrate the bunching a flux lines at the corners, the magnetic flux density distribution for the designed stator with 7A RMS phase currents applied was simulated using FEM software to produce the image in Figure 3.3.

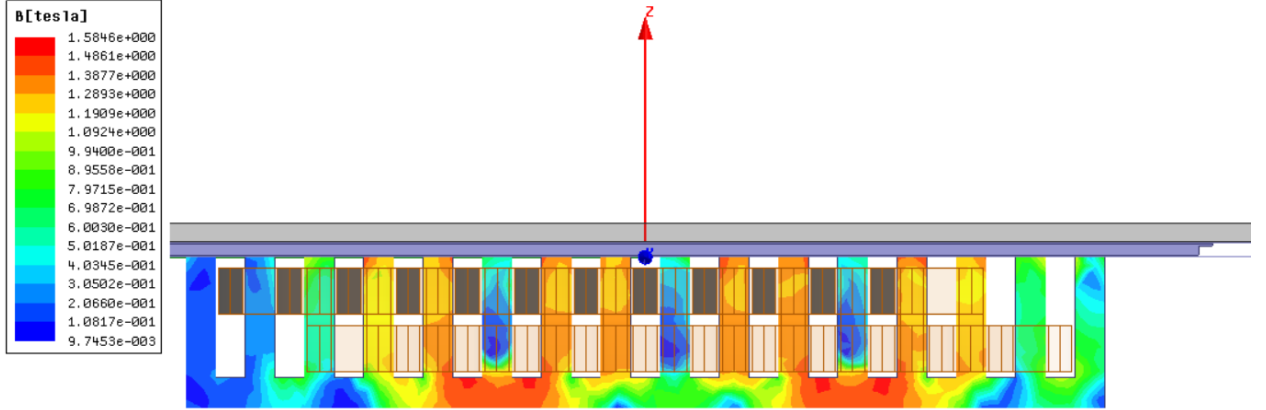


Figure 3.3 Increased Flux Density at Sharp Corners

The red in Figure 3.3 indicates a high flux density of 1.5T in the vicinity of the slot base corners, contrasting the blue regions with a low flux density of approximately 0.1T. The bunching of flux lines propagates down the length of the stator with the MMF wave. Using rounded corners at the slot base may help to reduce the concentration of flux, limit saturation, decrease the required magnetizing current and improve efficiency [28].

3.3 Construction of Windings

The design parameters of the windings must be decided upon in order to determine the number of stator slots/teeth that are required. The purpose of the windings is to produce a pure travelling sinusoidal MMF [17] given by Equation 3.3.

$$F(x, t) = F_m \cos\left(\frac{\pi}{\tau} x - \omega_1 t - \theta_0\right) \quad (3.3)$$

where F_m is the maximum value of the MMF wave, τ is the spatial half period, x is the longitudinal distance along the stator, ω_1 is the angular frequency of phase currents and θ_0 is the initial angular position at $t = 0$.

Equation 3.3 can be decomposed for 3-phase systems into

$$F(x, t) = \frac{2}{3} F_m \left[\begin{array}{l} \cos\left(\frac{\pi}{\tau}x - \theta_0\right) \cos(\omega_1 t) + \cos\left(\frac{\pi}{\tau}x - \theta_0 - \frac{2\pi}{3}\right) \cos\left(\omega_1 t - \frac{2\pi}{3}\right) + \\ \cos\left(\frac{\pi}{\tau}x - \theta_0 + \frac{2\pi}{3}\right) \cos\left(\omega_1 t + \frac{2\pi}{3}\right) \end{array} \right] \quad (3.4)$$

As such, an ideal MMF waveform can be represented by three single phase windings, separated in both time and space by $2\pi/3$ radians.

With the number of pole-pairs to be used for the stator decided upon as two, the use of single or double layer windings and the number of slots/pole/phase were the next design considerations to be determined. As double layer windings have an advantage over single layer windings due to the utilization of double the number of coils, double layer windings was chosen for the stator. The numerous coils aid the production of a sinusoidal MMF and are generally used except when the slot openings are large compared with the length of the airgap [29].

The number of slots/pole/phase to be used is dependent on coil throw (or coil span) and affects the shape of the MMF waveform in the airgap. The MMF waveform that would be produced for coil throws of $y = 1, 2$ and 3 are calculated graphically [17] and presented in Figure 3.4.

$$F = F_A(x, t) + F_B(x, t) + F_C(x, t)$$

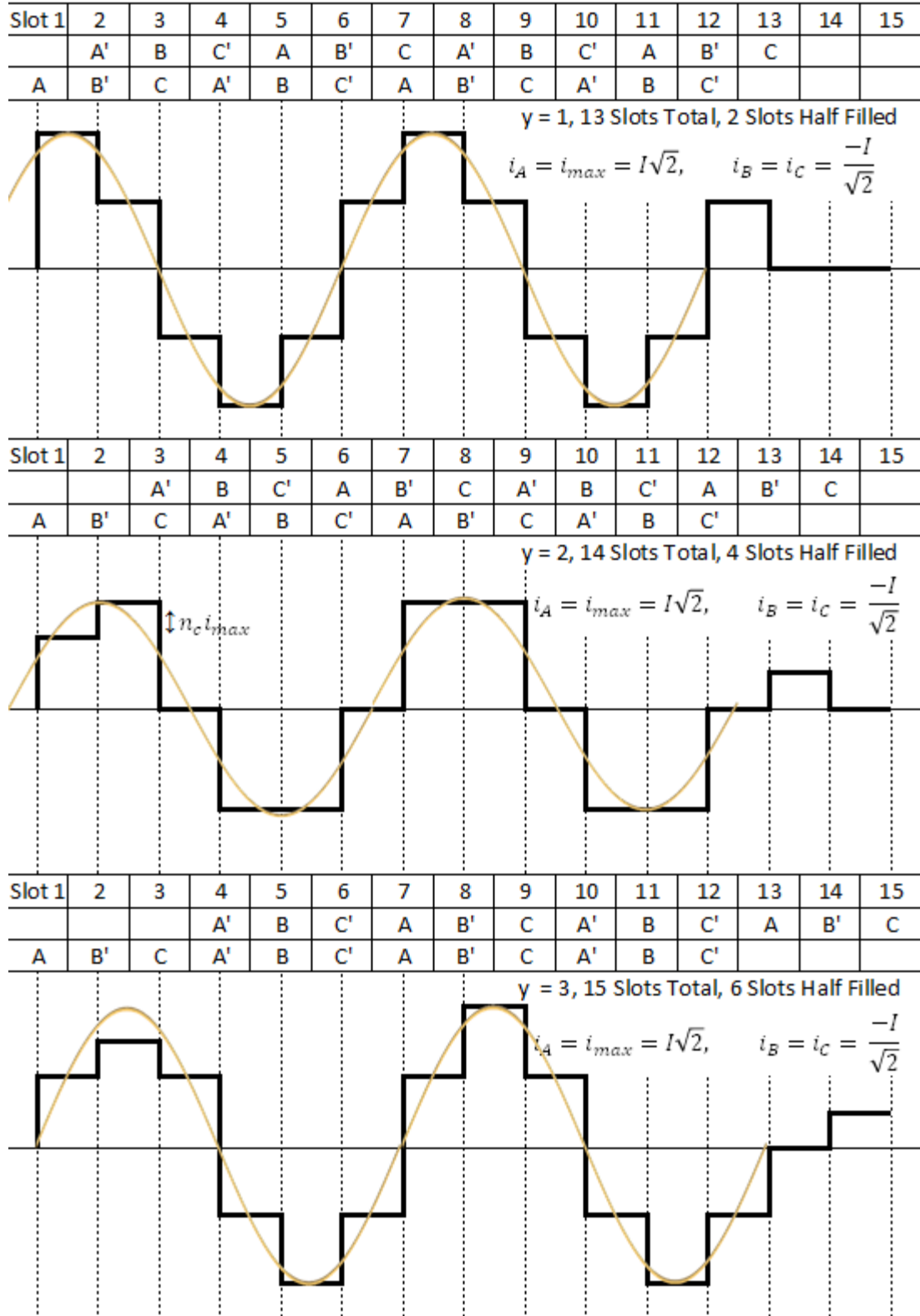


Figure 3.4 Total MMF Waveform for Different Coil Throw

The travelling MMF waveform produced in Figure 3.4 resembles a rectilinear sinusoid for all 3 coil throws calculated. A coil throw of 3 was selected due to the winding flexibility offered by the 6 half-filled slots and the maximized stator area (length) that interacts with the reaction plate to increase the thrust developed, as evidenced by FEM simulation.

The final design parameter is the conductor diameter. Combining Equations 2.9 and 2.15 gives,

$$F_x \propto (NI_1)^2 \quad (3.5)$$

Equation 3.5 implies that to maximize the thrust developed (ignoring other parameters), the product of the number of turns and phase current should be maximized. To carry a large current, the conductor diameter could be increased, giving a larger cross-sectional area in which current can flow. However, the larger conductor area leaves less room within the fixed slot area, causing the number of turns to decrease proportionally. As such, the maximum thrust achievable for a fixed slot area is approximately constant.

The reactance of each coil is given by,

$$X_L = \omega L = \omega \mu \frac{N^2 A}{l} \quad (3.6)$$

where A is the area of the coil and l is the length. Consequently, an increased number of turns leads to a greater impedance and requires a larger applied voltage to achieve the same phase current. This is significant as the design specifications in Table 3.1 dictate that the inverter is to operate at voltages no higher than 400V. Additionally, windings made of thinner conductors also result in greater resistive losses in accordance with the equivalent circuit of Figure 2.8, generating heat that may limit operability of the

vehicle. Wire with a conductor diameter of 1.00mm was selected for use with the designed stator due to the sufficiently low resistance of approximately $21\Omega/\text{km}$ [30].

The finalized design parameters for each of the two custom LIM stators are shown in Table 3.2, below.

Number of turns	520 per phase
Number of phases	3 phases
Number of poles	4 poles
Number of slots/pole/phases	5/4
Stator Length	410mm
Stator Width	45mm
Tooth Width	12.7mm
Slot Height	50.8mm
Slot Width	12.7mm
Slot Pitch	25.4mm
Pole Pitch	77mm
Conductor Diameter	1.0mm
Average Phase Inductance	35mH
Average Phase Resistance	3.3Ω
Connection Type	Star (Wye)

Table 3.2 LIM Stator Physical Parameters

3.4 Preliminary Experimental Results

An experimental rig was constructed to test the performance of the two stators compared to the performance from FEM simulations and analytically calculated results. Later described in section 4.3, the output phase voltages can be controlled via software

to be a desired proportion of the DC bus voltage applied. The RMS voltages expressed in this section are those calculated from,

$$V_{rms} = \frac{1}{\sqrt{2}}A(V_{DCBUS} - 2V_{f,rect}) \quad (3.7)$$

where A adopts a value between 0.01 and 0.95 and $V_{f,rect}$ is the junction temperature dependent forward voltage drop of the 3-phase rectifier at the input, equal to approximately 2.5V.

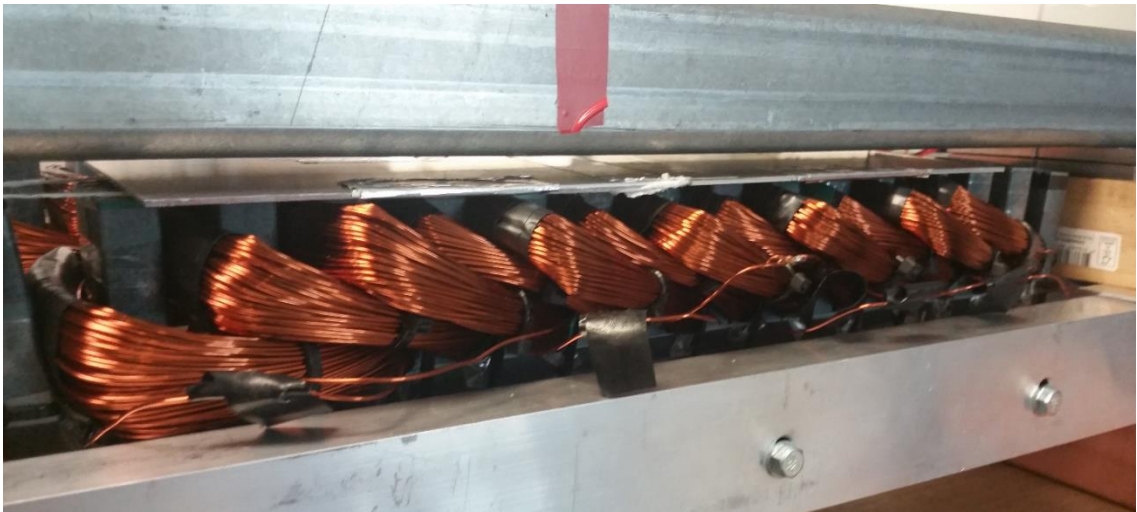


Figure 3.5 Experimental Setup for Testing Stator and Reaction Plate Parameters

The electrical parameters of each stator, including the relationships between voltage, current, airgap length and thrust, were tested using the experimental setup shown in Figure 3.5, whereby the stator was held firmly in place using two aluminium extrusions while a rectangular steel extrusion with a width of 90mm and 6mm thick walls performed the role of the steel backing plate. Wooden blocks are leveraged against the aluminium extrusions and used together with spacers to give fine control of the airgap.

The airgap between the stator and backing plate plays an important role in LIM systems as it greatly increases the reluctance of the magnetic circuit. Without the presence

of a reaction plate, the $R'_{2/s}$ branch of the equivalent circuit of Figure 2.8 disappears, giving the effective equivalent circuit of Figure 3.6.

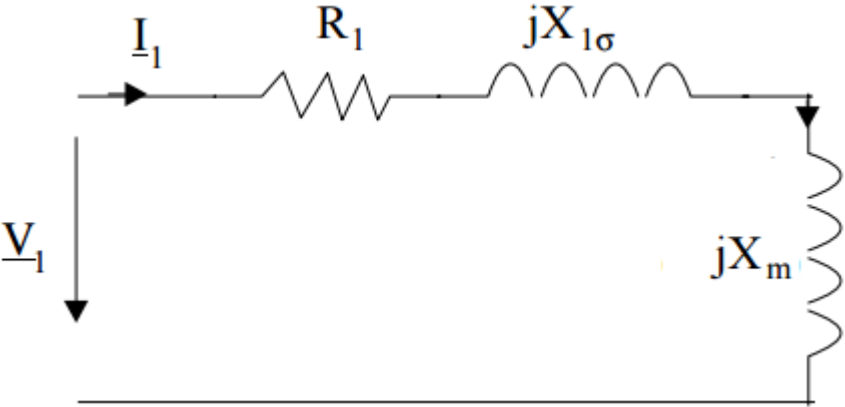


Figure 3.6 Per Phase Equivalent Circuit without Reaction Plate

As the $R'_{2/s}$ branch of the per-phase equivalent circuit that represents the reaction plate is not present in Figure 3.6, there is only one return current conduction pathway instead of two, so the magnitude of phase current for a specified applied voltage decreases. The converse occurs when the airgap is made larger. As the airgap increases, the increasing reluctance of the airgap decreases the magnetizing reactance via Equation 2.8, resulting in greater phase current for a given phase voltage applied. This effect is demonstrated in Figure 3.7.

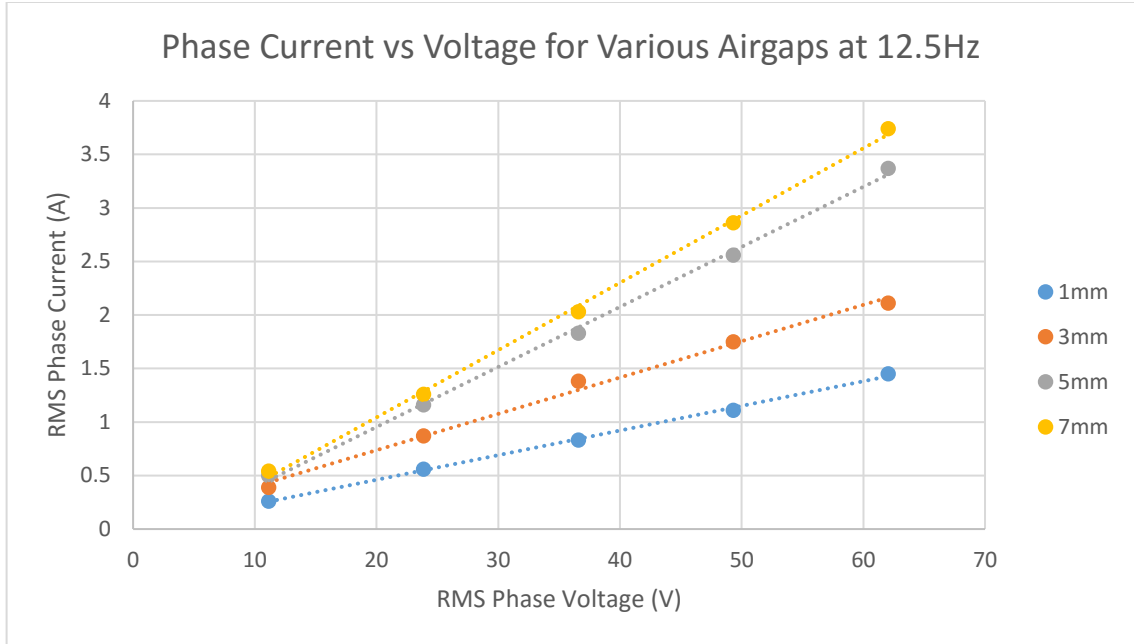


Figure 3.7 Phase Current vs Applied Voltage for Different Airgaps

Figure 3.7 confirms the relationship between applied phase voltage and current is linear with a gradient equal to the inverse of the phase impedance via ohms law. The resistance of the windings and stator reactance are independent of the airgap length so from Figure 3.6 it is evident that the changing phase impedance is due to the changing magnetizing reactance. The resistance of each phase is known to be approximately 3.3Ω , allowing $X_{l\sigma}$ and X_m to be calculated using the equivalent circuit of Figure 3.6 and gradients of Figure 3.7. For a drive frequency of 12.5Hz, this approximates $X_{l\sigma}$ to be 9Ω and X_m for the smallest 1mm airgap as 41Ω , decreasing as the airgap grows larger.

The net normal force produced by the stator is also of great interest for the potential application as a steel-plate climbing vehicle. Equation 2.18 indicates the attractive force dominates over the repulsive force for stator designs with low Goodness Factor. Figure 3.8 shows experimental results of normal force measurements.

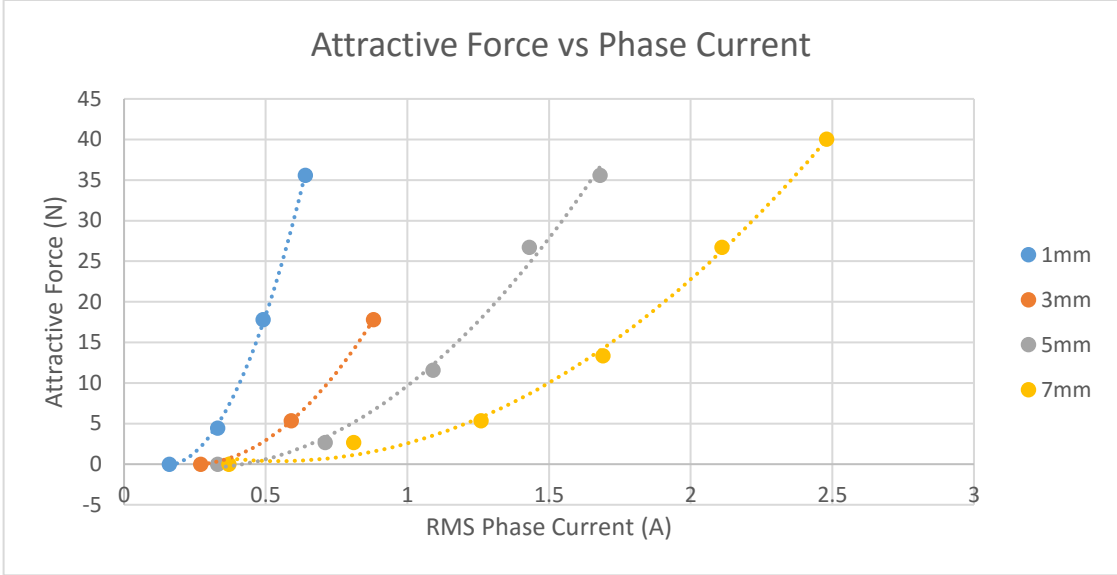


Figure 3.8 Attractive Force vs Phase Current for Different Airgaps (w/o reaction plate)

The curves of best fit found in Figure 3.8 indicate the attractive force increases proportionally to the square of the current density through the windings, consistent with Equation 2.18.

Chapter 4 Inverter Design and Development

This chapter describes the design process and operating principle of the dual 3-phase inverter and LIM vehicle controller board, including an explanation of the imbalanced phase compensation technique implemented in the control software.

4.1 Overall Design

The controller board was designed using an ATXMEGA16D4 microcontroller at the heart and consists of the components outlined in Figure 4.1.

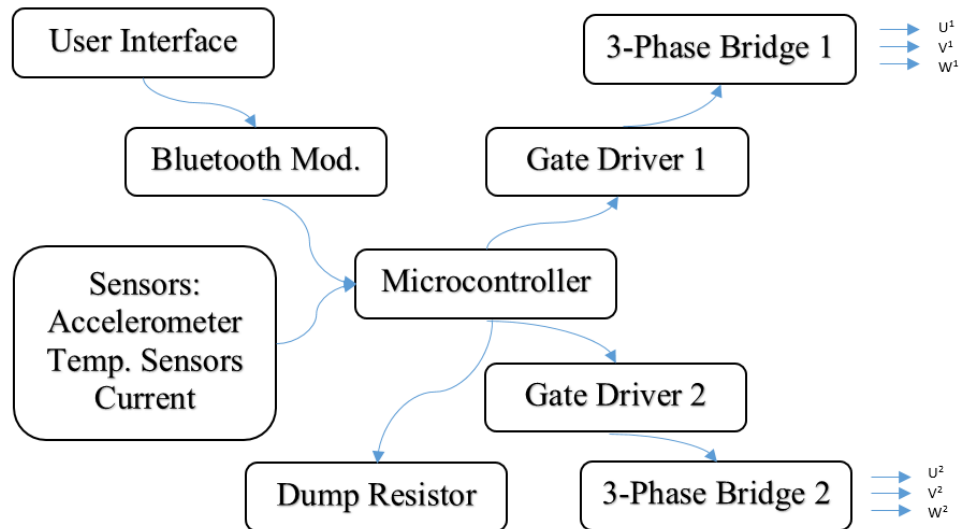


Figure 4.1 Controller Block Diagram

The controller has no physical buttons so any communication by the operator takes place via a Bluetooth connection. A bespoke Android-based app, shown in Figure 4.2, allows the controller to be accessed from anywhere in the nearby vicinity using an Android mobile phone after being granted permissions by entering a PIN number. Sensors on the board include a tri-axis 10G accelerometer/gyroscope for orientation and thrust sensing, temperature sensors on the board and in both 3-phase bridge modules, and shunt

resistors to allow the total current through each bridge to be measured. The 3-phase bridge modules use the topology from in Figure 2.3.

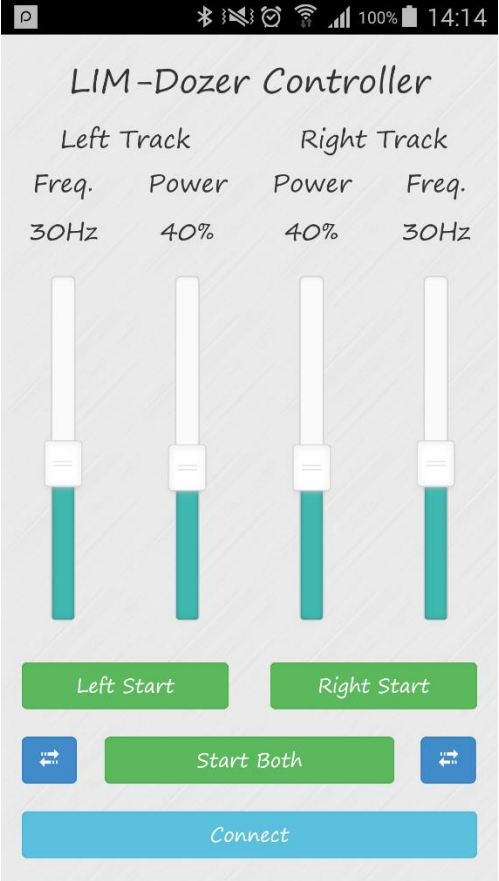


Figure 4.2 Screenshot of the LIM Controller App Interface

The dump resistor is an external 25Ω 50W resistor fastened to the aluminum chassis of the vehicle to aid with heat dissipation and is used to “dump” excess energy that would otherwise be stored on the DC link capacitor when the load operating conditions change as discussed in subsection 2.1.2.3.

Six outputs (3 high side, 3 low side) from the microcontroller are connected to each gate driver allowing the switching of the 3-phase bridge modules to be controlled. These 3-phase bridge modules are also connected to three output terminals each, with each terminal forming one phase of the 3-phase output system.

In addition, four coloured LED lights on the board also allow visual verification of controller status. The function of each LED light is described in Table 4.1.

LED Color	Application
Red	Heartbeat indicator that blinks every 500ms to show normal program execution.
Yellow	Excess Current indicator that is illuminated when stator output is disabled due to excessive current being drawn.
Green	Excess Temperature indicator that is illuminated when stator output is disabled due to high IGBT module temperatures. Blinks if output is disabled due to excessive winding temperature.
Blue	Command Received indicator that is illuminated for one second when a command has been received via Bluetooth connection.

Table 4.1 Controller LED Functions

The high-brightness coloured LEDs enable the operator to know the status of the vehicle at a glance during operation and assists in fault-finding efforts. Several unused I/O pins from the microcontroller are ported to an expansion header for future use with additional sensors. Figure 4.3 shows a snapshot of the controller board with labels to indicate some of the components.

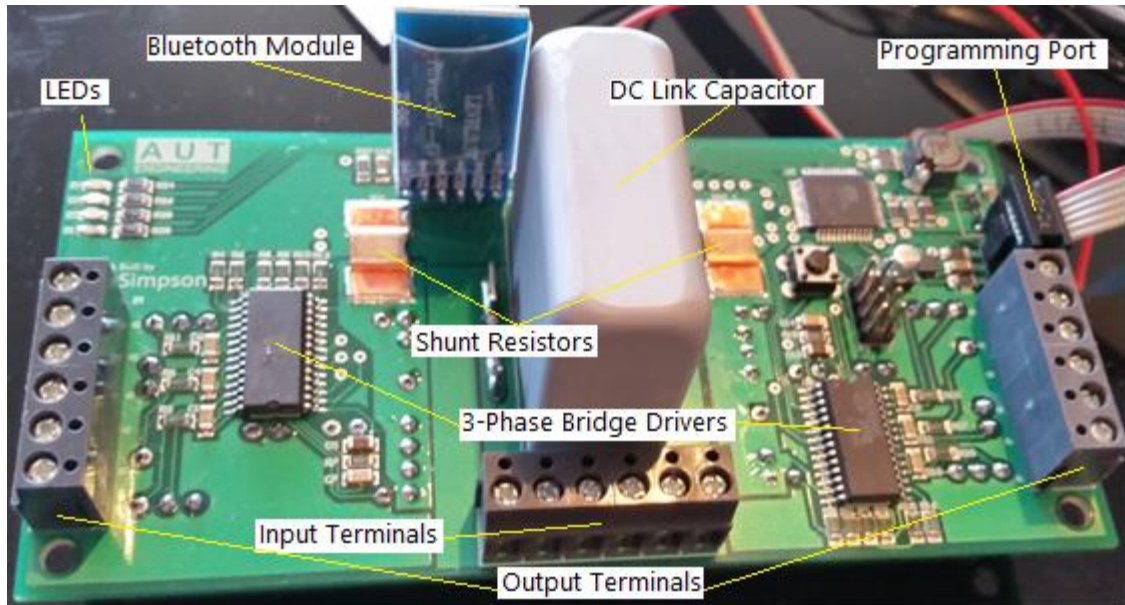


Figure 4.3 Physical View of Controller Board

4.2 Direct Digital Synthesis (Sine PWM)

A direct digital synthesizer uses a fixed-frequency reference sine wave and generates a time varying signal in digital form, performing a digital-analog conversion to produce an analogue signal [31]. To do this, the input sinusoidal reference wave and a high frequency triangular or sawtooth carrier signal are applied to a comparator which switches its output depending on which input is greater. This effectively generates a PWM signal with frequency equal to the input carrier frequency but with sinusoidal-varying duty cycle. This switching technique is illustrated in Figure 4.4.

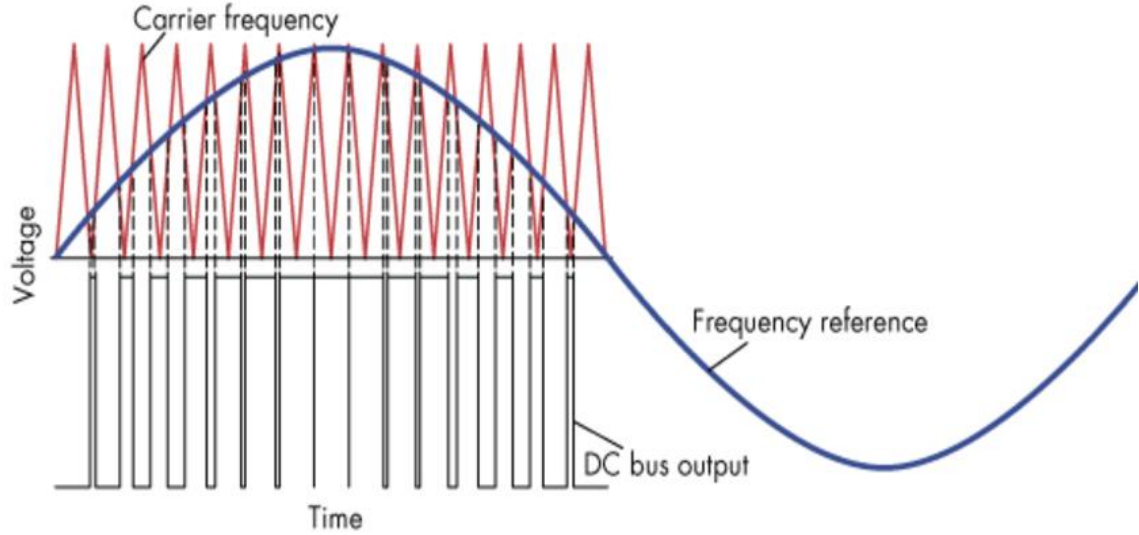


Figure 4.4 Direct Digital Synthesis using Hardware [32]

Using a microcontroller, the same time-varying duty cycle seen Figure 4.4 can be calculated mathematically once using the sine function and stored in a lookup table for reference. To reproduce the pattern on an output, the microcontroller should be configured to output the 12 required PWM signals to the 3-phase bridge gate drivers in capture-compare mode at the desired switching (carrier) frequency. Capture-compare and overflow interrupts must also be enabled.

A sine lookup table of length n can then be calculated for each data entry, d_i , by

$$d_i = 0.5 \left(\sin \frac{2\pi i}{n} + 1 \right) \quad (4.1)$$

where $0 \leq i \leq n - 1$. The data entries can then be scaled to form microcontroller register values appropriate to the desired carrier frequency using,

$$r_{d_i} = f_c d_i \quad (4.2)$$

where f_c is the carrier frequency and r_{d_i} is the scaled register data entry for the i th component of the sine wave.

When a PWM timer overflow interrupt occurs, the microcontroller increments counters pointing to entries in the table situated $n/3$ entries apart, representing three phases offset by $2\pi/3$ radians, then sends the corresponding register data entries to the PWM buffer. The high-side gate output's capture-compare channels initially give a high logic level output, but transition to low level when the capture-compare condition occurs. The low-side gate outputs do the opposite.

The relationship between the lookup table length and the carrier frequency determines the output frequency as per Equation 4.3.

$$f_{out} = \frac{f_c}{n} \quad (4.3)$$

Accordingly, a desired change in output frequency demands a change in either the number of samples per cycle, or the carrier frequency. As both RAM and program memory available for storing the lookup table is limited in the microcontroller, it is preferable to have a fixed lookup table length to ensure the memory capacity is not exceeded. Consequently, the carrier frequency is changed while keeping the number of samples fixed in order to effect a change in output frequency in accordance with Equation 4.3.

The length of the lookup table length, n , must be relatively large so that a sufficient number of samples are present in the output wave form for it to be well-formed and have minimal harmonic distortion. However, the tables must also be small enough such that two such tables can be stored within the memory available in the microcontroller. Two lookup tables are required to allow each of the two stators of the vehicle to be driven at frequencies independent of each other. Additionally, the number of samples must be

small enough that carrier frequency for the highest intended output frequency does not cause excessive burden to the load switching elements or introduce large switching losses.

The effect that the number of samples has on the harmonic distortion of the output current waveform is illustrated in Figure 4.5, where a single 50Hz phase is output from the controller and filtered through a low-pass filter with a 100Hz cut-off frequency. The three waves are for $(n = 7, f_c = 350\text{Hz})$, $(n = 14, f_c = 700\text{Hz})$, $(n = 28, f_c = 1400\text{Hz})$.

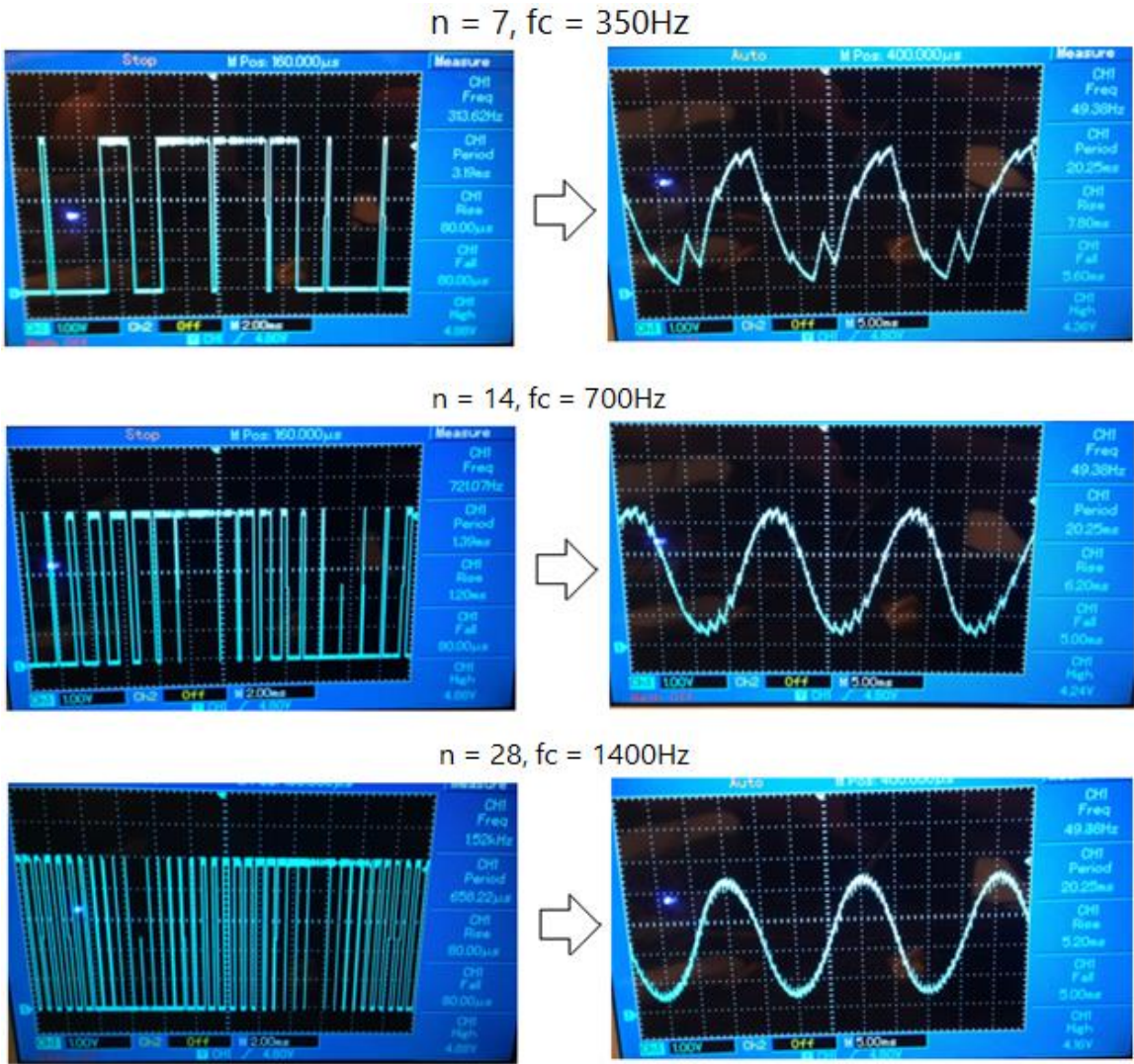


Figure 4.5 Effect of Number of Samples on Filtered Output Waveform

Figure 4.5 demonstrates the effect of using an RC low-pass filter to convert the sine-PWM waveform output into a more recognizable quasi-sinewave. The resistor of the RC filter introduces large losses for loads during high currents making it unpractical for use with the controller. Instead, an LC low-pass filter is can be used. However, for highly inductive loads the filter can be altogether omitted due to the high impedance conduction pathway at high frequency, due to the linear increase in impedance with frequency given by,

$$Z_L = \omega L \quad (4.4)$$

where Z_L is inductive impedance and L is the winding inductance.

The high impedance effectively filters out most of the carrier frequency while retaining most of the fundamental frequency, allowing an oscillating sinusoidal current to flow through the LIM stator windings even when an unfiltered sine-PWM voltage waveform is applied.

The 3-phase sinusoidal current waveform through the stator windings is verified in Figure 4.6 for a 50Hz output frequency, 4.5kHz carrier frequency and 90 samples per wavelength, measured using current probes and a 4-channel digital storage oscilloscope.

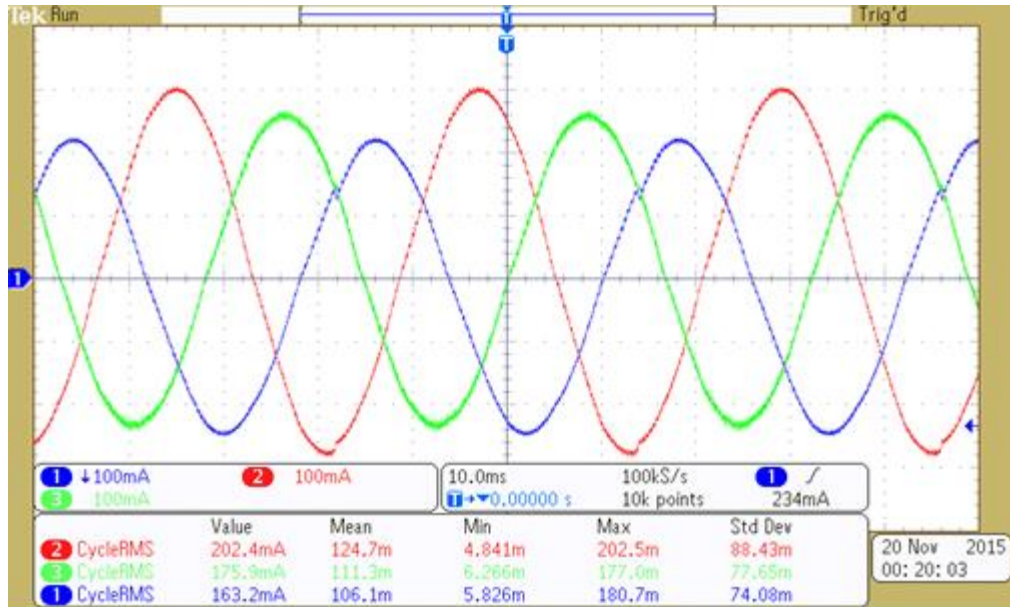


Figure 4.6 3-Phase 50Hz Current Waveform with Inductive Load

The total harmonic distortion of each phase current was measured using the FFT function of the oscilloscope and found to be approximately 2.5%, indicating the harmonics do not occupy a large portion of the signal, even for this unfiltered output case.

The most noticeable feature of Figure 4.6 is that the phase currents are unbalanced. This imbalance is a direct result of the three phase resistances and inductances being unequal. Software compensation for this imbalance is addressed in the following section.

4.3 Software Amplitude and Phase Control

The synchronous speed of LIMs is proportional to the drive frequency, while the thrust developed is proportional to flux linkage and current applied to the windings. For a fixed output frequency, the magnitude of the current is proportional to the magnitude of the applied voltage wave and length of time that voltage is applied. This allows the flux linkage and current amplitude to be effectively controlled in software for a given

frequency by changing the maximum ratio of high-output to low-output time of the switches of the 3-phase bridges. Manipulation of voltage waveform applied time in order to keep the flux linkage constant as drive frequency changes is the basic working principle for Volts-per-Hertz drive control.

Equation 4.2 can be modified to allow the drive voltage to be manipulated for a fixed DC input voltage by including an amplitude coefficient, A, giving,

$$r_{d_i} = A f_c d_i \quad (4.5)$$

where, $0 \leq A \leq 1$.

4.3.1 Current Waveform Distortion

Attempting to drive the stator windings using the controller with the maximum possible amplitude coefficient ($A = 1$) resulted in a distorted current waveform with a transient around positive peak, as shown in Figure 4.7.

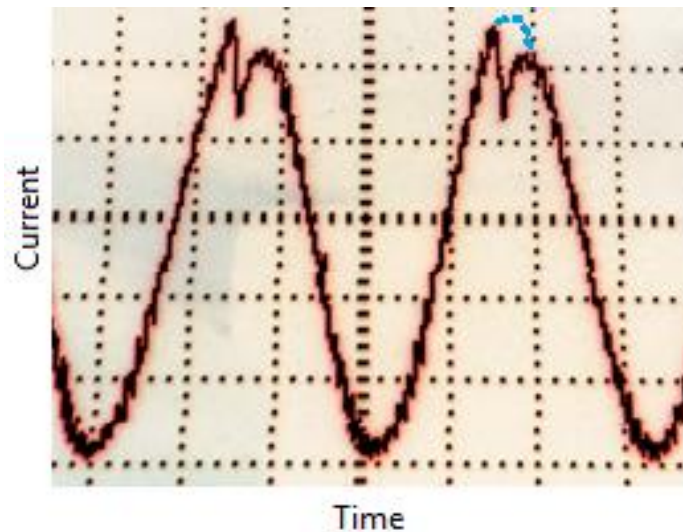


Figure 4.7 Current Waveform Distortion for 100% Amplitude Coefficient

Figure 4.7 shows the transient as a collapsed positive peak. The second peak has been colored in blue to show the expected shape of the waveform. The transient due to the high-side bootstrap capacitors failing to deliver sufficient charge to turn the high-side gate on or to keep the gate on sufficiently long. The bootstrap capacitors store charge from the 12V power rail and use the charge to boost the high-side IGBT gate voltage with reference to the emitter pin, allowing the IGBT to be turned on. The bootstrap capacitor for each leg of the bridge is charged whenever the low-side IGBT of that leg is on, through the path shown in Figure 4.8.

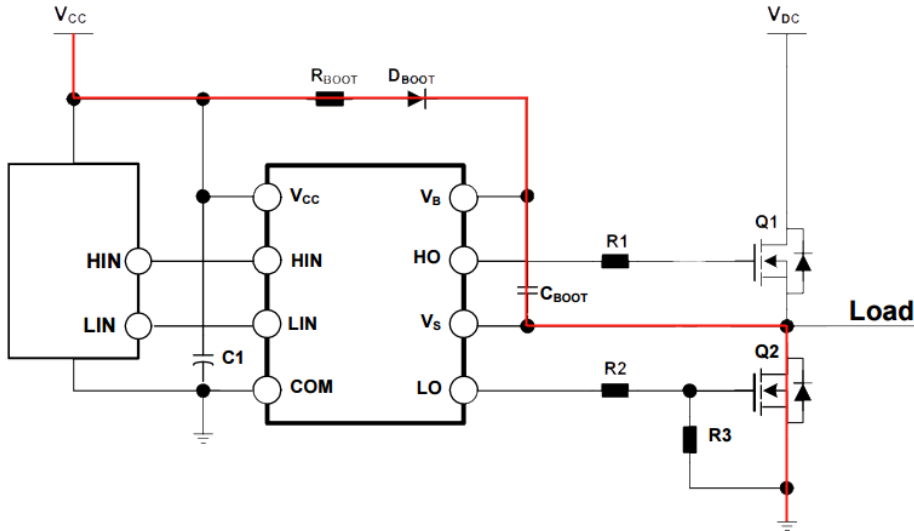


Figure 4.8 Bootstrap Capacitor Charging Path

To avoid the waveform distortion, the bootstrap capacitor must be selected subject to Equation 4.6 [33].

$$C_{BOOT} = \frac{Q_{GATE} + (I_{LKCAP} + I_{LKGE} + I_{QBS} + I_{LK} + I_{LKDIODE})t_{ON} + Q_{LS}}{V_{CC} - V_F - V_{GEMIN}} \tag{4.6}$$

where Q_{GATE} is the total gate charge; I_{LKGE} is the gate-emitter leakage current; I_{QBS} is the bootstrap circuit quiescent current; I_{LK} is the bootstrap circuit leakage current; $I_{LKDIODE}$ is the bootstrap diode leakage current; t_{ON} is the low-side on time; Q_{LS} is the gate driver internal level shifter charge ($3nC$); V_F is the bootstrap diode forward voltage; and V_{GEMIN} is the minimum gate-emitter voltage required to turn the IGBT on.

Accordingly, when the peak amplitude for each phase is being output, the low-side on time, t_{ON} , approaches zero, preventing the bootstrap capacitor from charging. Soon after, the charge on the gate is dissipated, causing the high-side IGBT to switch off. When the duty cycle drops such that the bootstrap capacitor has time to sufficiently charge, operation recommences as expected. This causes the distortion in the waveform seen in Figure 4.7.

A workaround to address this problem was to limit the maximum duty cycle ratio by using amplitude coefficients within the range of $0 \leq A \leq 0.95$. This eliminates the transient in the current waveform but reduces the RMS voltage applied to the windings.

4.3.2 Imbalanced Phase Compensation

Precisely wound stator windings can be readily achieved using automated equipment or machinery in a production environment, but the winding process is much more arduous when developing a proof-of-concept vehicle. The asymmetry of the slot geometry caused by some half-filled slots and some completely filled slots makes maximizing the slot fill factor while attempting to keep the number of turns in the windings equal a challenging task. These challenges resulted in differing secondary flux linkages and impedances of each phase of the stator windings, giving the imbalanced current waveforms presented in Figure 4.6.

The phase angle between voltage and current waveforms for a reactive load is given by,

$$\theta = \tan^{-1} \frac{X_L - X_C}{R_1} \quad (4.7)$$

Equation 4.7 indicates that the voltage waveform leads the current for an inductive load, but the phase angle can be minimized with the introduction of a power-factor correction capacitor. For a non-capacitive load, this equation further simplifies to,

$$\theta = \tan^{-1} \frac{X_L}{R_1} \quad (4.8)$$

Equation 4.8 states that the phase angle for each phase depends on the ratio of inductive reactance and resistance. This 3-phase LIM stators for the vehicle are connected in a star (or Wye) arrangement, giving the phase voltages by,

$$v_x = V_m \sin(\omega t + \alpha_x) \quad (4.9)$$

where $x = \{a, b, c\}$ represents each of the 3 phases and the phase shift α_x is chosen to be 0, $2\pi/3$ and $4\pi/3$ radians. For steady-state sinusoidal operation, the phase currents are given by,

$$i_x = I_m \sin(\omega t + \alpha_x + \theta_x) \quad (4.10)$$

where θ_x represents the voltage-current phase angle given by Equation 4.8 for each phase $x = \{a, b, c\}$. For optimal operation the angle between phases should be $2\pi/3$ radians, but the value for θ_x varies for each respective phase with an unbalanced loads. A power factor correction capacitor can be used to decrease θ_x to nearly zero for industrial applications.

With software-based amplitude and phase control, each phase has the capacity to have its own amplitude coefficient and relative phase shift, implemented by modifying

the relative lookup table indices in software. To achieve the optimal $2\pi/3$ radians difference in phase angle without the use of power correction capacitors, a new variable can be introduced as per Equation 4.11.

$$\alpha_x^* = \alpha_x + \theta_x \quad (4.11)$$

α_x can be chosen such that α_x^* becomes equal to 0, $2\pi/3$ or $4\pi/3$ radians, negating the effects of the frequency dependent phase shift due to imbalanced windings. In other words, phase current balancing can be achieved despite differences in physical winding construction by outputting the drive voltage with phase shifts separated by angles not equal to $2\pi/3$ radians. This can be implemented in software if the resistance and inductance of each phase is known. This balancing process can be conducted visually using an oscilloscope for a single frequency, but as the inductive reactance is frequency dependent, the phase factor should be calculated analytically using Equation 4.8. Once calculated, α_x^* can be used to map the lookup table index using

$$a_x = \frac{\alpha_x^*}{2\pi} n \quad (4.12)$$

and rounding to the nearest integer. Equations 4.8, 4.11 and 4.12 can be combined and rearranged to calculate the lookup table index using,

$$a_x = \frac{n}{2\pi} \left(\alpha_x^* + \tan^{-1} \frac{\omega L_x}{R_x} \right) \quad (4.13)$$

where L_x and R_x are respectively the inductance and resistance of that particular phase and α_x^* is 0, $2\pi/3$ or $4\pi/3$. The effects of the software-based phase-tuning can be noted in Figure 4.9.

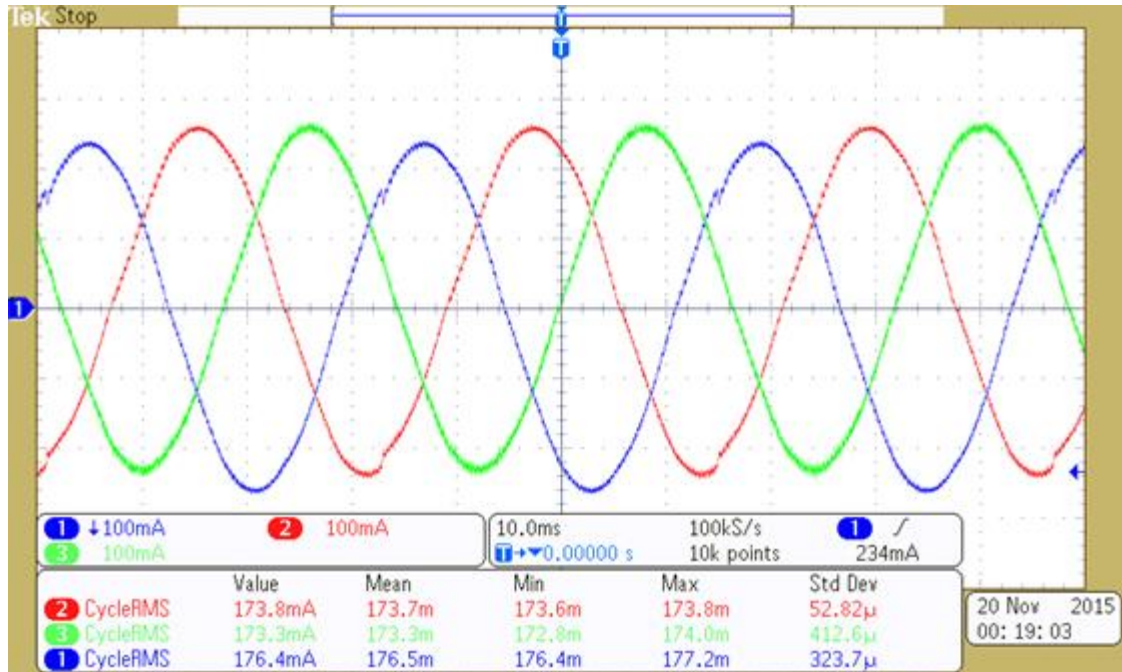


Figure 4.9 3-Phase Current Waveforms after Balancing in Software

The differences in the impedances between phases have been compensated in software to produce the 120° shifted current waveforms shown in Figure 4.9. The pre-tuning waveforms of Figure 4.6 varied in amplitude by up to 24%, but can be seen to now vary by approximately 2% and have been further confirmed experimentally using an ammeter.

The current prior to tuning and compensation of the second stator varied in amplitude by approximately 6.9% and yielded a post-tuning variance of less than 1.1%. As the tuning process offsets lookup table entries specific to each phase based on their resistance and inductance, care must be taken when to ensure the correct phases are connected to the appropriate controller outputs or a de-tuning effect will occur.

Chapter 5 Reaction Plate Design

This chapter describes the design and construction of the continuous loop reaction plate tracks that allow the vehicle maneuver across steel plates. Reaction plate material, segment size and thickness are among the design elements considered and tested.

5.1 Reaction Plate Structure

The reaction plate is the moving member of the vehicle in which eddy currents are induced, generating the thrust. To effectively achieve a reaction plate of infinite length, other experiments [34] have wrapped several layers of thin 0.05mm copper film into a loop around the wheels of the vehicles. For the purpose of robustness and maneuverability, the initial prototype track herein proposed instead consists of several segments of 1.5mm thick aluminum plate, linked together using aluminum rivets and hinge segments.

Equations 2.9, 2.10 and 2.15 together indicate the locked thrust produced by a LIM is not only dependent on the physical construction of the stator, current density through the windings and airgap, but is also dependent on reaction plate equivalent conductivity, width, length and thickness. The equivalent conductivity is determined by the material used for the reaction plate, which was chosen to be aluminium for its light weight, high conductivity and paramagnetic properties, but is further weighted to account for the presence of the steel backing plate, transverse edge effects and skin effects [17]. Figure 5.1 pictures two early prototype track designs with different segment lengths and thicknesses.



Figure 5.1 Early Reaction Plate Prototypes

The prototype tracks in Figure 5.1 illustrate how hinges segments are riveted to the tracks to form a linked track. This early design had problems due to transverse edge effects as the tracks are the exact same width as the stators. Furthermore, the short segment length provided great track maneuverability but proved to prevent sufficient thrust generation over the controller operation region. Future tracks were subsequently chosen to have a width equal to twice that of the stators in order to allow the transverse end effects to be neglected [22].

The spacing between the LIM stator and steel backing plate is required to be sufficiently large so as to allow the aluminum hinges that connect each of the aluminum reaction plate segments together to pass over the stator teeth unobstructed and without catching. The hinge selected has a maximum thickness of 6mm at the section surrounding the pin, suggesting that the minimum spacing between stator and backing plate should be 6mm, allowing aluminum segments totaling up 6mm to be used to comprise the track. The effect of changing the reaction plate thickness was initially simulated using FEM modelling software for a fixed 5A RMS phase current through each winding and constant

7mm spacing between stator and backing plate, within which the reaction plate is free to move, giving the simulation results illustrated in Figure 5.2.

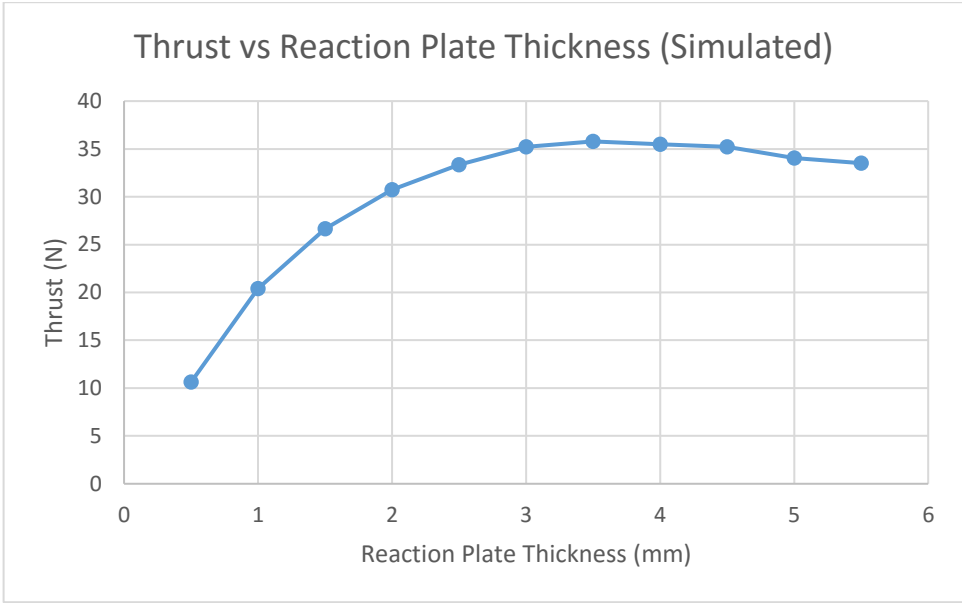


Figure 5.2 Thrust vs Reaction Plate Thickness (Simulated)

Figure 5.2 indicates that greater thrust is produced by the LIM as the ratio of aluminium to air in the gap between the stator and backing plate increases until the gap is approximately half-filled. The shape of the curve suggests the reaction plate to be used for the robotic vehicle should be constructed such that it occupies at least half of the required minimum gap of 6mm between the stators and backing plate in order to increase thrust production. This hypothesis is tested experimentally by measuring the thrust produced for reaction plate segments of equal length and with thicknesses of 1.5mm, 3mm (1.5mm x 2 ply) and 4.5mm (1.5mm x 3 ply) with the same 7mm gap between backing plate and stator as simulated, producing the graph of Figure 5.3. The 3-ply reaction plate construction had a physical thickness of 6mm due to irregularities (bending) when mating the ply together. For the same reason, the 6mm (1.5mm x 4 ply)

construction had an 8mm physical thickness so could not be tested within the 7mm spacing.

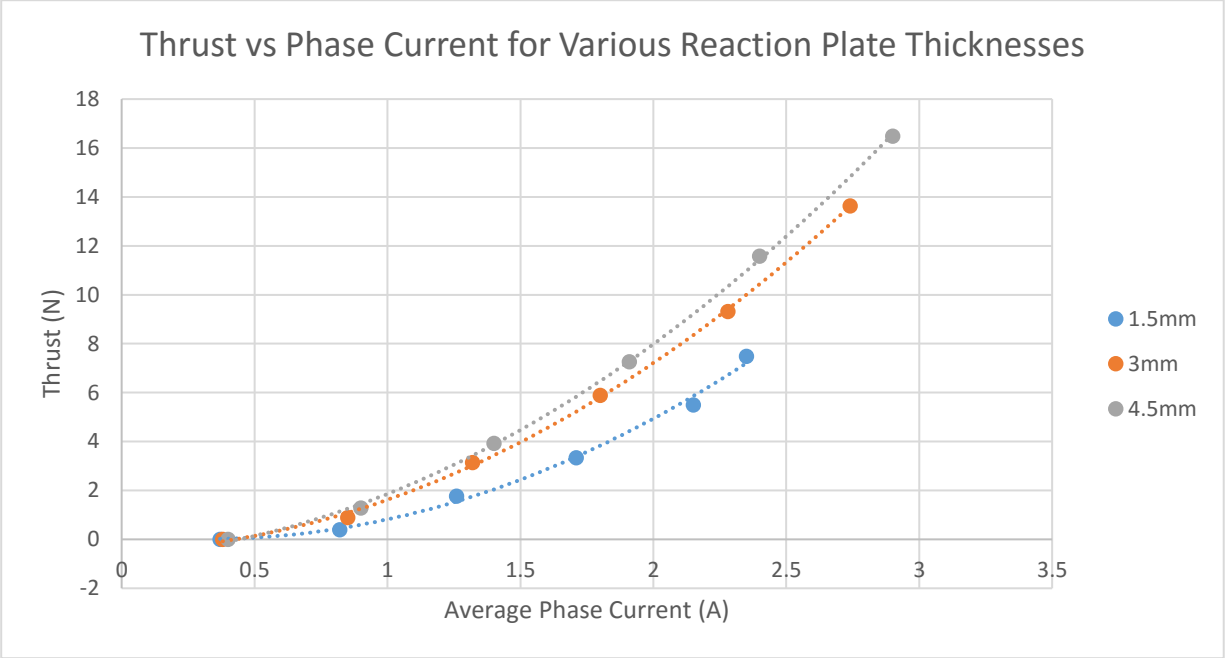


Figure 5.3 Thrust vs Phase Current for Various Reaction Plate Thicknesses

Figure 5.3 verifies that the thrust produced increases significantly for the same phase current when a 3mm thick reaction plate is used instead of a 1.5mm version. Similarly, a 4.5mm thick reaction plate delivers further gains over the 3mm version, but the gain in thrust is not as significant. These results validate those found by simulation in Figure 5.2. The data points in the chart are recorded for applied voltages increased in 10V increments, showing that the magnitude of the phase currents for constant applied voltages also increases with reaction plate thickness.

The final design parameter to be determined was the optimum length of the individual segments. Whilst the segments should be made as short as possible to allow the track to form a loop that fits well around the wheels of the vehicles, each segment

must be sufficiently long to minimize the effects of the reaction plate being shorter than the wavelength of the MMF wave that forms in the gap.

The following figure shows the thrust resulting from placing 1.5mm thick aluminum segments of various lengths at the center of the stator and applying a fixed current at a constant airgap.

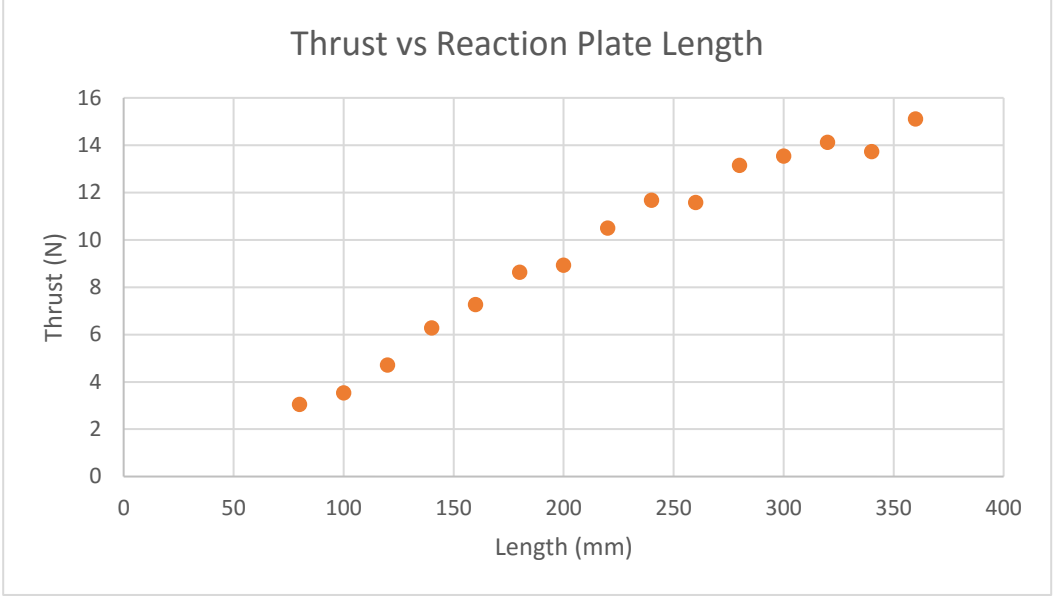


Figure 5.4 Thrust vs Reaction Plate Length

The total thrust generated by the assembled reaction plate segments can hence be calculated by Equation 5.1.

$$F = \frac{l_{stator}}{l_{segment} + l_{hinge}} * F_{segment} \tag{5.1}$$

Using this equation, individual reaction plate segments were selected to have a length of 180mm. This size is short enough to form a neat loop around the wheels of the vehicle, but sufficiently long to minimize the negative effects of a shorter reaction plate. The assembled LIM vehicle with continuous tracks made from 180mm segments is shown in Figure 5.5.

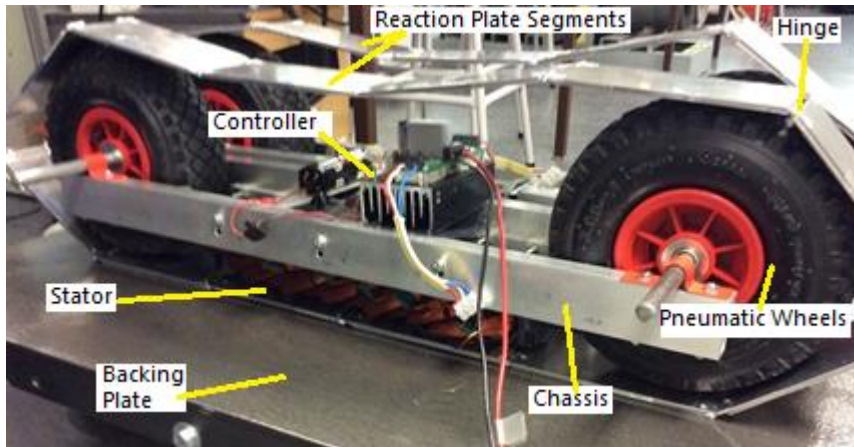


Figure 5.5 Reaction Plates Form a Closed Loop around the LIM Vehicle

The reaction plate design characteristics are summarized in Table 5.1.

Length (m)	0.180
Width (m)	0.090
Thickness (m)	0.006
Aluminum Thickness (m)	0.001.5 x 3 ply
Mass (kg)	0.18
Pieces per Loop	13

Table 5.1 Reaction Plate Segment Dimensions

5.2 Experimental Results

Commercially available variable frequency drives offer various control techniques ranging from basic Volts-per-Hertz control through to sophisticated sensorless vector and torque control methods [32]. For a known load, however, a lookup table-based optimal torque control can be achieved via thorough characterization of the load. This section investigates the relationships between controllable voltage and slip-frequency parameters and developed thrust and normal forces in order to implement such optimal torque control.

An important design consideration is what voltage and frequency should be applied for a given slip-frequency product, so measurements were made of the thrust developed for drive frequencies of 12.5Hz, 25Hz and 50Hz, yielding Figure 5.6.

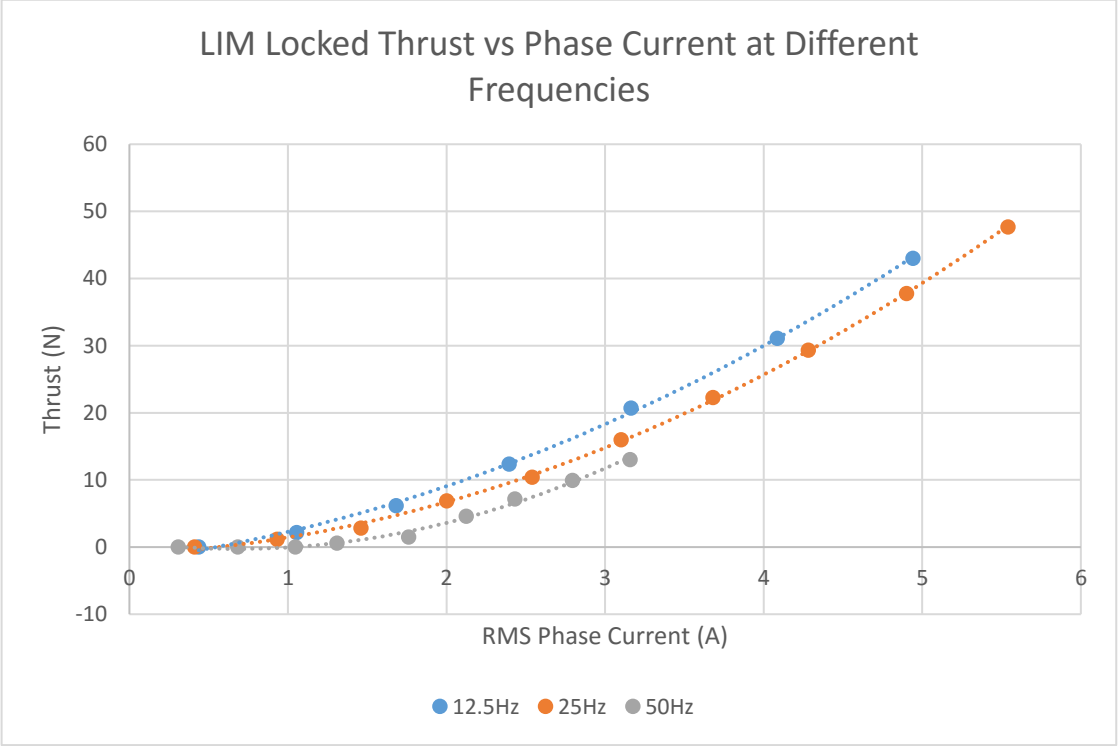


Figure 5.6 LIM Locked Thrust vs Phase Current

Figure 5.6 indicates the thrust developed under locked reaction plate conditions is proportional to the square of the phase current, consisted with Equation 2.15. In addition to the large variation in applied voltage required to achieve the same phase current due to greater impedance at higher frequencies, the thrust developed for a given phase current is shown to have a small but non-negligible frequency dependence.

To verify the frequency dependence of thrust developed, thrust was measured under locked stator conditions with a phase current of 3A while frequency was varied, producing the graph of Figure 5.7.

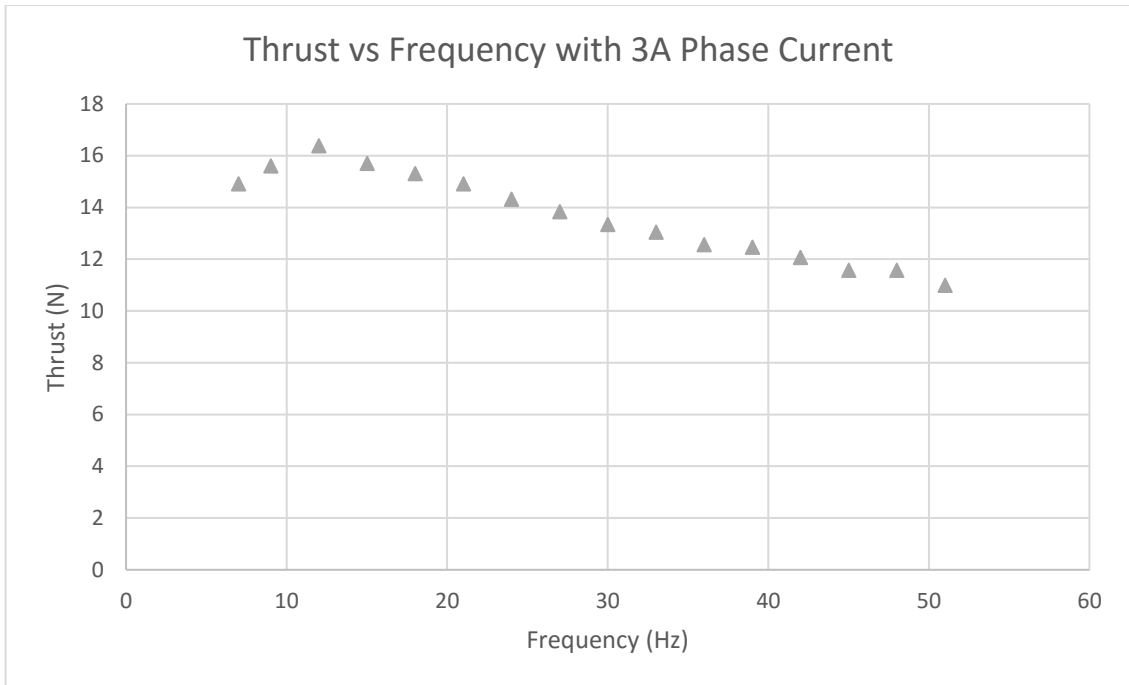


Figure 5.7 Thrust vs Frequency for Fixed Phase Current

If the applied frequency approaches 0Hz, the synchronous velocity also approaches zero so there is no slip for a static reaction plate and consequently no mismatch in rotating magnetic fields to induce the thrust producing eddy currents, so thrust generated is also zero. Moreover, Equation 2.15 suggests that the thrust developed is inversely proportional to the slip-frequency and consequently decreases as frequency is increased. Therefore a non-linear thrust versus torque curve can be expected, with a peak in developed thrust located in the low slip-frequency region. Figure 5.7 experimentally verifies this relationship with peak thrust of over 16N at 12.5Hz.

The power factor of the system is another parameter of interest as it describes the ratio of real power used to do work to the apparent power that is applied to the circuit. An oscilloscope can be used to show the phase difference between voltage and current waveforms, allowing the power factor to be calculated. In this case, the voltage waveform

is the sine-PWM switching waveform applied to stator windings, while the current waveform is sinusoidal as harmonic content is filtered out due to the inductive load, giving the waveforms seen in Figure 5.8. As expected, with no reaction plate in the airgap to generate thrust, the large inductance of the stator relative to the resistance causes the current waveform to lag behind the voltage waveform by approximately 90° .

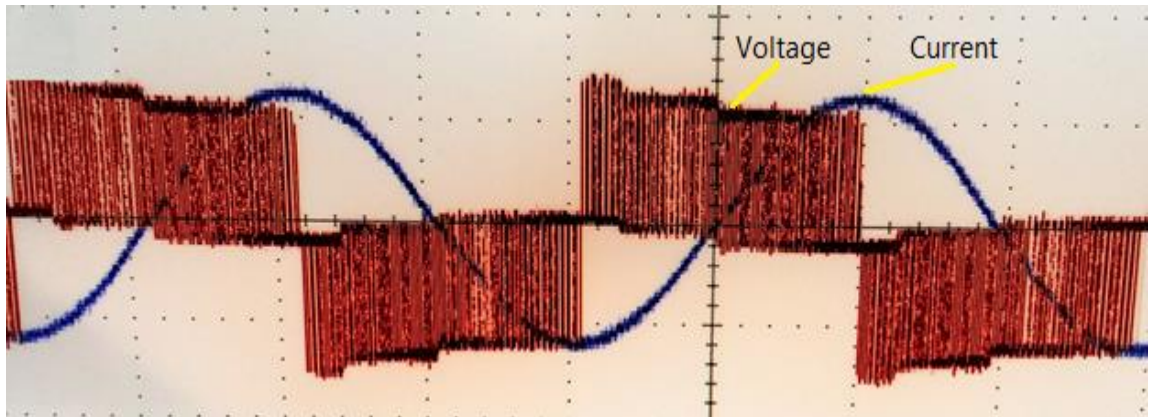


Figure 5.8 Voltage and Current Waveforms Applied to Stators

When a reaction plate is present in the airgap it is helpful to use Equation 2.14 to determine the power factor, which states that the power factor is proportional to the ratio of the thrust developed and the resistive losses to the total power input to the system. Using the experimentally measured data, the power factor for various input powers at 25Hz fundamental drive frequency yields Figure 5.9.

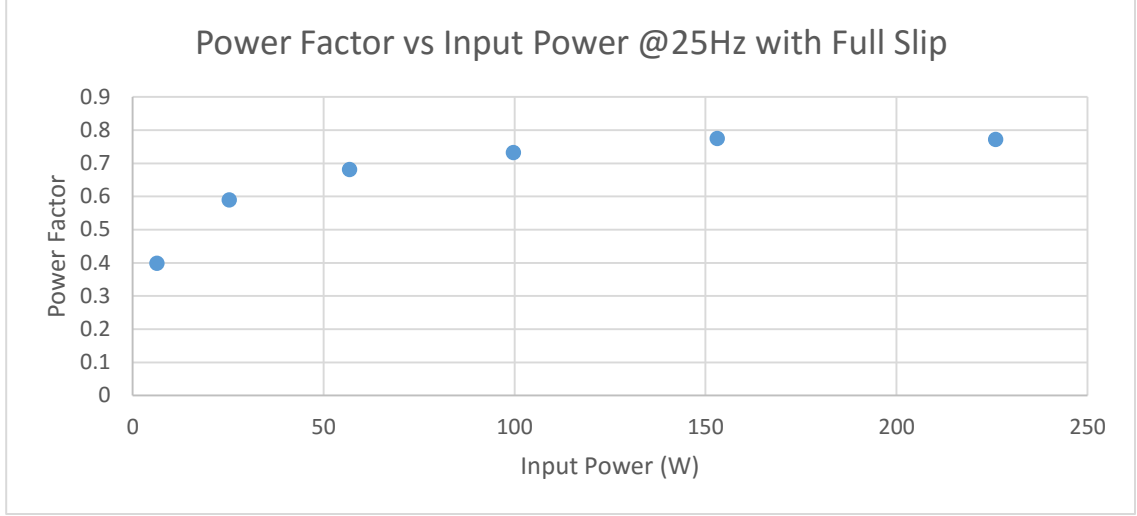


Figure 5.9 Power Factor vs Input Power at Slip=1

Figure 5.9 shows the power factor of the system approaches 0.8 as the applied power is increased for locked rotor conditions.

As the power factor is dependent on the thrust developed via Equation 2.17 and the thrust is dependent on slip via Equation 2.15, the power factor also varies in accordance with slip. Combining Equation 2.15 with Equation 2.17 yields,

$$\cos \varphi = \frac{\frac{3I_1^2 R_2'}{S \left[\left(\frac{1}{SG_e} \right)^2 + 1 \right]} + 3I_1^2 R_1}{3V_1 I_1} \quad (5.2)$$

The Goodness Factor of the system varies slightly due to a changing effective airgap length as given by Equation 2.10. Changes in the effective airgap are small, so the Goodness Factor is specified as slip-independent for simplicity in the following derivation. Then, grouping the terms dependent on slip together in a function $f(s)$, Equation 5.2 can be rewritten as,

$$\cos \varphi = \frac{\frac{3I_1^2 R_2'}{f(s)} + 3I_1^2 R_1}{3V_1 I_1} \text{ where } f(s) = S \left[\left(\frac{1}{SG_e} \right)^2 + 1 \right] \quad (5.3)$$

The power factor for full slip is known from Figure 5.9, but is of interest to calculate the power factor as slip approaches zero. Mathematically, the limit of $f(s)$ approaches infinity as the denominator of $f(s)$ goes to zero, hence,

$$\lim_{s \rightarrow 0} f(s) = \infty \rightarrow \lim_{s \rightarrow 0} \cos \varphi = \frac{3I_1^2 R_1}{3V_{1f} I_1} = \frac{I_1 R_1}{V_{1f}} \quad (5.4)$$

Using ohms law to substitute V_{1f} then yields,

$$\lim_{s \rightarrow 0} \cos \varphi = \frac{I_1 R_1}{I_1 Z_T} = \frac{R_1}{Z_T} \quad (5.5)$$

where Z_T is the total impedance of the per-phase equivalent circuit. Accordingly, the power factor for zero slip conditions is equal to the ratio of the winding resistance to the total circuit impedance. The zero slip condition is identical to the purely inductive load not producing any thrust of Figure 5.8, resulting in a power factor of approximately zero due to the nearly 90° phase difference between voltage and current waveforms as the inductive reactance provides a more substantial contribution to the total circuit impedance compared to the winding resistance.

Equation 5.3 shows the power factor is greatest when the value of $f(s)$ is smallest, allowing the value of slip that yields the greatest power factor to be calculated by differentiating $f(s)$ with respect to slip to find the minimum, giving,

$$\frac{d}{ds} S \left[\left(\frac{1}{sG_e} \right)^2 + 1 \right] = 1 - \frac{1}{s^2 G_e^2} \quad (5.6)$$

Setting the derivative equal to zero and rearranging gives,

$$S = \frac{1}{G_e} \quad (5.7)$$

This suggests that for systems with a Goodness Factor less than 1, the peak slip occurs at a non-realizable value greater than 1, indicating that the power factor decreases

as slip decreases. If the Goodness Factor is greater than 1, the peak power factor occurs for a slip between 0 and 1. This means that the power factor of the system improves to a maximum value determined by the Goodness Factor as slip decreases, before decreasing again as slip approaches zero.

Chapter 6 LIM Vehicle Performance

Models of LIM properties and theoretical performance are subject to the various approximations made by the model and the non-ideal nature of physical constructions. In this chapter, various LIM drive parameters are varied and the resulting fluctuations in forces generated are compared to those simulated or calculated analytically using the equations in Chapter 2.

6.1 Normal Force

The developed attractive force was initially investigated in Chapter 3, leading to Figure 3.8 which shows the relationship between attractive force and phase current in the absence of a reaction plate. However, this relationship is not so simple for the proposed LIM vehicle due to the non-linear effects of the reaction plate track and changes to the airgap during operation. The normal force produced is the vector sum of the attractive force to the backing plate and repulsive force from the reaction plate largely due to the opposing magnetic fields of the induced eddy currents. Therefore, while Figure 3.8 appears to show the magnitude of the normal force is approximately proportional to the square of the phase current, the sign of the force depends on both structural and drive parameters. Equation 2.21 showed the net normal force is attractive when the products of slip, frequency, pole-pitch, thickness and effective conductivity of the reaction plate equate to less than π/μ_0 .

The targeted slip-frequency region at which the LIM vehicle will be operated is that which develops the greatest thrust force, namely a slip-frequency between 10 – 20Hz, as shown in Figure 5.7. Accordingly, the net normal force over this operating region is

also required to satisfy Equation 2.28 to ensure operation at any angle of incline. The locked rotor thrust and normal forces per stator can be calculated using Equations 2.15 and 2.18 for an RMS phase current of 3A and are shown below in Figure 6.1 (cf. Figure 2.9).

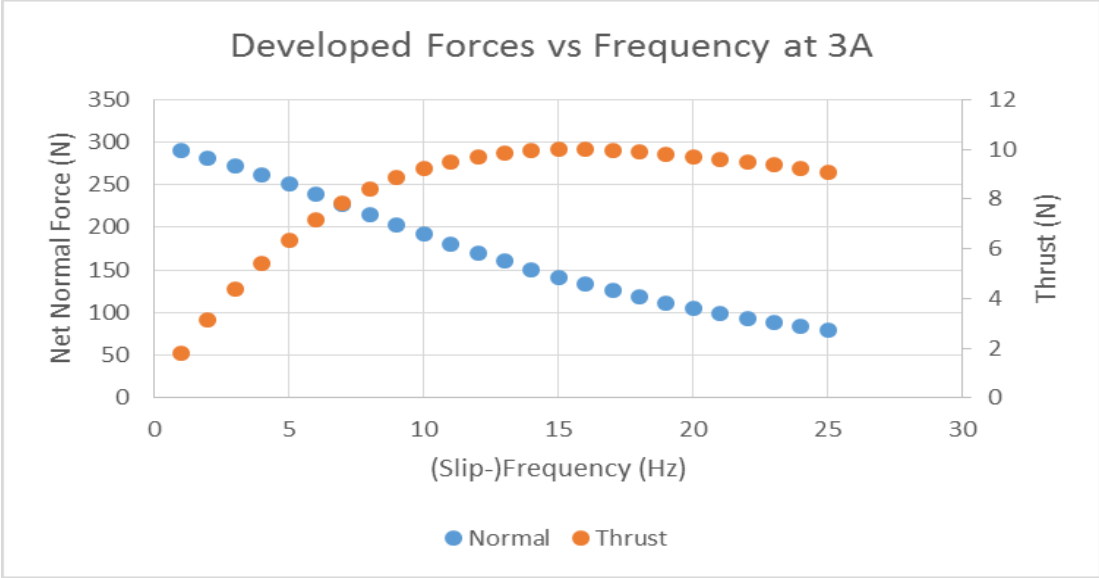


Figure 6.1 Calculated Forces for 3A Phase Current and Full Slip

Figure 6.1 indicates that over the intended operating region the normal force varies by a factor of 2, from approximately 200N at 10Hz down to 100N at 20Hz, while the thrust developed stays relatively constant. This varying normal force could be utilized in a control algorithm to increase the slip-frequency for regular upright and flat vehicle use to limit friction on the vehicle bearings, yet lowering the slip-frequency for inverted/inclined operation to achieve a greater attractive force between the vehicle and backing plate.

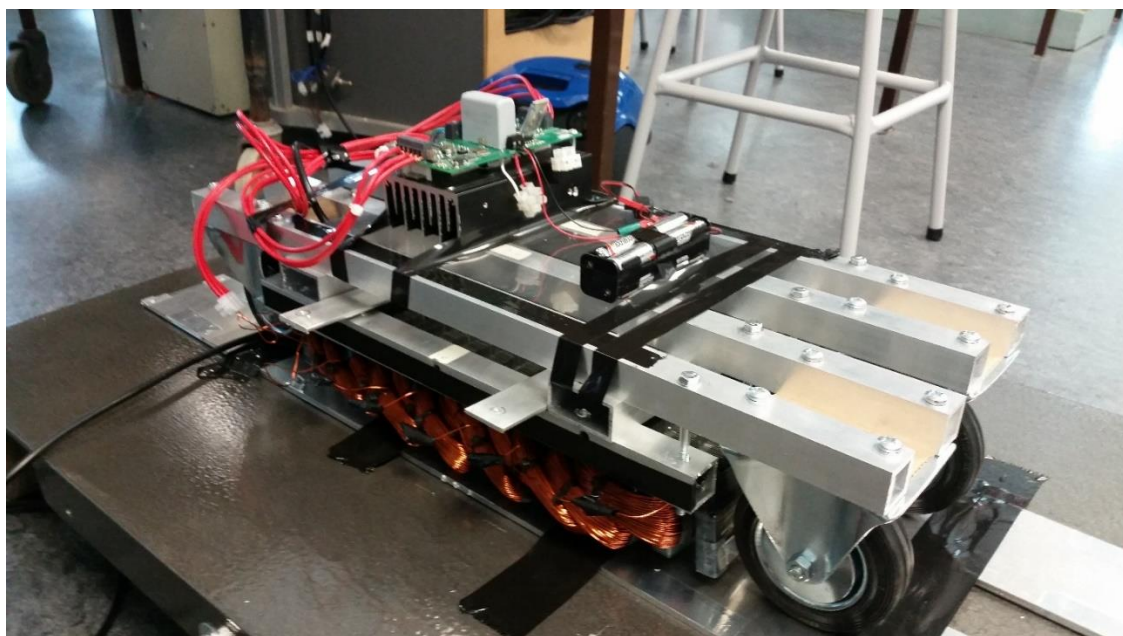


Figure 6.2 LIM Vehicle and Rig for Achieving a Constant Airgap

Figure 6.2 shows the vehicle rig, complete with controller board, resting on the unfolded aluminium track and steel backing plate. The enclosed track is unfolded for experimental ease and has no effect on the results obtained. Castor wheels also replace the pneumatic tyres for the purpose of obtaining results with a fixed airgap length. The vehicle dimensions and mass for the rig using castors is summarized in Table 6.1.

Length (m)	0.61
Stator Width (m)	0.1
Total Width (m)	0.33
Height (m)	0.145
Mass (kg)	24.1

Table 6.1 Modified Vehicle Dimensions

The net normal force produced by the vehicle was measured using electronic scales for various phase currents and frequencies under locked rotor conditions. The vehicle was held in place by heavy blocks and the aluminium reaction plate was fixed to

the backing plate to prevent any linear movement. The experimental setup is sketched in Figure 6.3.

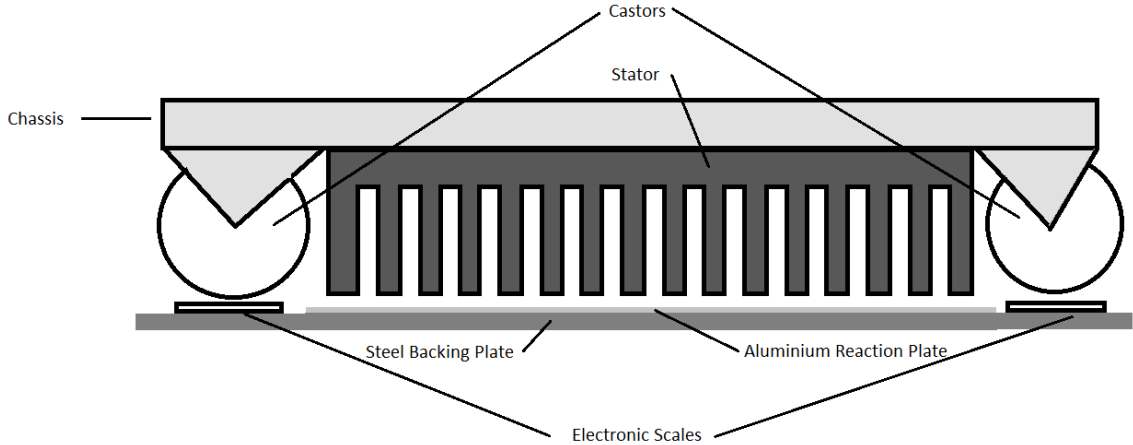


Figure 6.3 Side-on View of Experimental Setup for Measuring Normal Force

For a constant phase current, the net normal force was measured over a range of frequencies, yielding the normal force versus frequency graph of Figure 6.4.

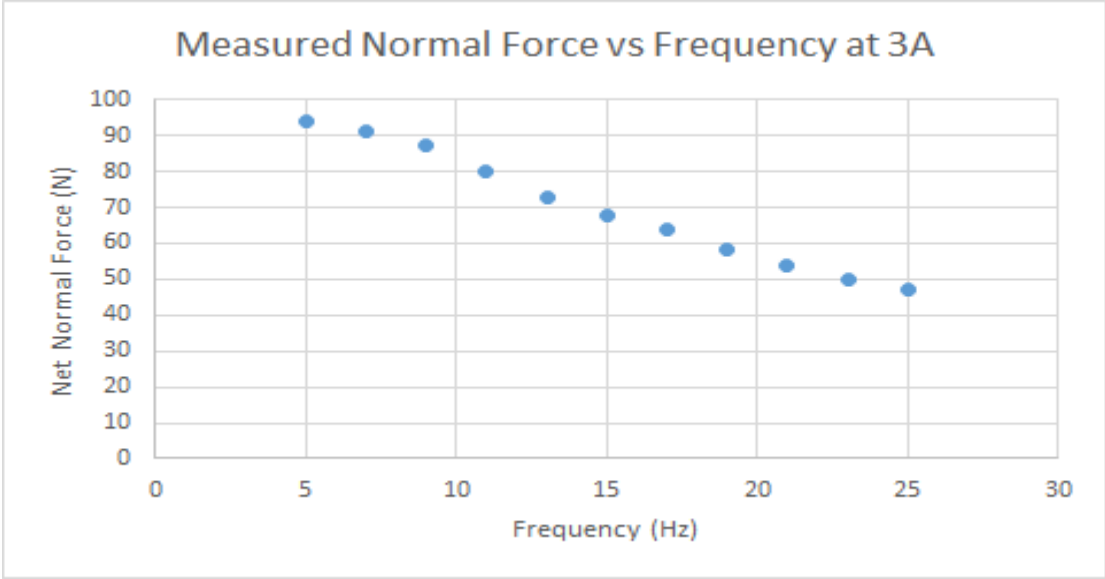


Figure 6.4 Measured Normal Force Versus Frequency at 3A

The positive net normal force values in Figure 6.4 indicate that the net force is attractive, consistent with expected calculated result using Equation 2.21. Furthermore, the graphed data represents the ‘per stator’ normal force developed, allowing the total normal force produced by the vehicle to be calculated by multiplying by a factor of two.

Over the intended operating region of 10 – 20Hz, the net normal force for 3A phase currents ranges from 160N total at 10Hz, down to 110N total at 20Hz. The negative slope of the measured results is less steep than that of the calculated results of Figure 6.3 and the produced force is decreased compared to the calculated results across the range. This can be attributed to core and copper losses that are not factored into the model used for calculations.

As the net normal force produced with phase currents of 3A over the intended operating region is less than the 270N weight of the vehicle and track, the vehicle would be unable to operate upon surfaces with a steep incline or inverted surfaces, regardless of the thrust produced. However, Equation 2.18 suggests the net attractive force produced increases proportional to the square of the phase current density, suggesting that sufficient normal force may be generated if the magnitude of the phase current is increased. Figure 6.5 illustrates the measured attractive force for various RMS phase currents at frequencies of 10Hz, 15Hz and 20Hz.

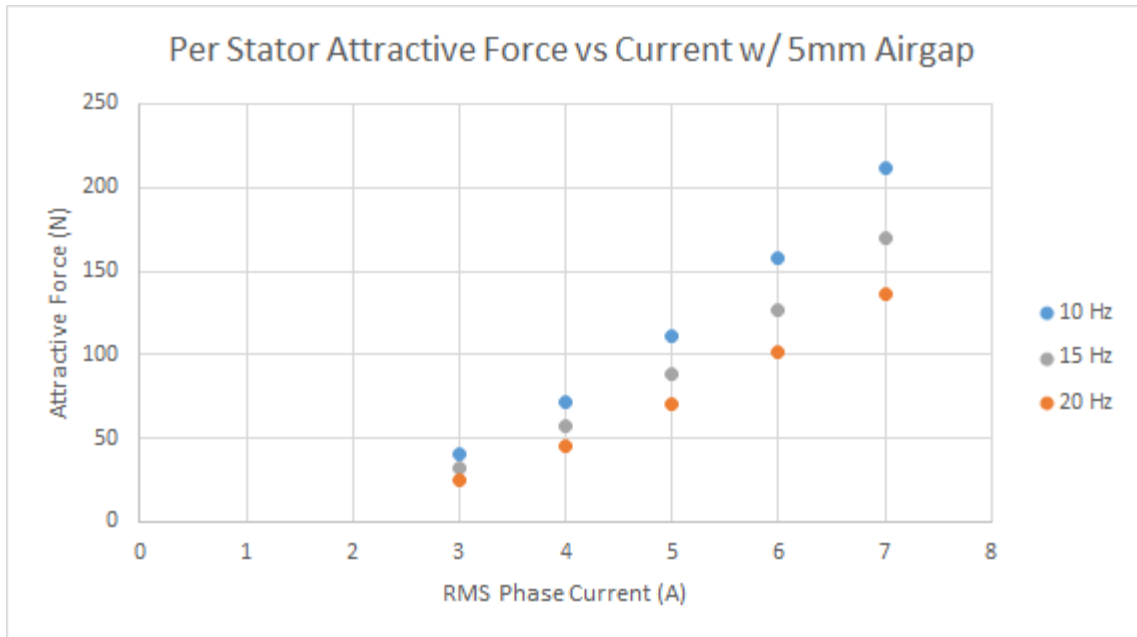


Figure 6.5 Per Stator Attractive Force vs Current for a 5mm Airgap

Equation 2.26 showed the required normal force for inclined operation is greatest when climbing a backing plate at 121° relative to the horizontal and can be calculated to be 518N, or 259N per stator, using Equation 2.28. Figure 6.5 confirms the attractive force produced increases proportional to the square of phase current, with a peak attractive force recorded of 210N for 7A RMS phase current at 10Hz. 210N falls short of the required 259N per stator for operation, ignoring required thrust for such operation, at all angles, but the results can be combined with those from Figure 6.4 to suggest that 259N may be achievable at a 5Hz drive frequency, or alternatively by applying 8A RMS through the windings.

To test upside-down operation, the vehicle was placed in an inverted position under the steel backing plate and driven with a voltage at 10Hz to produce 6A RMS phase current. The vehicle was hereby experimentally confirmed to generate sufficient

attractive force to support its own weight for inverted operation on the bottom side of a steel backing plate.

6.2 Thrust Force

The thrust force must be sufficient to overcome the static friction of the vehicle in order for linear motion to be achieved, with any excess thrust used for acceleration. As the angle of the backing plate for climbing operation increases, so too does the required thrust in order to overcome gravity. The most extreme climbing case possible is that where the vehicle attempts to climb a surface perpendicular to the Earth, such as a wall, in the direction that opposes the gravitational pull of Earth the greatest. Under such conditions, the thrust required to achieve motion is in excess of the vehicle weight plus static/kinetic coefficient considerations. For this vehicle, the goal is hence to produce at least 280N of thrust.

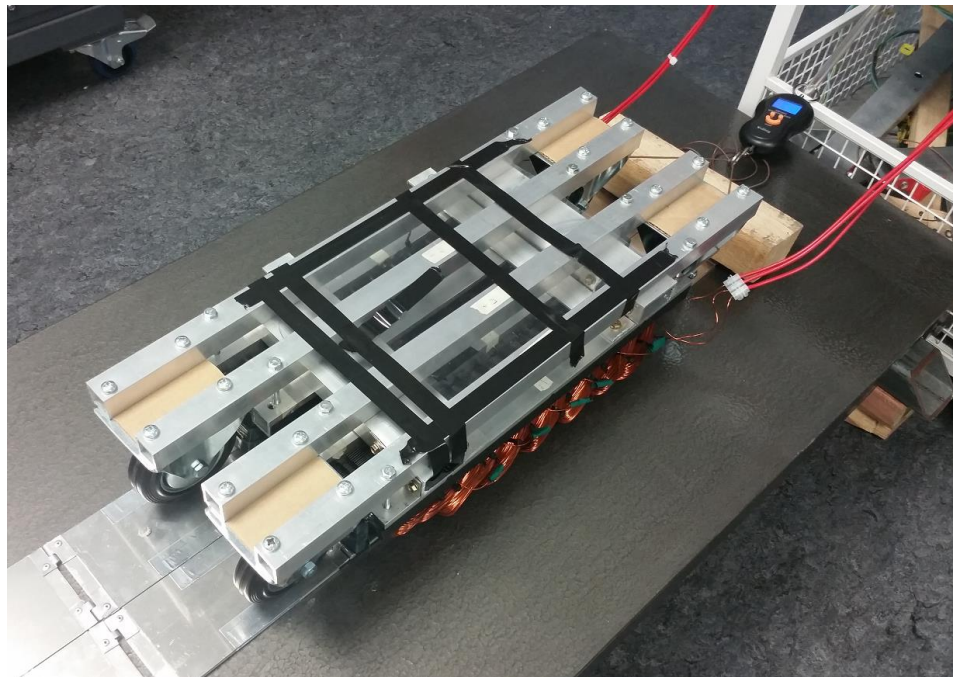


Figure 6.6 Measuring Vehicle Thrust on Steel Backing Plate with Fixed Track

To measure the thrust performance, the reaction plate track was fixed to the steel backing plate arranged horizontally and the vehicle placed atop the reaction plates such that it can roll freely along the length of the track. An electronic force meter was then used to hold the vehicle in place and measure the produced thrust. Figure 6.7 shows the measured thrust when operated at 12.5Hz on a prepared steel plate with 5mm airgap.

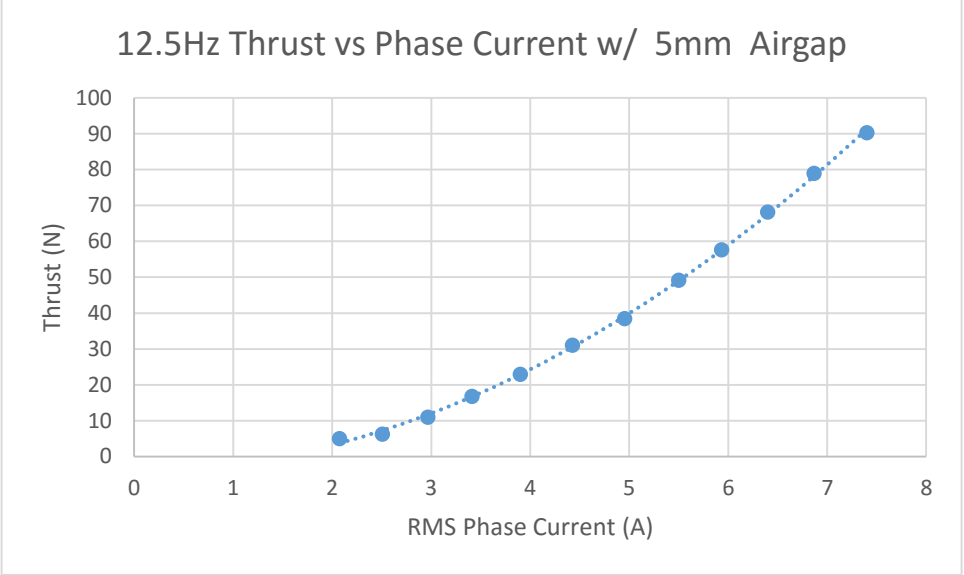


Figure 6.7 12.5Hz Thrust vs Phase Current with 5mm Airgap

With thrust data sampled within the safe operating region of the controller, the next step was to experimentally verify the climbing action of the vehicle up the backing plate positioned at different angles. The steel backing plate used for experimental testing varied the plate angle from horizontal (0° incline) up to a maximum incline of 86° , as shown in Figure 6.8.



Figure 6.8 Maximally Erect Steel Backing Plate (86°)

Starting from 0°, the vehicle was experimentally verified to be capable of climbing angles up to 21°. This was conducted by setting the drive frequency to 12.5Hz and was selected as it produces the peak amount of thrust from standstill (Figure 5.7). The applied voltage was then gradually increased until linear motion occurred.

The attractive force developed was shown to be sufficient to keep the vehicle adhered to the backing plate at any angle and allow various complex driving operations, so long as the track successfully maintains its enclosed loop around the vehicle. In particular, upside-down operation driving along the bottom of a flat surface, or driving across a vertical wall from left to right is possible due to sufficiently large attraction force produced and low levels of thrust required for such motion.

Moreover, the vehicle can also be used to climb vertical surfaces as long as the thrust required does not exceed the maximum thrust available. This can be achieved by controlling the vehicle such that it zig-zags up the wall at angles relative to the horizontal less than that given by,

$$\theta_{max} < \sin^{-1} \frac{F_{x,max}}{mg} \quad (6.1)$$

6.3 Simulated Performance

Various parameters of the LIM vehicle and its performance have been experimentally measured as outlined in the previous chapters, with results compared to those analytically calculated or simulated using FEM software. All of these measured results have been conducted at full slip ($S = 1$) due to the complexities of measuring thrust and normal forces while the vehicle is moving. Moreover, limitations in the controller and power supplies available at the experiment site has prevented operation at high current. This section using FEM software to extend the results discussed thus far, through simulation of the vehicle performance.

As mentioned previously, the vehicle parameter of most interest is the capacity for the vehicle to develop thrust, followed closed by the net normal force produced. In

Figure 6.9, FEM software was used to simulate a range of phase currents for a fixed drive frequency of 12.5Hz and measure the thrust and normal force developed by the LIM vehicle (per stator), extending the experimental measurements from Figure 6.5 and Figure 6.7.

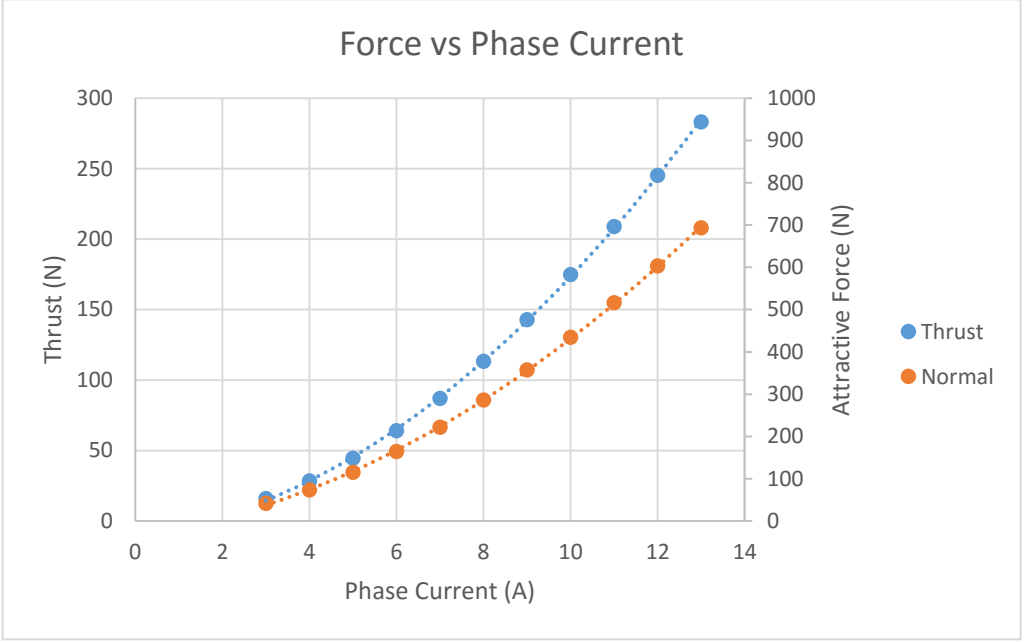


Figure 6.9 Thrust and Normal Force vs Phase Current

Figure 6.9 suggests that the per-stator thrust developed will reach 140N, the required minimum peak thrust for vertical climbing, at a current of approximately 9A. At this current, the attractive force per stator is 357N, translating to 714N for the overall vehicle. As this force exceeds that required for climbing at all angles, as expressed in Equation 6.7, the vehicle is expected to be capable of climbing steel plates at any possible angle for phase currents greater than 9A.

The thrust force produced between the stator and reaction plates for different reaction plate velocities at a 10Hz drive frequency was simulated using FEM simulation

software and is shown in Figure 6.10. Equation 2.4 can be used to calculate the synchronous velocity at this frequency as 1.6m/s.

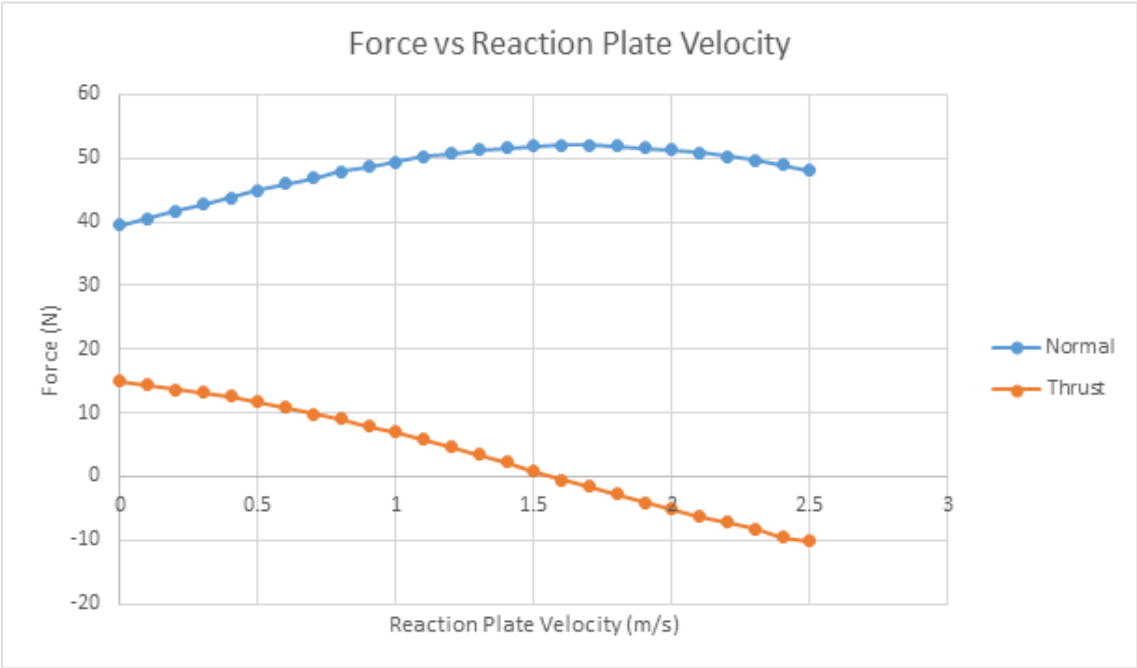


Figure 6.10 Force Developed by One Stator versus Reaction Plate Velocity

As described in Chapter 2, the thrust force is expected to approach zero as the reaction plate velocity approaches the synchronous velocity. Furthermore, for velocities in excess of the synchronous velocity, the slip will become negative and the vehicle will enter “braking” (or “generating”) mode, producing negative thrust in accordance with Equation 2.15. Moreover, Equation 2.18 suggests that the net normal force is greatest (most attractive) when slip is zero. Figure 6.10 validates these hypotheses as the peak normal for can be seen to occur at the synchronous velocity of 1.6m/s, after which the thrust produced becomes negative, indicating deceleration or braking.

Equation 2.15 also indicates the produced thrust is proportional to the square of the phase current and this was confirmed in Figure 6.9. As the inductive impedance

increases linearly with drive frequency, it is of interest to note the relationship between thrust and frequency when the voltage is kept constant, allowing current to vary in accordance with the impedance at each frequency, as per Equation 4.4. Figure 6.11 shows the expected achievable thrust and normal forces as a function of drive frequency for a constant applied voltage.

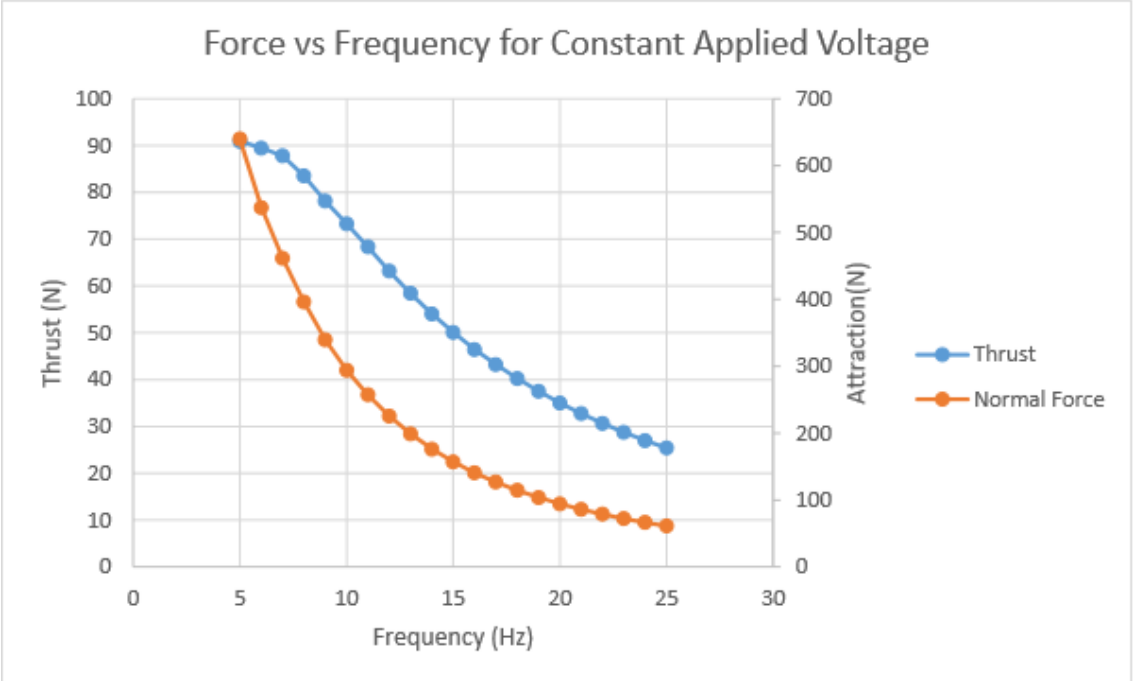


Figure 6.11 Force versus Frequency for a Constant Applied Voltage

Figure 6.11 indicates that the thrust and normal forces are both greatest at low frequency due to the higher current that flows as a result of low impedance.

To keep the flux linkage constant, a simple Volts-per-Hertz algorithm can be used in which the phase voltage applied is increased linearly with applied frequency. For example, the voltage applied when driving the LIM at 20Hz will be twice that applied when driving the LIM at 10Hz as the inductive impedance is twice as large. This simple drive technique ignores winding resistance so the actual current at increased frequencies

rises more rapidly than a true linear relationship. The thrust and normal forces produced using Volts-per-Hertz control are shown in Figure 6.12.

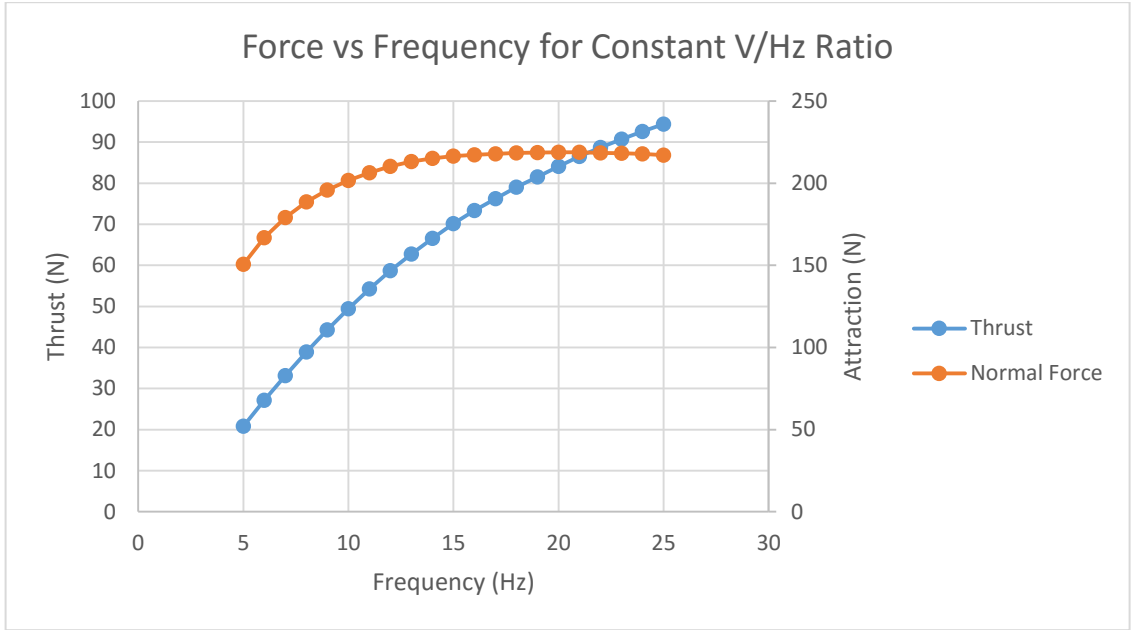


Figure 6.12 Force vs Frequency for Constant V/Hz Ratio

The Volts-per-Hertz control technique of Figure 6.12 results in a characteristic thrust of a similar shape to that found in Figure 6.1 when phase current was kept constant, providing nearly constant thrust over the 10 - 20Hz operating range. However, the net normal force takes on a much different shape, with minimal attraction at low frequencies, increasing as the frequency is raised. The major differences between the results of Figure 6.11 and Figure 6.12 are caused by the changing current. Figure 6.13 depicts the phase current flowing in the windings as a function of drive frequency under constant applied voltage conditions and for when using Volts-per-Hertz control.

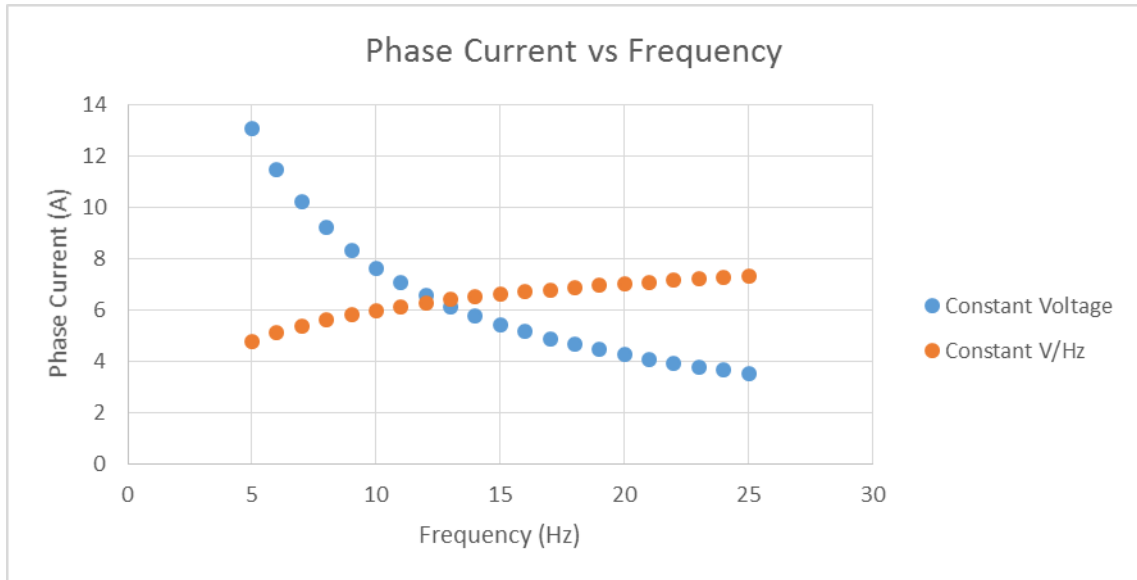


Figure 6.13 Simulated Current vs Frequency using Constant V or V/Hz Techniques

A rapid decline in current as frequency increases for the constant voltage control technique is evident in Figure 6.13, contrasting the increase in current with frequency for the constant Volts-per-Hertz technique due to the ignored winding resistance. For a known load, this winding resistance can easily be accounted for in the control algorithm to produce a constant phase current independent of frequency by including the winding resistance when calculating impedance. If included, the shape of the thrust versus frequency curve becomes identical to that of Figure 6.1 and varies purely as a result of the changing slip-frequency.

FEM analysis is used in Figure 6.14 to show the z-component of the magnetic field along a line down the center of the stator in the middle of the airgap.

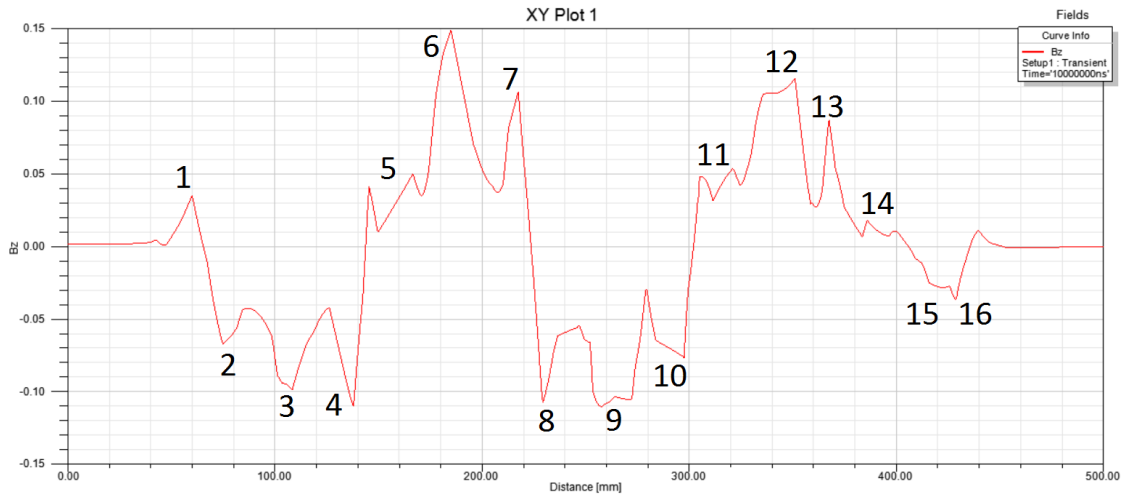


Figure 6.14 Z-Component of Magnetic Field along Stator Length

Figure 6.14 illustrates how the magnetic field taken on a quasi-sinusoidal form along the length of the stator, with magnetic field strength greatest in the vicinity of each of the stator teeth. The overall shape and number of wavelengths present validates the numerical approach taken in Chapter 4 which led to the rectilinear MMF sinusoids of Figure 3.4.

Similarly, the magnitude of the magnetic field can be plotted for a 2D cross-section of the stator to allowing the locations of greatest flux density to be easily observed, as shown in Figure 6.15.

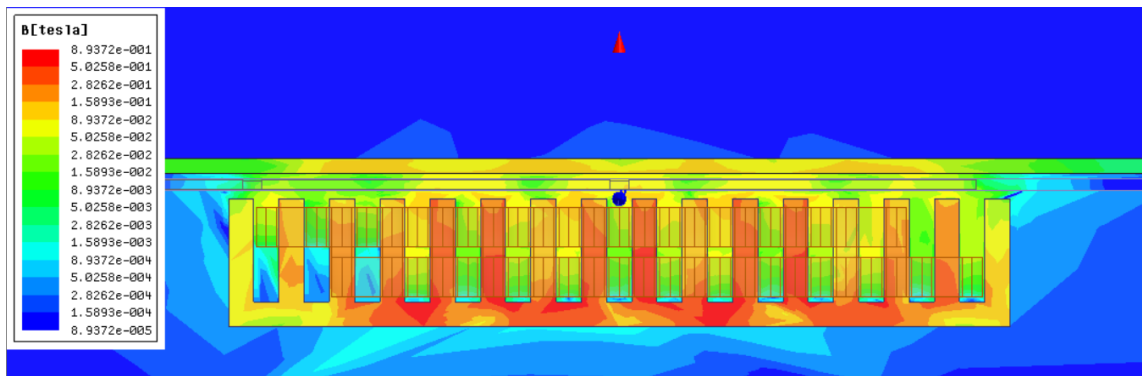


Figure 6.15 2D Snapshot of Magnetic Field Strength in Stator

Figure 6.15 uses a logarithmic scale to make it clear that very little flux escapes the back of the stator and that the flux density is greatest in the teeth of the stators. The visible flux density in the backing plate shows that the flux lines are indeed crossing the airgap, but the decreased density suggests a notable portion is being lost due to flux leakage.

A mechanism showing how a repulsive thrust force can be generated by placing a non-ferromagnetic conductive material in the gap above the stator teeth, causing eddy currents and consequently a repulsive force to be generated by the changing magnetic field in the gap was presented in Chapter 2. Figure 6.16 shows a snapshot in time of the eddy currents produced.

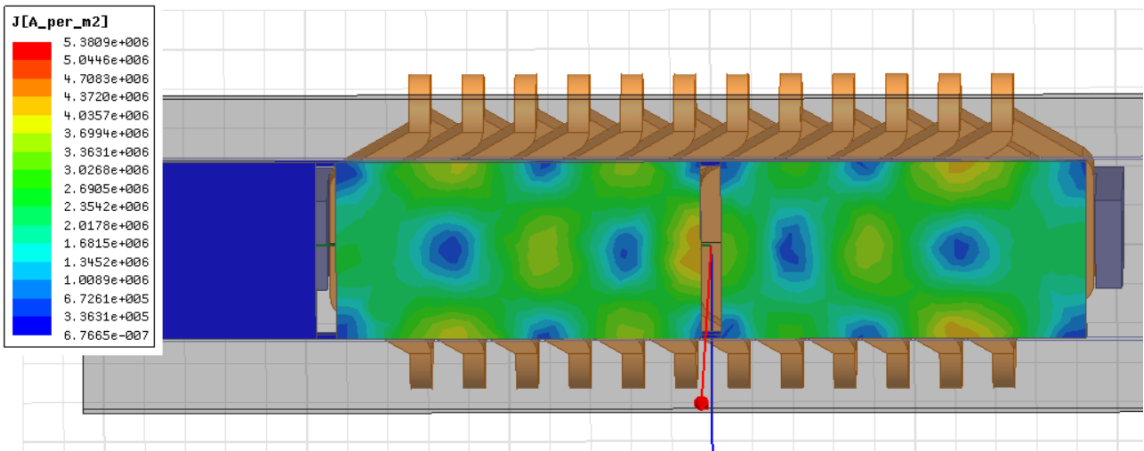


Figure 6.16 Magnitude of Eddy Currents Flowing in the Reaction Plate

Figure 6.16 shows four centers of decreased current density along the length of the two reaction plate segments covering the stator. These centers are the eyes of the eddy current flows, which travel in clockwise and anti-clockwise directions, with direction at any given in point in time alternating in space (clockwise – anti-clockwise – clockwise – anti-clockwise). The eddy current centers propagate along the length of the stator in

synchrony with the travelling MMF wave. The simulation of Figure 6.16 indicates the eddy currents produced for the applied 5A RMS phase currents have a magnitude of roughly $3 \times 10^8 \text{ A/m}^2$, equating to 3 A/mm^2 . The eddy currents produced under non-locked rotor conditions decrease with reaction plate speed, approaching zero as the reaction plate reaches synchronous speed. At synchronous speed, the plate is moving along a ‘wave’ of equal magnetic potential as it crosses the stator and from the perspective of the reaction plate there is no changing magnetic field so no eddy currents are induced.

The simulated eddy current flows can also be used to provide a rough estimate of induction heating that occurs when the stator is in the locked rotor condition. As visible in Figure 6.17, most of the heat-producing current flows circularly around a central eye of low current density within radii r and R from the center.

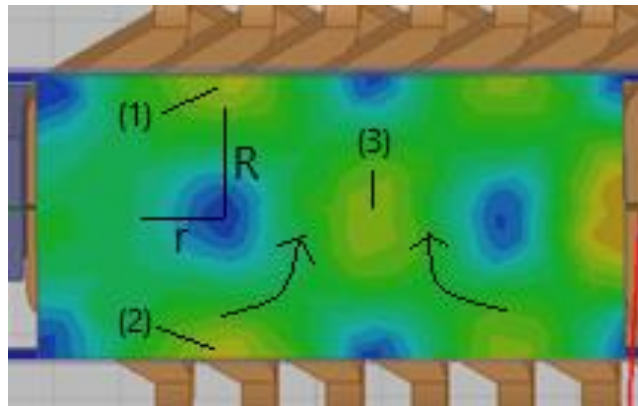


Figure 6.17 Measuring Joule Heating of Reaction Plate

The Lorentz Force equation dictates that a charge in a magnetic field experience a force given by,

$$\mathbf{F} = q\mathbf{v} \times \mathbf{B} \quad (6.2)$$

If the airgap between the stator teeth and backing plate is small then the magnetic field lines between the airgap are close to parallel and Equation 6.2 suggests the electrons

of the reaction plate experience a centripetal force that cause them to accelerate to follow a circular path. Electrons unable to flow in a circular manner due to insufficient electron length cause an increased current density as indicated by markers (1) and (2) in Figure 6.19. The current density is also increased in areas such as that marked by (3), where the electron pathways from different ‘eyes’ overlaps.

The joule heating, P_J , due to the reaction plate current density, J_R , between radii r and R of Figure 6.17, can be calculated using,

$$P_J = I^2 R_2 = \frac{I^2 \rho L}{A} = J_R^2 \rho LA \quad (6.3)$$

where ρ is the resistivity of aluminium, L is the average circumferential length traveled by electrons given by,

$$L = 2\pi(R + r) \quad (6.4)$$

and A is the cross-sectional area of the current loop in a reaction plate of thickness d , given by,

$$A = (R - r)d \quad (6.5)$$

Table 6.2 lists the values used for calculating the reaction plate Joule heating using Equations 6.3 – 6.5.

Current Density, J_R	$3 \times 10^8 \text{A/m}^2$
Resistivity of Aluminium, ρ	$2.65 \times 10^{-8} \Omega\text{m}$
Outer Radius, R	0.04m
Inner Radius, r	0.025m
Reaction Plate Thickness, d	0.004m
Reaction Plate Mass	0.18kg
Specific Heat of Aluminium	$0.902 \text{J/g}^\circ\text{C}$

Table 6.2 Values Used to Calculate Reaction Plate Joule Heating

For the 5A RMS phase current used for the simulation of Figure 6.18, Equations 6.3 – 6.5 can be used to estimate that for locked rotor conditions, 11W of power is used to heat the reaction plate track. For the two circulating currents in Figure 6.19, a track segment with a mass of 180g, and a specific heat capacity of 0.902J/g°C for aluminium, this equates to heating of the reaction plate at a rate of 8°C per minute.

Chapter 7 Future Work

This chapter describes the improvements to be made to the vehicle in its current state in order to enhance the viability for LIMs to be used to in the creation of a vehicle for propulsion along steel plates. Section 7.1 outlines improvements that can be made to vehicle chassis, wheels and track to aid skid-steer turning. Section 7.2 discusses a potential Volts-per-Hertz control algorithm with proportional-integral-derivative (PID) feedback.

7.1 Chassis/Track Design

The chassis design for each stator used for testing purposes thus far consists of the stator itself, two castors at the front and rear of the stator and an aluminum frame holding the relevant components in place. This chassis rolls over each aluminium reaction plate segment during operation, but crucially does not have a mechanism to keep itself aligned above the track. This section proposes a new future chassis and track design to improve the maneuverability of the vehicle while keeping the track properly aligned over the stator.



Figure 7.1 Close-up of Chassis Design using Castors

The proposed track design has an overall shorter vehicle length by moving the wheel axle to be aligned with the stator end. Furthermore, grooves are added to the reaction plate track in which two disc shaped wheels ride, lining up segments as they reach the vehicle front and preventing the track from slipping from the vehicle when turning.

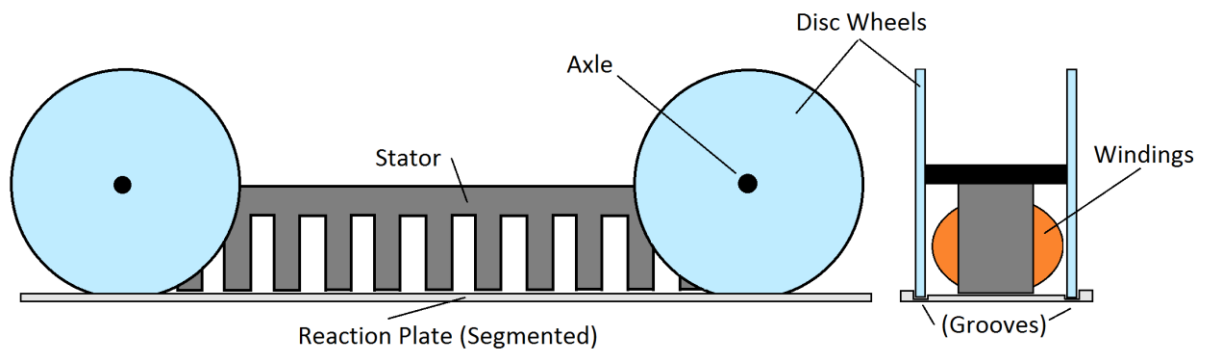


Figure 7.2 Proposed Future Chassis and Track Design

The disc wheels could be made of a rigid, lightweight material such as acrylic, wood or steel wrapped in a layer of rubber or other gripping material to prevent sliding when stalled on steep inclines. The overall vehicle configuration consisting of 4 wheels per stator, or 8 wheels for the entire vehicle, acts to distribute the vehicle weight across the wheels.

7.2 Control Algorithm

Robotic vehicles require a means of interfacing with the user in order to receive information on the task to be completed. Furthermore, the robot needs a feedback and control algorithm to translate the required operations into individual operations within the robot's subsystem.

For the purposes of this project, a bespoke app is used to send various instructions to the robotic vehicle via a Bluetooth link. These instructions can be used to set the frequency and drive voltage (as a percentage of the input voltage) of each stator, turn each stator on or off and also reverse the directions of either stator.

The app is sufficient to manipulate the vehicle for testing purposes; however, this section proposes ways to use the on-board sensors and other information to control the vehicle subject to some constraint or target objective. These sensors were disabled for testing purposes while collecting experimental data.

The on-board sensors available are the accelerometer/gyroscope, temperature sensors and current sensors. The accelerometer/gyroscope can be used to sense the orientation and instantaneous acceleration of the vehicle while the current sensors detect the current through each stator. Temperature sensors are available not only on the board

itself, but are also built into the IGBT modules that switch the stator currents. Additionally, the expansion pinout also allows further resistive element temperature sensors to be connected, for example, for measuring the coil temperature of each stator.

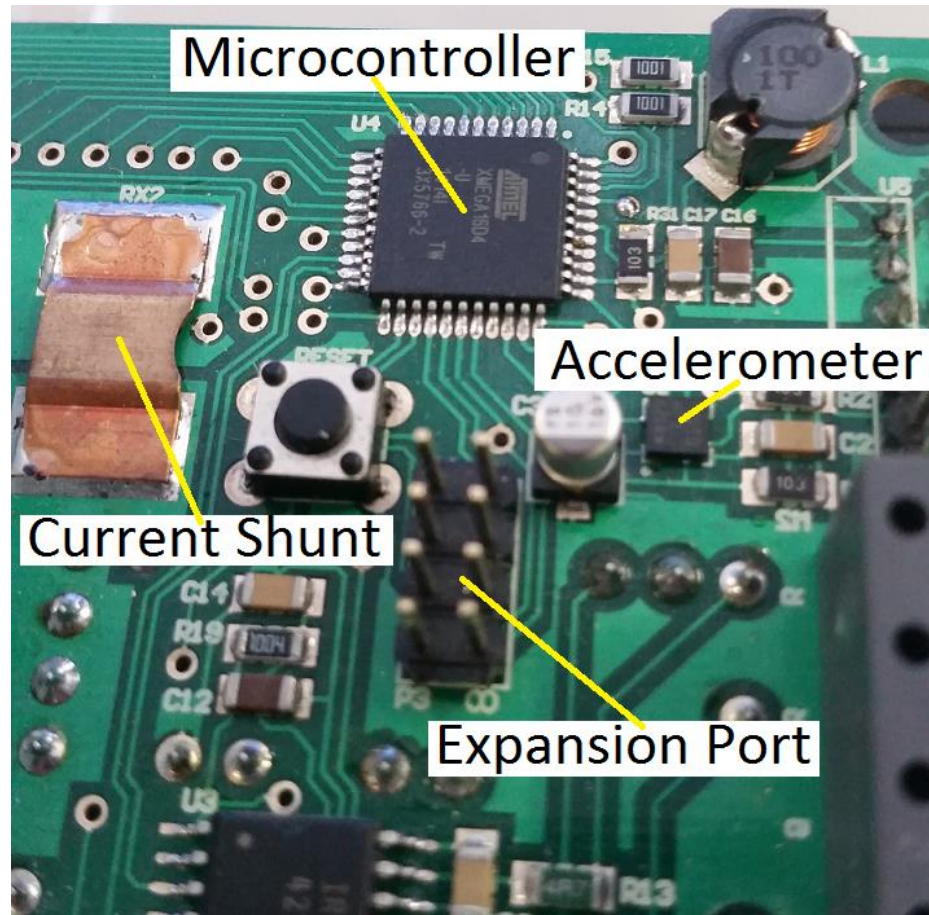


Figure 7.3 Microcontroller, Sensors and Expansion Port Interface

An external linear encoder can also be connected using the expansion headers to allow the distance traveled to be measured and can also be used for velocity/acceleration calculations. Alternatively, optical encoders could be attached to measure the rotation of the wheels for the same purpose.

The proposed algorithm for basic vehicle motion control is essentially a Volts-per-Hertz and optimal torque tracking control hybrid with PID. That is, a slip-frequency

will be targeted based on the desired ratio between thrust and normal forces produced. The frequency is manipulated based on the measured slip in order to keep slip-frequency constant. As per Volts-per-Hertz control, this requires the applied voltage to also be changed to keep the voltage to frequency ratio equal in order to maintain the same flux density in the airgap. Finally PID feedback is used to modify the Volts-per-Hertz multiplier to increase or decrease power to the system.

An outline of this process is presented in the flowchart of Figure 7.4.

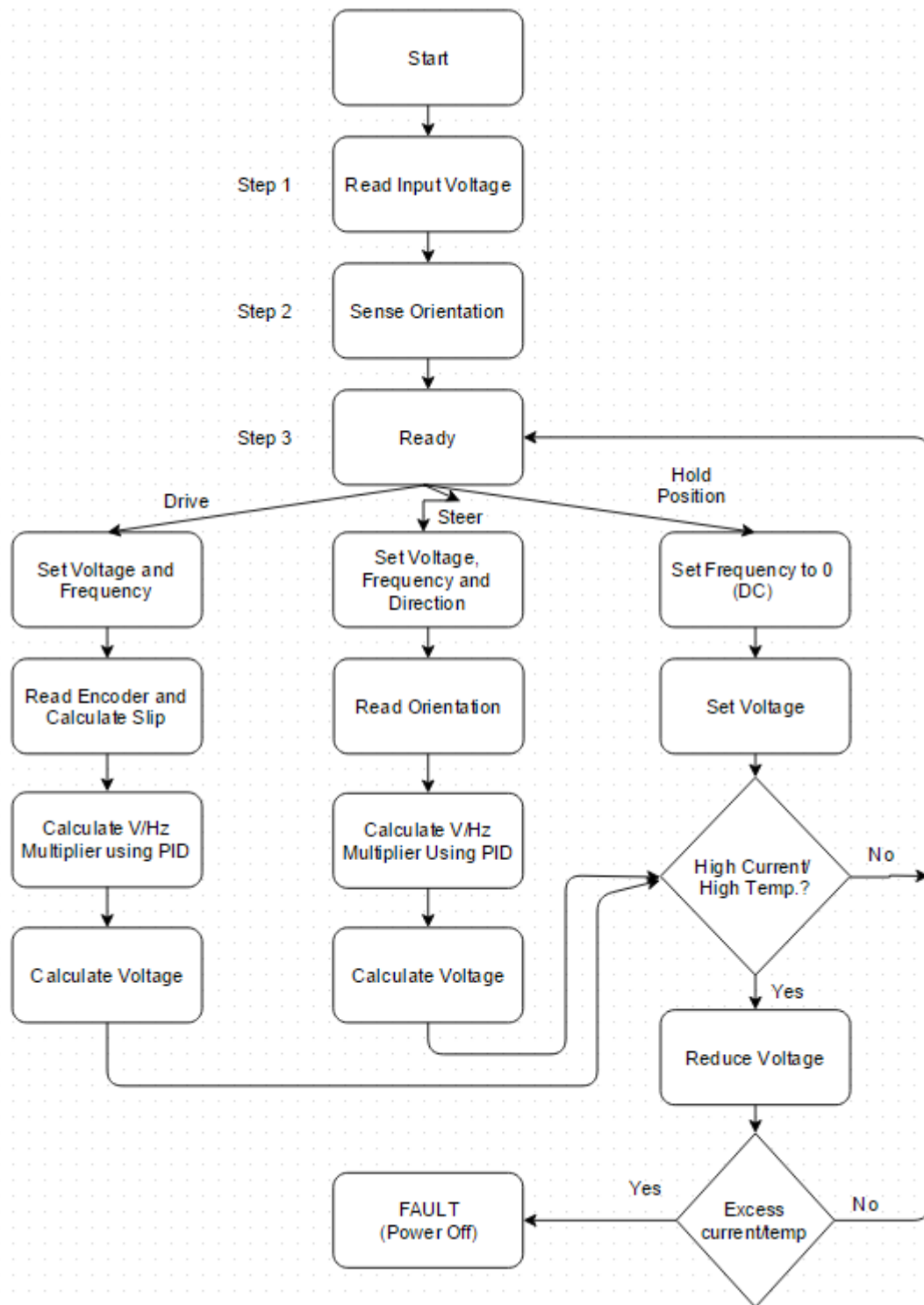


Figure 7.4 LIM Vehicle Control Sequence

Step 1 of Figure 7.5 reads the input voltage to the system using a voltage divider and microcontroller ADC. The initial Volts-per-Hertz ratio can be then calculated by dividing the input voltage by maximum intended operating frequency (20Hz). Step 2 reads the vehicle orientation – upright, sideways (on a wall) or upside-down. The targeted slip-frequency can then be chosen based on the desired attraction force to thrust ratio (Figure 6.4). Step 3 splits the logical pathway into 3 directions depending on whether the vehicle should drive, steer or hold position.

In drive mode, the vehicle receives a position target and initial voltage and frequency, based on steps 2 and 3, are applied to the stators. The encoder is read to calculate the distance moved and the speed of the vehicle. The motor slip can then be calculated from the speed. A PID controller constantly compares the vehicles current position with the target position and modifies the Volts-per-Hertz ratio based on the error. Given the Volts-per-Hertz ratio, the new voltage and frequency to be applied can be calculated from the frequency required to keep the slip-frequency product constant. These new values are applied in the subsequent iteration.

The algorithm for steering mode is similar to drive mode, but the direction of one of the stators can be reversed if required, in order to achieve the desired turning radius. Due to the slippage of the track while turning, optical encoders are not used to prove the orientation feedback. Instead, the on-board orientation sensor (gyroscope) is used for this purpose.

In hold position mode, one output of the 3-phase bridge is set high, while the other two are set LOW. This allows the stator to act as a DC electromagnet, effectively holding its position on the steel backing plate without moving linearly. The phase of the bridge

leg that is set high carries twice the current of the other two phases, so the high and low phases can be interchanged over time to distribute the load.

The temperature of various components and phase currents are checked during each iteration to verify they are within the rated operating range. If they are not, the voltage is lowered for the following iterations, decreasing phase currents and flux linkage. The algorithm can then continue unless the hard temperature/current limit is reached.

The hard temperature/current limit is the maximum allowable component temperature or allowable current (short-circuit detection). If exceeded, the voltage to the stators is rapidly lowered to zero. This fault mode will also cause the vehicle to fall from inclined and inverted surfaces so is implemented as a worst-case scenario fault handling method.

7.3 Other Recommendations for Further Development

It was originally the intent to have the vehicle operate over surfaces of any angle, including inverted, but excessive weight and problems with maintaining a consistent airgap limited the inclines that could be experimentally validated. With this in mind, emphasis on any future such vehicle should be placed on weight reduction. Several methods for reducing the weight are available, including:

- 1) Reducing the winding throw to 1 slot pitch to reduce copper weight of windings
- 2) Further reduce the steel to slot ratio of the stator by stamping out custom laminations

- 3) Replace the aluminium chassis and heavy castors or pneumatic tyres with the disc like wheels from Chapter 6

The avenues of possible research are greatly extended should a large steel backing plate become available. A larger backing plate would give the space required to investigate the skid-steer turning mechanism, as well as allow the electrical parameters of the LIM vehicle to be characters for slips less than 1.

The range of motion available to such a vehicle could be greatly extended if the continuous track system was abandoned in favor of 4 swivel casters at the corners of the vehicle. Such a vehicle would require an aluminium-clad steel backing plate, but would mitigate the effects of friction when turning, resulting in a remarkably maneuverable wall-climbing robot.

Chapter 8 Conclusion

This body of work entailed the simulation, design and build of a vehicle for climbing on steel plates. This included the constructing of two LIM stators, designing and assembling the controller board, investigating and building a reaction plate track structure, creating the vehicle chassis, developing a mobile interface app and programming the microcontroller logic. The physical rig constructed enabled theoretical knowledge and results to be built upon and tested experimentally and the collected data compared to theory, analytical calculations and simulations. These results enabled a control algorithm to be proposed to automate output voltage and frequency selection to achieve drive objectives, incorporating a mechanism for compensating phase current magnitudes due to imbalanced phase impedances.

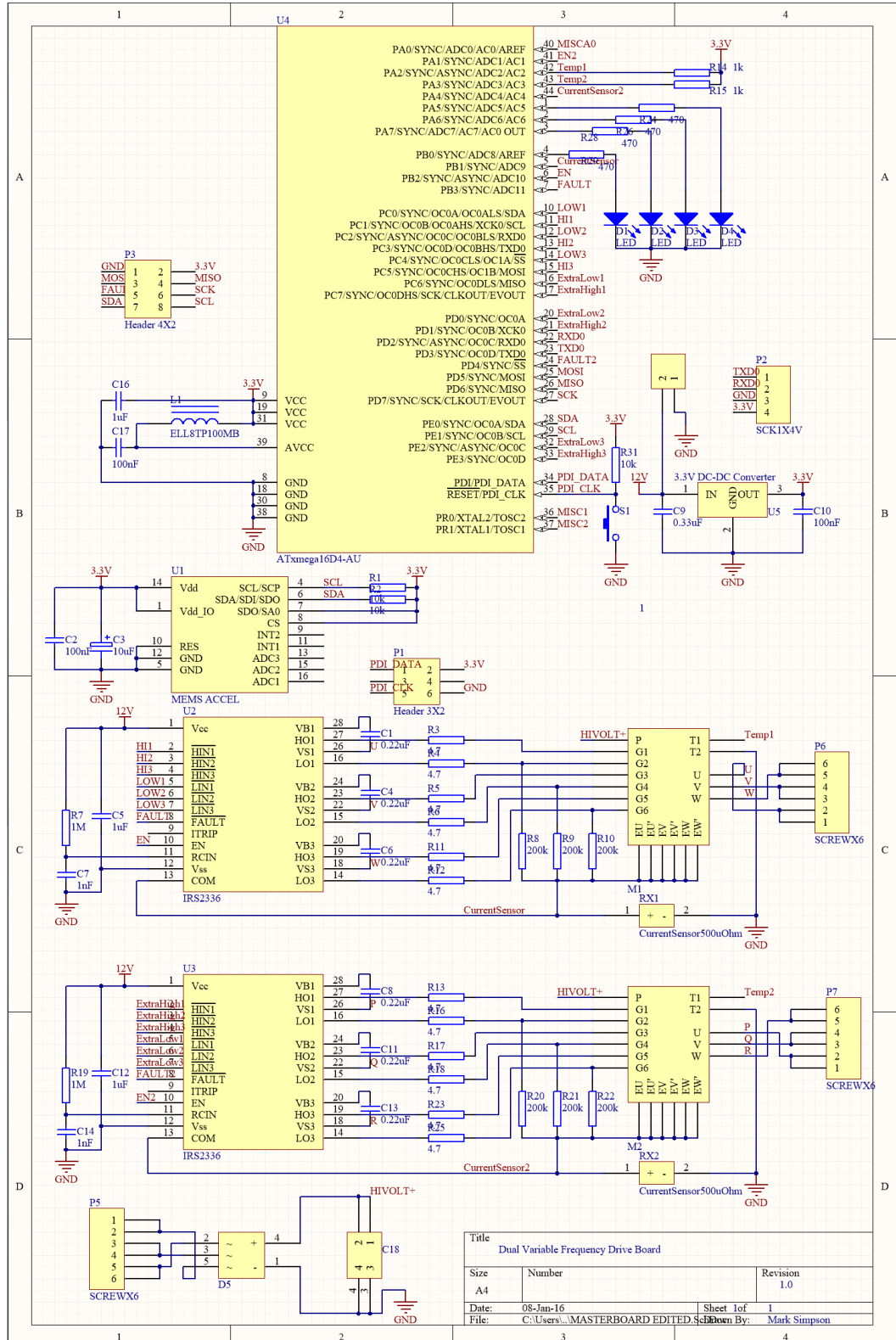
The LIM vehicle created shows that continuous track reaction plates can indeed be used together with LIM stators to create a robotic vehicle capable of climbing steel walls. The tracked vehicle was demonstrated to be capable of producing 90N of thrust when 1.7kW of electrical power is applied. The targeted operating frequency ranged from 10-20Hz and used an adaptation of Volts-per-Hertz control with a maximum tested operating voltage of 220V and maximum phase current of 7A. Tracked LIM vehicles have advantages over other wall climbing vehicles due to the simpler method of operation, fewer parts requiring maintenance and the ruggedness of the vehicle. From a physical standpoint, the biggest drawback of the vehicle was its large weight due to the heavy laminations used in the stators and weight of all of the copper windings, totaling 28kg. Despite the large weight, the vehicle was shown to be capable of climbing a steel backing plate.

The coupling between the attractive force and thrust developed were explored in detail for locked rotor conditions, with comparisons made between calculated results, simulated results and results validated experimentally. The results showed that the single greatest factor in limiting efficiency was due to the amount of leakage flux due to having a large airgap – required to ensure clearance between the reaction plate track and stator to allow movement. This leakage flux caused a large magnetizing current to flow, resulting in excessive heating of the windings when attempting to achieve large thrusts, forcing the controller to operate over a range not intended for when designed and limited further investigations.

Overall, this research placed emphasis on designing and creating a working prototype vehicle and studying its performance and attributes. The author hopes the foundation formed will serve as a platform from which further research can develop into the future.

Appendix A Inverter Schematic/PCB

A.1 Schematic Diagram



Appendix B Inverter Program Code

```
/*
 * DualBoard.c
 *
 * Created: 28-Jan-15 11:31:35 AM
 * Author: Mark
 */

/**
 * The input/output pins of the ATXmega16D4 microcontroller are
 * described as follows:
 *
 * PA0 - MISCELLANEOUS
 * PA1 - Enable IGBT Driver 2
 * PA2/PA3 - Temperature of IGBT Module 1 and 2
 * PA4 - Current Sensor 2
 * PA5/PA6/PA7 - LED Outputs
 *
 * PB0 - LED Outputs
 * PB1 - Current Sensor 1
 * PB2 - Dump Resistor
 * PB3 - FAULT for IGBT Driver 1
 *
 * PC1/PC0 - OC0AHS/OC0ALS (Phase 1)
 * PC3/PC2 - OC0BHS/OC0BLS (Phase 2)
 * PC5/PC4 - OC0CHS/OC0CLS (Phase 3)
 * PC7/PC6 - OC0DHS/OC0DLS (Phase 4)
 *
 * PD1/PD0 - Manual HI/LO (Phase 5)
 * PD2/PD3 - RXD0 / TXD0
 * PD4 - FAULT for IGBT Driver 2
 * PD5/PD6/PD7 - NOT USED (MOSI / MISO / SCK)
 *
 * PE0/PE1 - SDA/SCL (for accelerometer)
 * PE3/PE2 - Manual HI/LO (Phase 6)
 */

#define F_CPU 32000000

#include <avr/io.h>
#include <util/delay.h>
#include "usart_driver.h"
#include "avr_compiler.h"
#include "twi_master_driver.h"
#include <string.h>
#include <stdio.h>
#include <math.h>

#define DEAD_TIME_CYCLES 16
#define ACCEL_ADDR 0b0011001
/*! Defining number of bytes in buffer. */
#define NUM_BYTES 7
#define USART USARTD0
/*! CPU speed 8MHz, BAUDRATE 100kHz and Baudrate Register Settings */
```

```

#define TWIBAUDRATE 100000
#define TWI_BAUDSETTING TWI_BAUD(F_CPU, TWIBAUDRATE)
#define nop() do { __asm__ __volatile__ ("nop"); } while (0)
#define CTRL_REG1 0x20
#define CTRL_REG2 0x21
#define CTRL_REG3 0x22
#define CTRL_REG4 0x23
#define CTRL_REG5 0x24
#define CTRL_REG6 0x25
#define REFERENCE 0x26
#define STATUS_REG 0x27
#define OUT_X_H 0x29
#define OUT_Y_H 0x2B
#define OUT_Z_H 0x2D

uint16_t timerTopValue = 5926;
uint16_t timerTopValueTwo = 5926;
float powerScalingFactor = 0.4;
float powerScalingFactorTwo = 0.4;
uint16_t sineTable[90];
uint16_t sineTableTwo[90];
float modifier = 1000;
float modifierTwo = 1000;

TWI_Master_t twiMaster; /*!< TWI master module. */
USART_data_t USART_data; /*! USART data struct */

/*! Buffer with test data to send.*/
uint8_t sendBuffer[22] = {0x0F, CTRL_REG1, 0x27, CTRL_REG2, 0,
CTRL_REG3, 0, CTRL_REG4, 0x08, CTRL_REG5, 0, CTRL_REG6, 0, REFERENCE,
0, STATUS_REG, 0x28, 0x29, 0x2A, 0x2B, 0x2C, 0x2D}; //FOR TWI
uint8_t test = 0;

/*! Test data to send. */
uint8_t sendArray[NUM_BYTES] = {0x10, 0x15, 0x20, 0x28, 0x2A, 0x2C,
0x00};
/*! Array to put received data in. */
uint8_t receiveArray[NUM_BYTES];

int8_t dataArray[3];
float gForceArray[3];
uint8_t accelOutputs[3] = {OUT_X_H, OUT_Y_H, OUT_Z_H};
uint8_t receiveBufPos = 0;
uint8_t messageReceived = 0;

/*! Global Variables for PWM interrupt -- made global to add reversing
functionality */
volatile uint8_t iIndex = 0;
volatile uint8_t jIndex = 30;
volatile uint8_t kIndex = 60;
volatile uint8_t i2Index = 0;
volatile uint8_t j2Index = 30;
volatile uint8_t k2Index = 60;

/*! Print Buffer for Bluetooth */
static char printBuffer[100];

```

```

void initAccelerometer(void);
void readAccelerometer(void);
void printString(char* str);
void setupClocks(void);
void setupIGBTs(void);
void setupPinDirections(void);
void setupUSART(void);
void setupTWI(void);
void readMessage(uint8_t* message);
void checkForMessages(void);

int main( void )
{
    cli(); //Sanity Check
    setupClocks();
    setupIGBTs();
    setupPinDirections();
    setupUSART();
    setupTWI();

    /* Enable low level interrupts. */
    PMIC.CTRL = PMIC_LOLVLEN_bm;

    /* Generate the custom SINE table */
    for (int c=0; c<90; c++){sineTable[c] = (int)
1185*(sin(6.28319*c/90)+1);}
    for (int c=0; c<90; c++){sineTableTwo[c] = (int)
1185*(sin(6.28319*c/90)+1);}

    sei();

    initAccelerometer();

    do {

        checkForMessages();
        readAccelerometer();
        PORTB.OUTTGL = PIN0_bm; //Switch the Red LED to indicate a
regular heartbeat
        _delay_ms(200);

    } while (1);
}

void printString(char* str){
    uint8_t length = strlen(str);
    uint8_t i = 0;
    bool byteToBuffer;
    // for each character in the string
    while (i < length) {
        byteToBuffer = USART_TxBuffer_PutByte(&USART_data, str[i]);
        if(byteToBuffer){
            _delay_ms(10); //THIS DELAY IS REQUIRED TO ALLOW TIME FOR
DATA TO BE PROCESSED
            i++;
        }
    }
}

```

```

}

void initAccelerometer(void) {
    _delay_ms(5);
    TWI_MasterWriteRead(&twiMaster, ACCEL_ADDR, &sendBuffer[1], 2, 0);
    while (twiMaster.status != TWIM_STATUS_READY);
    _delay_ms(5);
    TWI_MasterWriteRead(&twiMaster, ACCEL_ADDR, &sendBuffer[3], 2, 0);
    while (twiMaster.status != TWIM_STATUS_READY);
    _delay_ms(5);
    TWI_MasterWriteRead(&twiMaster, ACCEL_ADDR, &sendBuffer[5], 2, 0);
    while (twiMaster.status != TWIM_STATUS_READY);
    _delay_ms(5);
    TWI_MasterWriteRead(&twiMaster, ACCEL_ADDR, &sendBuffer[7], 2, 0);
    while (twiMaster.status != TWIM_STATUS_READY);
    _delay_ms(5);
    TWI_MasterWriteRead(&twiMaster, ACCEL_ADDR, &sendBuffer[9], 2, 0);
    while (twiMaster.status != TWIM_STATUS_READY);
    _delay_ms(5);
    TWI_MasterWriteRead(&twiMaster, ACCEL_ADDR, &sendBuffer[11], 2,
0);
    while (twiMaster.status != TWIM_STATUS_READY);
    _delay_ms(5);
    TWI_MasterWriteRead(&twiMaster, ACCEL_ADDR, &sendBuffer[13], 2,
0);
    while (twiMaster.status != TWIM_STATUS_READY);
    _delay_ms(5);
}

void readAccelerometer(void) {
    // Read the accelerometer X, Y, Z (0, 0, 64 for flat and
stationary)
    for (int i=0; i<3; i++)
    {
        TWI_MasterWriteRead(&twiMaster, ACCEL_ADDR, &accelOutputs[i],
1, 1);
        while (twiMaster.status != TWIM_STATUS_READY);
        dataArray[i] = (twiMaster.readData[0]);
        if (dataArray[i]>127)
        {
            dataArray[i] = 0-(~dataArray[i] + 1);
        }
    }
    sprintf(printBuffer, "X: %d, Y: %d, Z: %d\r\n", dataArray[0],
dataArray[1], dataArray[2]);
    printString(printBuffer);
}

void checkForMessages(void) {
    /* Fetch received data as it is received. */
    if (USART_RXBufferData_Available(&USART_data)) {
        receiveArray[receiveBufPos] =
USART_RXBuffer_GetByte(&USART_data);
        receiveBufPos++;
        messageReceived = 1;
        PORTA.OUTSET = PIN5_bm;
    }
}

```

```

        if ((messageReceived==1)&&(receiveBufPos>2)){ //Want a new message
to be there, and the message at least three characters long
            readMessage(receiveArray);
        }
    }

void setupClocks(void){
    /* Start internal 32MHz RC oscillator. */
    OSC.CTRL = OSC_RC32MEN_bm;
    do {
        /* Wait while oscillator stabilizes. */
    } while ( ( OSC.STATUS & OSC_RC32MRDY_bm ) == 0 );
    /* Enable prescaler B and C. */
    //CCP = CCP_IOREG_gc; CLK.PSCTRL = CLK_PSBCDIV_2_2_gc; //Divides
both B and C by 2
    CCP = CCP_IOREG_gc; CLK.PSCTRL = CLK_PSBCDIV_1_1_gc;
    /* Select 32 MHz as master clock. */
    CCP = CCP_IOREG_gc; CLK.CTRL = CLK_SCLKSEL_RC32M_gc;
    //MasterClock==ClkPer4==32Mhz, ClkPer2==16Mhz, ClkPer==ClkCPU==8Mhz
    }

void setupIGBTs(void){
    /* Configure dead time insertion. */
    AWEXC.CTRL = AWEX_DTICCAEN_bm | AWEX_DTICCBEN_bm |
AWEX_DTICCCEN_bm; //Insert on output A, B and C
    AWEXC.OUTOVEN = 0x3F; //Override pin 0 - 6 actions (but must still
be configured as output)
    AWEXC.DTBOTH = DEAD_TIME_CYCLES; //select desired deadtime

    /* Enable output for PWM on PORTD and PORTE and invert the second
output. */
    PORTD.DIRSET = PIN0_bm | PIN1_bm;
    PORTD.PIN1CTRL = PORT_INVEN_bm;
    PORTE.DIRSET = PIN2_bm | PIN3_bm;
    PORTE.PIN3CTRL = PORT_INVEN_bm;

    PORTC.PIN6CTRL = PORT_INVEN_bm; //Invert Low Side so when OUTSET
is called the bridge is ON, and is OFF on OUTCLR

    /* Configure timer. */
    TCC0.PER = timerTopValue;
    TCC0.CTRLB = TC0_CCAEN_bm | TC0_CCBEN_bm | TC0_CCCEN_bm |
TC_WGMODE_DS_T_gc;
    TCC0.INTCTRLA = TC_OVFINTLVL_LO_gc;
    TCC0.CTRLA = TC_CLKSEL_OFF_gc; //IGBT1 clock initially off

    /* Configure timers for second inverter */
    TCD0.PER = timerTopValueTwo; //Initial carrier frequency (for
30Hz)
    TCD0.CTRLB = TC0_CCAEN_bm | TC0_CCBEN_bm | TC_WGMODE_DS_T_gc;
    //Dual slope PWM
    TCE0.PER = timerTopValueTwo;
    TCE0.CTRLB = TC0_CCCEN_bm | TC0_CCDEN_bm | TC_WGMODE_DS_T_gc;
    TCD0.INTCTRLA = TC_OVFINTLVL_LO_gc; //Interrupt to low level
    TCE0.INTCTRLA = TC_OVFINTLVL_LO_gc;
    TCD0.INTCTRLB = TC_CCCINTLVL_LO_gc; //Interrupt on capture/compare

```

```

    TCD0.CTRLA = TC_CLKSEL_DIV1_gc; //Start the Timer
    TCE0.CTRLA = TC_CLKSEL_DIV1_gc;

}

void setupPinDirections(void) {

    /* PORTC as outputs. */
    PORTC.DIR = 0xFF;

    /* Set data direction for LEDs */
    PORTA.DIRSET = PIN7_bm | PIN6_bm | PIN5_bm;
    PORTB.DIRSET = PIN0_bm;

    /* Set IGBT 2 Enable Pin as Output (IGBT 1 Controlled by switching
of TCC0 clock) */
    PORTA.DIRSET = PIN1_bm; //Unit 2

    /* Set DUMP RESISTOR resistor pin as output */
    PORTB.DIRSET = PIN2_bm;
}

void setupUSART(void) {
    //This step must go before the output set below as per Datasheet
    PORTD.OUTSET = PIN3_bm;
    /* PD3 (TXD0) as output. */
    PORTD.DIRSET = PIN3_bm;

    /* PD2 (RXD0) as input. */
    PORTD.DIRCLR = PIN2_bm;
    /* Use USARTD0 and initialize buffers. */
    USART_InterruptDriver_Initialize(&USART_data, &USART,
USART_DREINTLVL_LO_gc);

    /* Set Baudrate to 9600 bps */
    USART_Baudrate_Set(&USART, 12 , 4); //For 32MHz

    /* USARTD0, 8 Data bits, No Parity, 1 Stop bit. */
    USART_Format_Set(USART_data.usart, USART_CHSIZE_8BIT_gc,
USART_PMODE_DISABLED_gc, false);

    /* Enable RXC interrupt. */
    USART_RxdInterruptLevel_Set(USART_data.usart,
USART_RXCINTLVL_LO_gc);

    /* Enable both RX and TX. */
    USART_Rx_Enable(USART_data.usart);
    USART_Tx_Enable(USART_data.usart);
}

void setupTWI(void) {
    /* Initialize TWI master. */
    TWI_MasterInit(&twiMaster, &TWIE, TWI_MASTER_INTLVL_LO_gc,
TWI_BAUDSETTING);
}

```

```

void readMessage(uint8_t* message){
    switch (message[0]){
        case 'S':
            switch (message[2]){
                case '0':
                    //Turn both IGBTs OFF
                    PORTB.OUTSET = PIN2_bm; //DUMP RESISTOR ON
                    TCC0.CTRLA = TC_CLKSEL_OFF_gc; //Disable the CC timers for
IGBT1
                    PORTA.OUTCLR = PIN1_bm; //IGBT2 Disable
                    _delay_ms(1);
                    PORTB.OUTCLR = PIN2_bm; //DUMP RESISTOR OFF
                    break;
                case '1':
                    //Turn both IGBTs ON
                    TCC0.CTRLA = TC_CLKSEL_DIV1_gc; //Enable the CC timers for
IGBT1
                    PORTA.OUTSET = PIN1_bm; //IGBT2 Enable
                    break;
            }
            break;
        case 'L':
            switch (message[1]){
                case 'F':
                    //Left Freq should be set to message[2] value
                    PORTB.OUTSET = PIN2_bm; //DUMP RESISTOR ON
                    cli();
                    modifier = (int) message[2];
                    modifier = (float) 177778/modifier; //Convert frequency to
a TOP value
                    timerTopValue = (int) modifier;
                    TCC0.PER = timerTopValue;
                    modifier = powerScalingFactor*timerTopValue/2;
                    for (int c=0; c<90; c++){sineTable[c] = (int)
modifier*(sin(6.28319*c/90)+1);}
                    sei();
                    PORTB.OUTCLR = PIN2_bm; //DUMP RESISTOR OFF
                    break;
                case 'P':
                    //Left Power should be set to message[2] value
                    PORTB.OUTSET = PIN2_bm; //DUMP RESISTOR ON
                    cli();
                    powerScalingFactor = (int)message[2];
                    powerScalingFactor = (float) powerScalingFactor/100;
                    modifier = powerScalingFactor*timerTopValue/2;
                    for (int c=0; c<90; c++){sineTable[c] = (int)
modifier*(sin(6.28319*c/90)+1);}
                    //Calculate phase shift for balancing
                    modifier = (int) message[2];
                    volatile uint8_t iIndex = (int)
14.3239*(atan(6.28319*modifier*0.035/3.3));
                    volatile uint8_t jIndex = (int)
14.3239*(2.094+atan(6.28319*modifier*0.038/3.4));
                    volatile uint8_t kIndex = (int)
14.3239*(4.189+atan(6.28319*modifier*0.034/3.3));
                    sei();
                    PORTB.OUTCLR = PIN2_bm; //DUMP RESISTOR OFF
            }
        }
    }
}

```

```

        break;
        case 'R':
            //Reverse Left IGBT
            PORTB.OUTSET = PIN2_bm; //DUMP RESISTOR ON
            cli();
            uint8_t temp = iIndex;
            iIndex = jIndex;
            jIndex = temp;
            sei();
            PORTB.OUTCLR = PIN2_bm; //DUMP RESISTOR OFF
            break;
        case 'S':
            //Start/Stop Left IGBT
            if (message[2]==1){
                TCC0.CTRLA = TC_CLKSEL_DIV1_gc; //Enable the CC timers
for IGBT1
                } else {
                PORTB.OUTSET = PIN2_bm; //DUMP RESISTOR ON
                TCC0.CTRLA = TC_CLKSEL_OFF_gc; //Disable the CC timers
for IGBT1
                _delay_ms(1);
                PORTB.OUTCLR = PIN2_bm; //DUMP RESISTOR OFF
            }
            break;
    }
    break;
    case 'R':
        switch (message[1]){
            case 'F':
                //Right Freq should be set to message[2] value
                PORTB.OUTSET = PIN2_bm; //DUMP RESISTOR ON
                cli();
                modifierTwo = (int) message[2];
                modifierTwo = (float) 177778/modifierTwo; //Convert
frequency to a TOP value
                timerTopValueTwo = (int) modifierTwo;
                TCD0.PER = timerTopValueTwo;
                TCE0.PER = timerTopValueTwo;
                modifierTwo = powerScalingFactorTwo*timerTopValueTwo/2;
                for (int c=0; c<90; c++){sineTableTwo[c] = (int)
modifierTwo*(sin(6.28319*c/90)+1);}
                sei();
                PORTB.OUTCLR = PIN2_bm; //DUMP RESISTOR OFF
                break;
            case 'P':
                //Right Power should be set to message[3] value
                PORTB.OUTSET = PIN2_bm; //DUMP RESISTOR ON
                cli();
                powerScalingFactorTwo = (int)message[2];
                powerScalingFactorTwo = (float) powerScalingFactorTwo/100;
                modifierTwo = powerScalingFactorTwo*timerTopValueTwo/2;
                for (int c=0; c<90; c++){sineTableTwo[c] = (int)
modifierTwo*(sin(6.28319*c/90)+1);}
                //Calculate phase shift for balancing
                modifierTwo = (int) message[2];
                volatile uint8_t iIndex = (int)
14.3239*(atan(6.28319*modifierTwo*0.038/3.3));

```

```

        volatile uint8_t jIndex = (int)
14.3239*(2.094+atan(6.28319*modifierTwo*0.039/3.3));
        volatile uint8_t kIndex = (int)
14.3239*(4.189+atan(6.28319*modifierTwo*0.032/3.2));

        sei();
        PORTB.OUTCLR = PIN2_bm; //DUMP RESISTOR OFF
        break;
        case 'R':
            //Reverse Right IGBT
            PORTB.OUTSET = PIN2_bm; //DUMP RESISTOR ON
            cli();
            uint8_t temp = i2Index;
            i2Index = j2Index;
            j2Index = temp;
            sei();
            PORTB.OUTCLR = PIN2_bm; //DUMP RESISTOR OFF
            break;
        case 'S':
            //Start/Stop Right IGBT
            if (message[2]==1){
                PORTA.OUTSET = PIN1_bm; //IGBT2 Enable
            } else {
                PORTB.OUTSET = PIN2_bm; //DUMP RESISTOR ON
                PORTA.OUTCLR = PIN1_bm; //IGBT2 Disable
                _delay_ms(1);
                PORTB.OUTCLR = PIN2_bm; //DUMP RESISTOR OFF
            }
            break;
    }
    break;
}
receiveBufPos = 0;
messageReceived = 0;
PORTA.OUTCLR = PIN5_bm;
}

/*
 *   ISR - Updates sine value
 */
ISR(TCC0_OVF_vect)
{
    /* Write the next output compare A, B and C value. */
    TCC0.CCABUF = sineTable[iIndex];
    TCC0.CCBBUF = sineTable[jIndex];
    TCC0.CCCBUF = sineTable[kIndex];

    /* Increment table index. */
    iIndex++;
    jIndex++;
    kIndex++;
    if(iIndex>89){ iIndex = 0; }
    if(jIndex>89){ jIndex = 0; }
    if(kIndex>89){ kIndex = 0; }
}

ISR(TCD0_CCC_vect)

```

```

{
    PORTC.OUTTGL = PIN6_bm | PIN7_bm;
}

ISR(TCD0_OVF_vect)
{
    PORTC.OUTSET = PIN6_bm | PIN7_bm;

    /* Write the next output compare A and B value. */
    TCD0.CCABUF = sineTableTwo[j2Index];
    TCD0.CCBBUF = sineTableTwo[j2Index];
    TCD0.CCCBUF = sineTableTwo[i2Index];

    /* Increment table index. */
    i2Index++;
    j2Index++;
    if(i2Index>89){ i2Index = 0; }
    if(j2Index>89){ j2Index = 0; }

}

ISR(TCE0_OVF_vect)
{
    /* Write the next output compare C and D value. */
    TCE0.CCCBUF = sineTableTwo[k2Index];
    TCE0.CCDBUF = sineTableTwo[k2Index];

    /* Increment table index. */
    k2Index++;
    if(k2Index>89){ k2Index = 0; }

}

/*! TWIE Master Interrupt vector. */
//ISR(TWIE_TWIM_vect)
//{
//    TWI_MasterInterruptHandler(&twiMaster);
//}

/*! \brief Receive complete interrupt service routine.
 *
 * Receive complete interrupt service routine.
 * Calls the common receive complete handler with pointer to the
correct USART
 * as argument.
 */
ISR(USARTD0_RXC_vect)
{
    USART_RXComplete(&USART_data);
}

/*! \brief Data register empty interrupt service routine.
 *
 * Data register empty interrupt service routine.
 * Calls the common data register empty complete handler with pointer
to the

```

```
* correct USART as argument.  
*/  
ISR(USARTD0_DRE_vect)  
{  
    USART_DataRegEmpty(&USART_data);  
}
```

Appendix C Raw Experimental Data

Measuring DC current input, power input, RMS phase currents, thrust

developed and normal force for different airgaps (in mm) and ply of aluminum reaction plate (1 ply is 1.5mm thick). Squares with yellow backgrounds implies a decreased airgap due to flex in the backing plate, in turn reducing input current.

Airgap	Ply	Voltage (V)	DC Current In (A)			Power In (W)			Current RMS (A)			Thrust (N)			Normal Force (N)		
			12.5Hz	25Hz	50Hz	12.5Hz	25Hz	50Hz	12.5Hz	25Hz	50Hz	12.5Hz	25Hz	50Hz	12.5Hz	25Hz	50Hz
1	0	20	0.18	0.08	0.05	3.6	1.7	1.0	0.3	0.2	0.1					0.0	0.0
		40	0.30	0.15	0.11	12.3	6.1	4.4	0.6	0.3	0.2					4.4	2.7
		60	0.43	0.23	0.18	26.1	13.6	10.6	0.8	0.5	0.3					17.8	5.3
		80	0.58	0.31	0.26	46.3	24.6	20.6	1.1	0.6	0.4					35.6	15.1
		100	0.77	0.39	0.32	76.9	38.7	31.9	1.5	0.8	0.5					44.5	32.9
		120	1.01	0.47	0.38	121.5	56.7	45.6	1.9	1.0	0.5					53.4	41.8
3	0	20	0.28	0.13	0.07	5.6	2.7	1.3	0.4	0.3	0.2					0.0	0.0
		40	0.53	0.24	0.13	21.2	9.6	5.2	0.9	0.6	0.3					5.3	1.8
		60	0.77	0.35	0.21	46.1	20.9	12.3	1.4	0.9	0.5					17.8	6.2
		80	0.94	0.31	0.28	75.5	25.0	22.7	1.8	0.6	0.7					35.6	10.7
		100	1.11	0.39	0.35	110.5	39.0	34.8	2.1	0.8	0.9					44.5	15.1
		120		0.48	0.41		57.2	48.1		0.9	1.0					53.4	19.6
	1	20	0.33	0.20	0.13	7.5	4.1	2.7	0.4	0.3	0.2	0.0	0.0	0.0		0.0	0.0
		40	0.74	0.41	0.28	29.9	16.2	11.2	1.0	0.6	0.4	1.6	0.9	0.0		5.3	2.7
		60	1.19	0.62	0.44	67.7	37.0	26.6	1.6	1.0	0.6	4.4	2.6	1.1		10.7	3.6
		80	1.51	0.82	0.60	121.5	65.6	48.0	2.1	1.3	0.9	8.0	4.2	2.2		19.6	6.2
		100	1.94	1.02	0.74	195.3	101.8	74.4	2.8	1.6	1.1	10.5	5.1	3.4		28.5	10.7
		120		1.22	0.88		147.0	####		1.9	1.3		5.1	5.0		35.6	19.6
5	0	20	0.39	0.16	0.08	8.0	3.3	1.5	0.5	0.3	0.2					0.0	0.0
		40	0.78	0.30	0.14	31.5	12.1	5.7	1.2	0.7	0.4					2.7	1.8
		60	1.19	0.45	0.23	71.9	26.9	13.7	1.8	1.1	0.6					11.6	4.0
		80	1.63	0.57	0.31	131.4	45.9	24.8	2.6	1.4	0.8					26.7	6.2
		100	2.13	0.66	0.38	214.2	65.7	37.9	3.4	1.7	1.0					35.6	8.5
		120		0.50	0.45		60.0	53.7		1.1	1.2					71.2	10.7
	1	20	0.43	0.22	0.13	8.6	4.4	2.7	0.5	0.3	0.2	0.0	0.0	0.0		0.0	0.0
		40	0.86	0.43	0.27	34.6	17.1	10.9	1.1	0.7	0.5	1.2	0.9	0.0		4.4	0.0
		60	1.31	0.64	0.43	78.8	38.8	26.0	1.8	1.1	0.7	3.6	3.1	0.7		11.6	0.0
		80	1.79	0.86	0.58	143.7	68.7	46.9	2.5	1.5	1.0	6.5	4.2	2.0		17.8	4.4
		100	2.29	1.05	0.73	231.0	105.5	72.9	3.3	1.8	1.2	10.2	7.6	2.9		26.7	5.3
		120		1.24	0.87		148.7	####		2.1	1.4		11.8	4.2		35.6	6.2
	2	20	0.46	0.26	0.17	9.3	5.3	3.3	0.5	0.4	0.2	0.0	0.0	0.0		0.0	0.0
		40	0.95	0.53	0.35	38.2	21.4	13.3	1.1	0.8	0.5	1.7	1.3	0.0		3.6	0.0
		60	1.45	0.82	0.55	87.5	49.1	33.0	1.8	1.2	0.8	6.0	3.3	1.1		6.2	0.0
		80	1.97	1.09	0.74	159.1	87.4	59.3	2.6	1.7	1.1	10.6	6.9	2.6		8.9	0.0
		100	2.54	1.36	0.91	255.0	136.4	91.5	3.3	2.1	1.4	11.7	11.3	4.1		17.8	4.4
		120		1.64	1.08		197.0	####		2.5	1.7		13.3	6.1		26.7	5.3

7	0	20	0.46	0.19	0.08	9.1	3.9	1.7	0.5	0.4	0.2				0.0	0.0
		40	0.91	0.36	0.16	36.6	14.5	6.2	1.3	0.8	0.5				2.7	0.0
		60	1.39	0.54	0.25	83.7	32.5	14.8	2.0	1.3	0.7				5.3	0.0
		80	1.91	0.71	0.33	154.2	56.7	26.9	2.9	1.7	0.9				13.3	4.4
		100	2.48	0.85	0.41	250.6	85.7	41.2	3.7	2.1	1.2				26.7	4.4
		120		0.98	0.49		117.7	58.1		2.5	1.4				40.0	4.4
	1	20	0.48	0.23	0.13	9.5	4.7	2.6	0.5	0.4	0.2	0.0	0.0	0.0	0.0	0.0
		40	0.96	0.46	0.27	38.6	18.3	10.7	1.2	0.8	0.5	0.9	0.4	0.0	2.7	0.0
		60	1.46	0.69	0.43	88.5	41.5	25.6	2.0	1.3	0.8	2.6	1.8	0.7	5.3	0.0
		80	2.01	0.92	0.57	162.2	73.6	45.0	2.7	1.7	1.0	5.6	3.3	1.5	8.9	0.0
		100	2.62	1.13	0.70	263.2	113.9	70.4	3.6	2.2	1.3	8.6	5.5	2.4	17.8	4.4
		120		1.24	0.82		136.6	98.6		2.4	1.5		7.5	3.5	26.7	4.4
	2	20	0.50	0.27	0.16	10.1	5.5	3.2	0.5	0.4	0.3	0.0	0.0	0.0	0.0	0.0
		40	1.03	0.54	0.32	41.4	21.8	13.0	1.2	0.9	0.5	1.8	0.9	0.0	0.0	0.0
		60	1.57	0.83	0.52	94.7	49.9	31.0	2.0	1.3	0.8	5.4	3.1	1.1	4.4	0.0
		80	2.14	1.11	0.69	172.7	89.0	55.4	2.8	1.8	1.1	9.4	5.9	2.4	8.9	0.0
		100	2.77	1.38	0.86	279.4	138.5	82.0	3.6	2.3	1.4	15.0	9.3	3.8	16.0	4.4
		120		1.62	1.01		194.6	93.6		2.7	1.6		13.6	5.4	24.0	6.7
	3	20	0.53	0.31	0.18	10.6	6.1	3.5	0.5	0.4	0.3	0.0	0.0	0.0		0.0
		40	1.08	0.62	0.36	43.6	24.9	14.5	1.3	0.9	0.6	2.2	1.3	0.0		0.0
		60	1.65	0.95	0.57	100.0	57.1	34.3	2.0	1.4	0.9	6.7	3.9	1.0		0.0
		80	2.26	1.25	0.77	182.5	100.1	61.7	2.8	1.9	1.3	11.9	7.3	2.2		0.0
		100	2.92	1.54	0.98	294.0	154.1	96.5	3.6	2.4	1.6	15.0	11.6	3.9		0.0
		120		1.84	1.24		222.0	####		2.9	2.1		16.5	7.1		

This table shows the experimentally collected data for the thrust generated for different reaction plate lengths, with and without a backing plate present. The data collected is for a single segment, but the results are multiplied by the number of segments that could fit along the length of the stator to get the value in the 'Total' column.

Length (mm)	Thrust (No Backing Plate) (N)	Thrust (W/ Backing Plate) (N)	Segments Incl Hinge per 41cm	Total
360	4.61	15.11	1.12	16.92
340	3.83	13.73	1.18	16.27
320	3.43	14.13	1.26	17.77
300	3.34	13.54	1.34	18.14
280	3.34	13.15	1.43	18.84
260	2.94	11.58	1.54	17.84
240	2.84	11.67	1.67	19.46
220	2.65	10.50	1.81	19.04
200	2.26	8.93	1.99	17.77
180	2.16	8.63	2.20	19.03
160	1.96	7.26	2.47	17.93
140	1.47	6.28	2.81	17.63
120	1.28	4.71	3.25	15.32
100	0.98	3.53	3.87	13.66
80	0.69	3.04	4.77	14.50

This section contains the data when testing the finalized 3-ply reaction plate track to measure DC current input, power input, RMS current and thrust developed for a 3mm airgap using a single stator.

Voltage (V)	DC Current In (A)			Power In (W)			Current RMS (A)			Thrust (N)		
	12.5Hz	25Hz	50Hz	12.5Hz	25Hz	50Hz	12.5Hz	25Hz	50Hz	12.5Hz	25Hz	50Hz
20	0.56	0.32	0.19	11.1	6.3	3.7	0.5	0.4	0.3	0.0	0.0	0.0
40	1.15	0.64	0.38	46.0	25.7	15.2	1.1	0.9	0.6	2.2	1.2	0.0
60	1.76	0.98	0.60	105.4	59.0	36.0	1.8	1.5	1.0	6.2	2.8	0.0
80	2.27	1.32	0.81	181.7	105.4	65.0	2.5	2.0	1.2	12.4	6.9	0.6
100	3.09	1.65	1.01	309.0	164.7	101.3	3.3	2.5	1.6	20.7	10.4	1.5
120	3.83	1.97	1.21	460.0	235.8	145.1	4.3	3.1	1.9	31.1	16.0	4.6
140	4.56	2.31	1.38	639.0	323.0	193.0	5.2	3.7	2.2	43.0	22.3	7.2
160		2.66	1.57		426.0	250.7		4.3	2.5		29.3	9.9
180		2.98	1.76		536.0	316.8		4.9	2.9		37.8	13.0
200		3.43			686.0			5.5			47.7	

The completed vehicle was then tested on the backing plate with power applied to both stators at the same time using a DC power supply capable of sourcing up to 11.5A. The vehicle had an approximately 5mm and was operated on 3-ply aluminium reaction plates at 12.5Hz.

Voltage (V)	DC Current In (A)	RMS Current (A)	Thrust (N)
50	3.11	2.1	5.0
60	3.76	2.5	6.3
70	4.45	3.0	11.0
80	5.12	3.4	16.8
90	5.85	3.9	23.0
100	6.64	4.4	31.0
110	7.43	5.0	38.5
120	8.25	5.5	49.1
130	8.9	5.9	57.6
140	9.6	6.4	68.2
150	10.3	6.9	79.0
160	11.1	7.4	90.3

List of References

- [1] G. Lee, H. Kim, K. Seo, J. Kim and H. Kim, "MultiTrack: A multi-linked track robot with suction adhesion for climbing and transition," *Robots and Autonomous Systems*, no. 72, pp. 207-216, 2015.
- [2] E. Purcell and D. Morin, *Electricity and Magnetism*, Cambridge University Press, 2013.
- [3] R. T. Schneider, "Designing with Vacuum and Suction Cups," *Hydraulics & Pneumatics*, vol. 55, no. 7, pp. 16-18, Jul 2002.
- [4] A. Sintov, T. Avramovich and A. Shapiro, "Design and Motion Planning of an Autonomous Climbing Robot with Claws," *Robotics and Automation Systems*, vol. 59, no. 11, pp. 1008-1019, 2011.
- [5] C. Cao, X. Sun, Y. Fang, Q. Qin, A. Yu and X. Feng, "Theoretical Model and Design of Electroadhesive Pad with Interdigitated Electrodes," *Materials and Design*, vol. 89, pp. 485-491, 2016.
- [6] L. Bouffier, V. Ravaine, N. Sojic and A. Kuhn, "Electric Fields for Generating Unconventional Motion of Small Objects," *Current Opinion in Colloid and Interface Science*, 2015.
- [7] D. H. Myszka, *Machines and Mechanisms: Applied Kinematic Analysis*, New Jersey: Prentice Hall, 2002.

- [8] S. El-Ghanam, "Performance of Some Oscillator Circuits in Different Environmental Conditions," *Journal of Electrical and Electronics Engineering*, vol. 3, no. 2, 2010.
- [9] G. Laxminarayana and K. Pradeep, "Comparative Analysis of 3-, 5- and 7-Level Inverter Using Space Vector PWM," *International Journal of Advanced Research in Electrical, Electronics and Instrumentation Engineering*, vol. 2, no. 7, 2013.
- [10] V. Radhkrishnan, S. Baghel and A. Taylor, "A Maximum Constant Boost Quasi-Z Source Inverter with Third Harmonic Injection for Linear Induction Motors," in *International Conference on Advances in Computing, Electronics and Communication*, Zurich, 2015.
- [11] J. V. M. P. L. O. Ellabban, "Experimental Study of the Shoot-Through Boost Control Methods for the Z-Source Inverter," *EPE Journal*, vol. 21, no. 2, pp. 18-29, 2011.
- [12] J. Nikander, "Induction Motor Parameter Identification in Elevator Drive Modernization," Helsinki University of Technology, 2009.
- [13] International Rectifier, "IGBT Characteristics," 2012.
- [14] J. Strydom, "A comparison of fundamental gate-driver topologies for high frequency applications," in *Applied Power Electronic and Exposition*, 2004.
- [15] B. Jayant Baliga, *Advanced High Voltage Power Device Concepts*, Springer, 2011.

- [16] A. a. L. T. Munoz, "On-line dead time compensation technique for open-loop PWM-VSI drives," *IEEE Transactions of Power Electronics*, vol. 14, no. 4, pp. 683-689, 1999.
- [17] S. N. I Boldea, *The Induction Machine Design Handbook*, CRC Press, 2009.
- [18] M. Li, Z. Yang, F. Lin and H. Sun, "Characteristics of Linear Induction Motor Considering Material of Reaction Plate Change," *Journal of Computers*, vol. 8, no. 1, pp. 102-107, 2013.
- [19] N. Ahmadnia, "The Linear Induction Motor (LIM) & Single Linear Induction Motor (SLIM)," *American Journal of Electrical Power and Energy Systems*, vol. 3, no. 4, pp. 71-75, 2014.
- [20] I. Y. Takahashi I., "Decoupling Control of Thrust and Attractive Force of a LIM Using a Space Vector Control Inverter," *IEEE Transactions on Industry Applications*, vol. 29, no. 1, 1993.
- [21] Y. S. Iwamoto M., "End Effect of High-Speed Linear Induction Motors," *Electrical Engineering in Japan*, vol. 92, no. 3, 1972.
- [22] J. A.P., "High Speed Linear Induction Motor Efficiency Optimization," Master's Thesis, MIT, 2005.
- [23] S. Nonaka, "Investigation of Equivalent Circuit Quantities and Equations for Calculation of Single-Sided Linear Induction Motors (LIM)," *Electrical Engineering in Japan*, vol. 117, no. 2, 1996.

- [24] K. Woronowicz, "A Novel Linear Induction Motor Equivalent-Circuit With Optimized End Effect Model," *Canadian Journal of Electrical and Computer Engineering*, vol. 37, no. 1, 2014.
- [25] W. e. a. Xu, "Equivalent Circuits for Single-Sided Linear Induction Motors," *IEEE Transactions on Industry Applications*, vol. 46, no. 6, 2010.
- [26] F. Cobb, "Coefficients of Friction," in *Structural Engineer's Pocket Book: Eurocodes*, CRC Press, 2015.
- [27] AK Steel, "Selection of Electrical Steels for Magnetic Cores," 2007. [Online]. Available: http://www.aksteel.com/pdf/markets_products/electrical/mag_cores_data_bulletin.pdf. [Accessed June 2015].
- [28] M. Sundaram and P. Navaneethan, "On the Influence of Stator Slot Shape on the Energy Conservation Associated with the Submersible Induction Motors," *American Journal of Applied Sciences*, vol. 8, no. 4, pp. 393-399, 2011.
- [29] S. Bahmidi, "Design of a Single Sided Linear Induction Motor (SLIM) Using a User Interactive Computer Program," University of Missouri-Columbia, 2005.
- [30] ANIXTER, "Technical Information Handbook: Wire and Cable," ANIXTER Inc., 2013.

- [31] E. Murphy, "Direct Digital Synthesis (DDS) Controls Waveforms in Test, Measurement, and Communications," *Analog Devices Analog Dialogue*, vol. 39, 2005.
- [32] S. Peterson, "How to Choose the Right Control Method for VFDs," *Machine Design, Yaskawa America Inc.*, 23 Oct 2014.
- [33] Fairchild Semiconductor Corporation, "Design and Application Guide of Bootstrap Circuit for High-Voltage Gate-Drive IC," 2008.
- [34] L. B. X. B. F. F. Wang T., "Linear Induction Motors for Vehicles Climbing on Steel Plates," *IEEE Transactions on Energy Conversion*, vol. 29, no. 3, September 2014.